SMALL-SIZE SPACE DEBRIS DATA COLLECTION WITH EISCAT RADAR FACILITIES

J Markkanen, M Postila and A van Eyken

Final Report
of
ESOC Contract No. 18575/04/D/HK(SC)
with
EISCAT Scientific Association

ESA/ESOC Technical Management
H Klinkrad and M Landgraf

June 2006

Generated from LaTeX source, June 27, 2006.

ESA study contract summary page

ESA CONTRACT No 18575/04/D/HK(SC)	SUBJECT: Small-size Space Depris Data Collection with EISCAT Radar Facilities	CONTRACTOR: EISCAT

ABSTRACT

The present study is the third in a series of our ESA contracts since 2000 to develop, implement, and apply a method of using the EISCAT ionospheric research radars, located in northern Norway near Tromsø (site latitude 69.5º, radar wavelength 32 cm) and in Longyearbyen on Svalbard (78.1º, 60 cm), to measure space debris simultaneously with the standard ionospheric measurements. In the present contract, the emphasis has been in performing a significant number of debris measurements. We have accumulated about 10 000 debris events during more than 800 hours of measurements in 2004 and 2005.

A basic aim through this series of studies has been to be able to conduct the debris measurements in a "piggy-backed" mode, without interfering with the standard EISCAT measurements. We utilize the radar's analog signal and the frequency reference, but otherwise place no requirements whatsoever on the host's resources or operations. Especially, we take both the radar transmission schemes and the antenna pointing directions as given, and optimize their use for our purposes. We use a special digital receiver back-end, connected in parallel with the standard EISCAT receiver at some point in the analog signal path. For increased detection sensitivity, we implement coherent pulse-to-pulse integration by computing the radar ambiguity function from a segment of measured transmission and reception that typically covers coherently a few tens of interpulse periods, 0.2-0.3 seconds. At the Tromsø radar, 0.2 s coherent integration gives 50% probability of detection of a 2.5 cm sphere at 1000 km range. At the Svalbard radar, the corresponding minimum detectable diameter is 2.9 cm. At the Tromsø system, typical integrated detection rate over LEO is 15-20 events per hour, on Svalbard, about twice as much.

Even though we have been able to obtain good sensitivity and reasonable event rates, there are inevitably limitations with our approach. Partly these are due to using radars that have been designed for beam-filling soft targets rather than small hard targets, partly due to the inherent difficulty of coherent integration, and partly due to the piggy-backed nature of our measurements. First, even though it seems that the coherent integration increases detection sensitivity somewhat, it is very difficult to get quantitative control on the integration loss, especially in the common EISCAT case of multi-frequency transmission. Second, none of the EISCAT antennas is equipped with a monopulse feed, so the target's path across the radar beam is not known, and only a lower bound for the radar cross section can be estimated. An unknown proportion of the events represents side-lobe detections. Third, the dominant pointing directions in EISCAT are towards south at about 70-80 degrees elevation, which makes it difficult to estimate Doppler-inclination.

In spite of the limitations, EISCAT space debris measurements, summarized in this report and available in detail on the accompanying CD, taken with two wavelengths, at two high latitude locations, in long continuous measurements (weeks), sometimes with multiple pointing directions, present an interesting check of the debris models in LEO. Some further work, however, remains to be done before quantitative comparison to the models, such as ESA's MASTER model, can be made with confidence. For instance, it seems desirable to re-detect the debris events with non-coherent pulse-to-pulse integration, a process which would be entirely possible since we routinely save the raw data of all the events.

The study was carried out by the following team members:
J. Markkanen, M. Postila (Study Manager) / EISCAT

ESA Study Manager: Heiner Klinkgrad, Markus Landgraf, ESOC

Contents

List of Tables

List of Figures

1. Introduction

1.1. Background

It is estimated that there are more than 200 000 objects larger than 1 cm currently orbiting the Earth as an enduring heritage of four decades of space activity. This includes the functioning satellites, but by far the bulk of the objects represent what is called space debris (SD), man-made orbital objects which no longer serve any useful purpose. Many of the small-sized (less than 10 cm) particles are due to explosions of spacecraft and rocket upper stages, but there are also exhaust particles from solid rocket motors, leaked cooling agents, and particles put into space intentionally for research purposes. The large (> 10 cm) objects have known orbits and are routinely monitored by the US Space Surveillance Network, but information of the smaller particles is fragmentary and mainly statistical. In particular, no radar in Europe is routinely used for monitoring small-sized SD.

This report describes the third phase of ESA contract work that started in 2000–2001 with a study about the feasibility of using the EISCAT ionospheric research radars for space debris measurements (3). Since the early 1980's, the EISCAT mainland radars—the Tromsø UHF radar operating at 930 MHz and the VHF radar operating at 225 MHz—have been performing ionospheric measurements on the order of 2000 hours per year; and since the late 1990's, after the EISCAT Svalbard radar (ESR) became operational, EISCAT has been measuring more than 3000 hours annually. The goal is to use a substantial proportion of these operating hours for simultaneous space debris measurement in cost-effective way. In the first study, we showed that it is feasible, and technically straightforward, to perform SD measurements in parallel with normal EISCAT ionospheric measurements, without interfering with those measurements (5).

Our measuring approach, introduced in the intial study, is to operate a separate digital receiver back-end, which we call the SD receiver, in parallel with the EISCAT standard digital receiver. This allows us to implement pulse-to-pulse coherent integration via a method which we call the match function (MF) method. Essentially our MF is what is often called the radar ambiguity function in the literature (9). The coherent integration is achieved by computing the MF as function of range and velocity for a set of values, and finding the maximum of the function. For a coherent signal, the maximum value of the MF gives an estimate of the total signal energy. Target detection is based on the maximum value exceeding a predefined threshold. The position of the maximum gives estimates of target range and radial velocity.

To make the hardware as simple and cheap as possible, the custom-made part of the SD receiver is basically just a fast sampler and digital demodulator; the MF computations are done in fast but still cheap general purpose workstations. The SD receiver samples the EISCAT analog signal, at the second intermediate frequency (around 10 MHz) level, fast enough to capture the relevant frequency channels into a single digital stream, without doing the customary channel separation. Typically during a measurement, we sample at the rate of about a million complex samples per second continuously, producing

more than 10 GBytes of data per hour.

A straightforward implementation of the MF method implies long data vectors, with lengths of hundreds of thousands complex points, to be Fourier-transformed a few thousand times per every second of raw data; basically, one is computing power spectra for a relatively large number of range gates. At the Third European Conference on Space Debris in 2001, we had to concede that with the processing speed that we had achieved at the time, it would take several centuries of CPU time to analyze just one year's quota of EISCAT space debris measurements. However, soon afterwards, M Lehtinen of Sodankylä Geophysical Observatory, who was the project leader of the first study, realized that by accepting some loss of detection sensitivity and a small bias in the velocity estimate, it would be possible to speed up MF computation drastically, typically by more than two orders of magnitude. We use the term fast match function algorithm (FMF) for the resulting computation scheme. The FMF algorithm is described in (7), and is also sketched in Fig. 3 on p. 53 in this report.

The second phase of the study (4) was conducted in 2003–2004, the contract being directly between ESA and EISCAT. The main purpose was to develop the measuring and analyzing system to be capable of handling large amount of measurements, hundreds of hours per year. The key task was to boost the system performance so that target detection and parameter estimation could be done in real-time, to avoid excessive piling-up of data, and also to make a more or less interactive inspection of the data feasible. The latter aspect was of some importance, in order to gain an understanding of the properties of the MF-method when applied to real data. In the final report of that phase (6), we gave a detailed analysis of several aspects of the MF-method, both in its the basic form, and when using the fast variant. We described the measuring and analysis software in considerable detail. We were also able to show the results of about 150 hours of debris measurements, all conducted at the Tromsø 930 MHz radar. Our first longer, 100 hour, campaign was run in November 2004. Before the 100 hour run, we took part in the international beam park 2004 debris campaign by collecting 17 hours of data in September 2004[1].

After our first two ESA contracts had established the feasibility of using EISCAT radars for SD measurements, and had built sufficient machinery to handle the data in practice, the present contract was signed late in 2004, for the purpose of finalizing the data processing and applying it to produce a fairly large amount of debris measurements.

1.2. Study objectives

According to our contract with ESA/ESOC, the overall objective of this study is to prepare for an operational phase of routine space debris measurements during the standard EISCAT ionospheric measurements, based on the developments in the two precursor studies. Sub-objectives are the following

1. to collect a substantial amount of data on the LEO space debris environment
2. to improve our software to make SD measurements more user friendly to conduct
3. to consolidate the availability of the space debris receiver hardware

[1] A report of EISCAT contribution to the beam park 2004 campaign, as well as other documents related to our SD work, are available through our web site at `http://www.sgo.fi/~jussi/spade/`.

4. to move towards facilitating the use of EISCAT data in the ESA PROOF tool

The contract work was divided to five work packages, which were grouped into two "phases". Phase One was to cover the first two work packages during 2005; whether or not to continue the study to Phase Two, was left to be decided later on. Either party had the option to discontinue the contract after Phase One. In project meeting on February 14th 2006 at ESOC, it was unanimously agreed that, due to shortage of resources, the Phase Two would not be activated. This report therefore covers only the Phase One of the study, the work packages W.P. 1 and W.P. 2.

1.2.1. Work Package One: Updating of the data processing methods and algorithms

In the technical proposal of the contract, the work to be done in the work package one was summarized by two action items and three output items. The action items were

(A1) Implement a hit grouping algorithm that automatically connects hits that are caused by a single debris particle, removing hits that are caused by spurious noise, hits that are so near the edges of the data vector that a proper analysis is not possible, and hits that are caused by range-aliased targets, and then copy the raw data belonging to those hits to an event directory.

(A2) Analyze the loss of coherence for longer signal integration times and estimate the sensitivity of the measurement.

The required output items were

(O1) An improved version of the DARC hit-grouping algorithm.

(O2) Quantitative description of the loss of coherence due to approximations done in our implementation of the MF- and FMF-algorithms.

(O3) Quantitative comparison between detection sensitivity achieved by using standard incoherent integration on one hand, and the MF-based coherent integration on the other hand, both methods applied to a pre-recorded EISCAT raw data set.

The status of WP 1

A1, O1 The hit grouping has been much enhanced by improving the preprocessor of DARC, the bad-hit removing Matlab program CLEANSCANS. The updated CLEANSCANS can work automatically, and is as effective in performing the tasks listed in item (A1) as if the operation were done interactively by a skilled operator. CLEANSCAN is covered in section 3.2 on p. 34 of this report.

A2, O2–3 What we are really interested in when considering the loss of coherence in our coherent integration is the effect on detection sensitivity and RCS estimation. In the final report (6) we have already inspected, semi-quantitatively, the effect of multiple frequencies (p. 55), the effect of target acceleration (p. 40, Fig. 3.6 and p. 38, Fig. 3.5), and the consequences of using FMF instead of MF (pp. 40–49), and we will not repeat the work here. We have now attempted to understand better the issue of coherent versus non-coherent integration.

We started experimenting with non-coherent pulse-to-pulse integration for the first time when analyzing the data from EISCAT's participation in the 2004 beam park experiment, and found that there was little difference in the number of events that came though from the final analysis. In sections 2.1 through 2.6 we adapt to the MF-method the standard procedure of handling the probability of false alarm and the probability of detection in radar measurements, so that we can give the expected difference between coherent and non-coherent integration for a particular experiment scheme in section 2.7.[2] Section 2.7 is very brief, due to lack of time to run the necessary simulations, but the basic conclusion is clear enough. Even with fully efficient coherent integration, the expected gain in terms of the weakest detectable signal is quite small, about 5–6 dB, see panel (b) of Fig. 12 on p. 62. With real data it is then entirely possible to lose most if not all of the advantage to the mentioned sinks of coherence, especially, when one has to handle a multi-frequency experiment. Nevertheless, in our implementations, the FMF-based coherent integration executes faster than a corresponding non-coherent integration, and tends to be slightly more sensitive, so we are going to use FMF for the initial detection also in the future. The ideal solution might be some kind of hybrid integration scheme.

1.2.2. Work Package Two: Routine space debris measurements during common programme measurements

In the technical proposal of the contract, the work to be done in the work package two was summarized by four action items and one output item. The action items were

(A1) Install the new space debris measurement computer at the site in Tromsø and connect it to the analogue signal chain.

(A2) Create an interface of the space debris receiver to the EISCAT Real-Time Operating System (EROS).

(A3) Collect, analyse, and store space debris detections during as much EISCAT Common Programme field aligned operation as possible. EISCAT Common Programme schedules are normally only decided one month ahead but at least 440 hours of suitable programming are expected to be available.

(A4) Investigate possibilities to use analysed data collected with the 500 MHz EISCAT Svalbard Radar (ESR)

The single output time was covered by specifying that

(O1) The duration covered by the data collection interval must be at least 440 hours.

[2] Even though standard books like (9) handle *both* the detection probabilities *and* the radar ambiguity function, they do not seem to make much connection between those subjects—the detection probabilities seem to be given in the situation of envelope detection, with lip service paid to possible coherent pre-integration. The ambiguity function is seen as a device so analyse the radar measurement ambiguities, but not as a basic tool also for target detection.

The status of WP 2

A1 The SD receiver, including the two computers, are "permamently" installed in Tromsø, and only require powering-up to be ready to start data collection. The hardware has worked reliably at Tromsø.

A2 Most of the EROS interface for space debris measurement, which we call DROS, was built during the previous contract. The DROS system has been used routinely, in all the measurements made for this contract, to take care of the data recording. The DROS is basically an enhanced copy of the EROS system itself, and is too large a system to be documented here; we only briefly mention it on p. 36.

A3,O1 During 2005, we measured SD for about 700 hours, collecting about 8000 events. All the measurements were made in parallel with EISCAT CP measurements. The measurements were concentrated in four campaigns described in chapter 4. The campaign results are summarized in numerous figures in this report. Lists of event parameters and a summary plot for each of the analyzed events are available on the CD accompanying this report.

A4 We ran a 24 hour test measurement at the ESR site on November 10th, 2005. The measurement is described in section 4.3 on p. 40, and the measurement results are included on the CD. It is quite clear that the ESR system is well suited for these measurements.

1.2.3. For future work

The preparatory work needed to apply the ESA PROOF tool to EISCAT data was not covered by the two work packages under the present contract. Further work is needed before the collected data can be used quantitatively to test the debris models. A task would be to make sure that the PROOF tool can handle arbitrary antenna beam shapes, side-lobes included, so that no particular distinction needs to be done concerning side-lobe detections. The other task would be to resort to non-coherent pulse-to-pulse integration in target detection, because it is very difficult to get quantitative control on the integration loss in the coherent integration. It appears that our coherent integration is *somewhat* more sensitive than the customary non-coherent integration, but to quantify the difference reliably in practice seems difficult. We therefore suggest to re-detect the collected data using non-coherent integration with sufficiently high detection threshold. This would result in some loss in the number of finally available events, but would give a firmer handle on the statistical properties of the events. A re-detection test with one of the four data sets taken during this contract found 667 events with non-coherent integration, out of the 801 events originally detected with FMF-based coherent integration. We have saved the raw data (about 400 GBytes) of all our events permanently to hard disk, so this approach is entirely feasible.

2. Theory

2.1. The match function method

The measured complex-valued signal $z(t)$ consists of target echo and noise,

$$z(t) = s(t) + \gamma(t)\,. \tag{2.1}$$

During a time interval $[0, T_c]$, the integration time, the demodulated signal $s(t)$ is modeled as a delayed-in-time, Doppler-shifted replica of the transmission $x(t)$,

$$s(t) = b_0 x(t - 2R_0/c)\mathrm{e}^{-i2\pi\frac{v_0}{\lambda/2}t}\,, \tag{2.2}$$

where R_0 is target range, v_0 is target radial velocity in the radar frame of reference, and λ is the radar wavelength. In EISCAT space debris measurements, both $x(t)$ and $z(t)$ are measured. An example of the recorded raw data $z(t)$ and transmission sample data $x(t)$ in the single-frequency-channel MANDA expriment is shown in Fig. 1.

We assume that the echo stays coherent, that is, the model Eq. (2.2) holds, during the integration time, typically a few tens of interpulse periods (IPPs). Then it is possible to use coherent integration in target detection. The match function method of coherent pulse-to-pulse integration is based on computing the quantity that is often called the radar ambiguity function in the literature (9), but which we choose to term the match function, MF. References (5) and (7) present the match function method from the point of view of Bayesian statistical inversion. Here we give a less rigorous description, which also omits complications that arise when we apply the method in practice in EISCAT, such as the need to correct for target acceleration and to handle multiple frequency channels. The match function is a function of the range gate $R_j = j\tau_s c/2$, where τ_s is the sampling interval, and the Doppler-velocity v, which is the radial component of the velocity vector (positive away from the radar). The MF is computed from the sampled signal vector $\mathbf{z}$ and the transmission-sample vector $\mathbf{x}$ as

$$\mathrm{MF}(v, R_j) = \frac{|\sum_n z_n \overline{x}_{n-j}\mathrm{e}^{i2\pi\frac{v}{\lambda/2}n\tau_s}|}{\|\mathbf{x}\|}\,, \tag{2.3}$$

where

$$\|\mathbf{x}\| = (\sum_n |x_n|^2)^{1/2}\,. \tag{2.4}$$

It follows from Eq. (2.3) that at the velocity points

$$v_k = \frac{k}{N_{\mathrm{FFT}}}\frac{\lambda}{2}\frac{1}{\tau_s} \tag{2.5}$$

the MF can be computed using a DFT. For a fixed range, the function $v \mapsto \mathrm{MF}(v, R_j)$ is essentially the spectrum of the cross-correlation vector $\mathbf{w}^{(j)} : w_n = z_n\overline{x}_{n-j}$; we refer

to it as the MF velocity slice through the range R_j. The bottom panel of Fig. 4 gives an example of a velocity slice.

Figure 3 summarizes the match function computation. In the figure we also show an extra step that we normally take to speed up the computations: basically, we just drop out the "unnecessary" zeros that occur in the DFT input vector due to the pulsed transmission. We call the resulting algorithm the fast match function algorithm, FMF. The gain of speed is large, typically more than two orders of magnitude, so we almost always use FMF in the practical computations. The gain comes with a (modest) price, since the detection sensitivity in the FMF-scheme is slightly reduced compared to the MF, as we hint to in the caption of Fig. 21 and analyze quantitatively in (7).

From Eq. (2.3) and Eq. (2.2) and the Cauchy-Schwartz inequality it follows that if there is no noise, the position of the MF maximum gives the target range R_0 and radial velocity v_0,

$$\arg\max_{v,R} \mathrm{MF}(v,R) = (v_0, R_0)\,,$$

and the value of the maximum is proportional to the square root of the total signal energy E_s ($\sim \|\mathbf{s}\|^2$). With noise, we use the position of the MF maximum as an *estimate* of the target range and Doppler-velocity,

$$(\widehat{v}, \widehat{R}) = \arg\max_{v,R} \mathrm{MF}(v,R)\,, \tag{2.6}$$

and we expect the MF maximum value still to be a reasonable estimate for $\|\mathbf{s}\|$. However, with noise, we need to consider background subtraction. Assuming that the maximum of the noisy MF takes place at about the correct position, we can form the expectation value of MF^2 (over repeated trials with the same signal, but different noise). Assuming that the noise samples γ_n are zero mean, independent, complex gaussians with variance σ^2, so that $\mathbb{E}(\gamma_m \overline{\gamma}_n) = \delta_{m,n}\sigma^2$ and terms linear in γ vanish, we get

$$\mathbb{E}\left(\max \mathrm{MF}^2\right) \approx \frac{\mathbb{E}|\langle b_0 x_0 + \gamma, x_0\rangle|^2}{\|x_0\|^2} = \|b_0 x_0\|^2 + \frac{\mathbb{E}|\langle \gamma, x_0\rangle|^2}{\|x_0\|^2} = \|s\|^2 + \sigma^2\,. \tag{2.7}$$

This shows that to get an unbiased estimate of $\|s\|^2$, we have to subtract the noise power from the MF^2 maximum value,

$$\widehat{\|\mathbf{s}\|^2} = \max \mathrm{MF}^2 - \sigma^2\,. \tag{2.8}$$

With coherent integration, the minimum detectable signal will have $\max \mathrm{MF}^2 \gtrsim 25\,\sigma^2$ in our case, so the subtraction has only a minor effect to the estimate. With non-coherent integration, the background subtraction is essential.

The norm $\|\mathbf{s}\|$ of the received, complex-valued sampled signal is related to the actual energy $E_{s'} = \int |s'(t)|^2 dt$ of the incoming signal $s'(t)$ in front of the receiver by

$$\tau_\mathrm{s}\|\mathbf{s}\|^2 = \int |s(t)|^2 dt = g_f \int |s'(t)|^2 dt = g_f E_{s'}\,, \tag{2.9}$$

where τ_s is the sampling interval. The equalities in Eq. (2.9) require the signal to be of sufficiently narrow bandwidth, so that there is not much aliasing, and that the receiver power gain g_f can be taken to be constant across the signal bandwidth. We divide the receiver gain such that $g_f = g_\mathrm{A} \cdot G_f$, where g_A is the gain of the relatively wide-band analog receiver and G_f is the precisely calculable gain of the digitally implemented space

debris receiver. We take g_A to be a constant over the whole bandwidth of the SD receiver (not just over the signal bandwidth). We get rid of the unknown gain g_A by noting that the noise power after the receiver, σ^2, estimated as the variance of the reception samples z_n in the absence of signal, is

$$\sigma^2 = kT_{\rm sys} g_{\rm A} B_{\rm eq}\,, \tag{2.10}$$

where $B_{\rm eq}$ is the noise-equivalent bandwidth of the SD receiver, and $kT_{\rm sys}$ is the power spectral density of the wide-band noise in front of the receiver, which we take to be a known radar parameter. The impulse response of the SD receiver is constructed to be of constant value $1/\tau_{\rm s}$ and duration equal to $\tau_{\rm s}$. For such a system, $B_{\rm eq} = 1/\tau_{\rm s}$ so that, from Eq. 2.8–2.10, we get

$$\frac{\widehat{E_{s'}}}{kT_{\rm sys}} = \frac{1}{G_f}\frac{\widehat{\|\mathbf{s}\|^2}}{\sigma^2} = \frac{1}{G_f}\left(\frac{\max \mathrm{MF}^2}{\sigma^2} - 1\right)\,. \tag{2.11}$$

Normally G_f is close to unity, and we will drop it from the notation from now on (in practice we have not made the G_f correction in the data analysis). We will also drop the prime from $E_{s'}$. We call the dimensionless ratio of the total signal energy divided by the noise power spectral density (= noise power per unit bandwith) the energy-to-noise ratio ENR,

$$\mathrm{ENR} = \frac{E_s}{kT_{\rm sys}}. \tag{2.12}$$

Thus, we estimate the energy-to-noise ratio from the MF maximum value as

$$\widehat{\mathrm{ENR}} = \frac{\max \mathrm{MF}^2}{\sigma^2} - 1\,. \tag{2.13}$$

Equation (2.11) has two related uses. First, it gives the target detection criterion for the threshold detection: with threshold Θ,

$$\text{detection} \leftrightarrow \sqrt{\widehat{\mathrm{ENR}} + 1} \;>\; \Theta\,. \tag{2.14}$$

As indicated by including the "1" into Eq. (2.14), we retain the background in the detection test; that is, we test directly $\max \mathrm{MF}/\sigma$ against the threshold, rather than the estimated ENR. We try to set the threshold Θ to be so high that there are only "very few" false alarms. Experience has shown that, with the coherent integration times 0.2–0.3 s that we normally use with the EISCAT standard experiments, the value $\Theta = 5$ is a suitable starting point. In the next section we give some theoretical justification for that choice, showing that it corresponds to a false alarm time of a few hours. The standard threshold might need to be increased sometimes, typically during strong auroral events, due to clutter. Then we normally increase Θ perhaps up to 7, but only in those ranges where the ionospheric clutter actually is a problem. On the other hand, we try to keep the threshold setting intact during a single measurement campaign.[1] Normally the clutter is a problem only at altitudes up to about 500 km, and their range aliases.

[1]The threshold is set via the threshold entry in the scanner control (.sdef) files, which are saved permanently in the `/Scans` directory three. The .sdef files are also available in the `info` directories in the analysis result three `/Analysis`. Consulting these files should give a fairly good idea about the detection thresholds used in the campaigns. Unfortunately, sometimes we have been forced to modify the threshold setting in add hoc manner during strong clutter conditions, and these modifications have not always been properly tracked.

The second use of Eq. (2.11) is to estimate the target "size". Then we treat the system temperature as a known radar parameter, and use the measured MF maximum and the measured noise variance to find the signal energy $E_{s'}$ in physical units. We use that estimate to find a lower limit, $\mathrm{RCS}_{\min}$, for the target's radar cross section (RCS). From the standard radar equation it follows

$$\mathrm{RCS} = \frac{(4\pi)^3\, kT_{\mathrm{sys}} \cdot R^4 \cdot \mathrm{E_s}}{G(\phi)^2 \cdot \lambda^2 \cdot P_x \cdot \mathcal{D}T_c}\,. \tag{2.15}$$

Here R is target range, λ is radar wavelength, P_x transmission peak power, $\mathcal{D}$ transmission duty cycle so that $\mathcal{D}T_c$ is the actual length of transmission during the integration T_c. The factor $G(\phi)$ is the antenna power gain in the direction of the target within the radar beam, an angle ϕ offset from the known direction of the antenna optical axes. In the EISCAT system, it is normally not possible to find the offset angle. As a way of cataloguing the observed signal strength, we therefore normally quote $\mathrm{RCS}_{\min}$, which we get from Eq. (2.15) by setting $\phi = 0$.

2.2. Probability of false alarm in coherent integration

If z is a complex gaussian random variable with zero mean and variance σ^2, the probability density function (PDF) with respect to the measure $dz \leftrightarrow dxdy$, where x and y are the real and imagenary part of z, is by definition

$$f(z) \equiv \frac{1}{\pi\sigma^2} \mathrm{e}^{-\frac{|z|^2}{\sigma^2}}\,. \tag{2.16}$$

In this case, the real and imagenary parts are independent real gaussians with variance $\sigma^2/2$ each. Using Eq. (2.16), the cumulative probability density (CPD) of the magnitude $|z|$ of z, which is a real-valued random variable, is

$$F(|z|) \equiv \mathbb{P}(|z| < r) = \mathbb{P}(|z|^2 < r^2) = \int_0^{r^2} |z|^2 f(z) dz = 1 - \mathrm{e}^{-\frac{r^2}{\sigma^2}}\,, \tag{2.17}$$

so that the probability of false alarm, that is, the probability that $|z|$ would exceed a given threshold θ, is

$$P_{\mathrm{fa}}(\theta) = \mathbb{P}(|z| > \theta) = \mathbb{P}(|z|^2 > \theta^2) = \mathrm{e}^{-\frac{\theta^2}{\sigma^2}}\,. \tag{2.18}$$

If we have N independent complex gaussians z_n, each with zero mean and variance σ^2, the probability of false alarm is the complement of the probability that all the the magnitudes would be less than the threshold. Due to their independence, this is equal to the product of the individual probabilities,

$$\begin{aligned} P_{\mathrm{fa}}(\theta) &= \mathbb{P}(\max|z_n| > \theta) \\ &= 1 - \prod_{n=1}^{N} \mathbb{P}(|z_n| < \theta) \\ &= 1 - [1 - \mathrm{e}^{-\frac{\theta^2}{\sigma^2}}]^N\,. \end{aligned} \tag{2.19}$$

When $N\mathrm{e}^{-\frac{\theta^2}{\sigma^2}} \ll 1$, Eq. (2.19) is well approximated by

$$P_{\mathrm{fa}}(\theta) = N\mathrm{e}^{-\frac{\theta^2}{\sigma^2}}\,. \tag{2.20}$$

That is, when the probability of false alarm is small, the N-point probability is just the sum of the probabilities (Eq. (2.18)) that the threshold would be exceeded at any one single point.

We model EISCAT transmission by a train of M non-coded pulses, of unit magnitude, each pulse L samples, and assume interpulse period of P samples. We want to know what is the probability of false alarm in the our method of coherent integration, in particular, when using the FMF version of the method. We want to estimate the probability $P_{\rm fa} = \mathbb{P}(\max_{j,k} \mathrm{FMF}(j,k) > \Theta)$ when there is no signal present. Refer to Fig. 3 for a summary and notation.

We first fix the range index, j, and consider a single velocity slice. Normally, we know a priori that the velocity is not very large, and therefore, we do not maximize over all possible velocity indexes. Even though we normally pad the FFT input vector $\mathbf{u}$ to be of length of some power of 2, we now assume that from the ML noise points γ_n going into $\mathbf{u}$, we compute an ML-point FFT. Then the velocity slice, before taking the magnitude, consists of ML complex points $\Gamma(j,k)$,

$$\begin{aligned} \Gamma(j,k) &= \frac{\langle \gamma, \chi(j,k) \rangle}{\|x\|} && (2.21) \\ &= \sum_{n=0}^{ML-1} \gamma_{j+n} \mathrm{e}^{-i2\pi kn/ML} / \sqrt{ML}\,. && (2.22) \end{aligned}$$

As a sum of equally distributed, independent complex gaussians, the Fourier-transform output points are also independent complex gaussians. Due to the normalization by $\sqrt{ML}$, the variance of each $\Gamma(j,k)$ equals σ^2. Then it follows from Eq. (2.19) that, for the fixed range j,

$$P_{\rm fa}^{(j)} = \mathbb{P}(\max_{k=1}^{N_v} |\Gamma(j,k)|^2 > \theta^2) = 1 - (1 - \mathrm{e}^{-\frac{\theta^2}{\sigma^2}})^{N_v}\,, \tag{2.23}$$

where N_v is number of points of the slice to include into the maximization. Noting that $\mathrm{MF} = |\Gamma|/\sigma$ and expressing the threshold in terms of the dimensionless variable $\Theta = \theta/\sigma$, we can express Eq. (2.23) as

$$\begin{aligned} P_{\rm fa}^{(j)} &= \mathbb{P}\left(\frac{\max_{k=1}^{N_v} |\Gamma(j,k)|^2}{\sigma^2} > \frac{\theta^2}{\sigma^2} \right) \\ &= \mathbb{P}\left(\frac{\max_k \mathrm{MF}(j,k)^2}{\sigma^2} > \Theta^2 \right) \\ &= 1 - (1 - \mathrm{e}^{-\Theta^2})^{N_v}\,. && (2.24) \end{aligned}$$

We would like to be able to drop the (j) from $P_{\rm fa}^{(j)}$ in Eq. (2.24), that is, we would like to know the false alarm probability when we go through a set of ranges, as we do in the target detection. Unfortunately, it does not appear straightforward to proceed analytically here. The problem is that the random variables $\Gamma(j,k)$ are not even approximately independent for nearby j—when the range j chances a little, most of the noise points involved are still the same. To get an idea of what happens when maximizing also in the range direction, we resort to Monte Carlo simulation. Based on the simulations, it appears that one can still use the functional form of Eq. (2.24), if one, in addition to using

an "effective N_v", also allows slight re-scaling of Θ. We try the following two-parameter (N and a) model

$$P_{\rm fa}(\Theta) = 1 - (1 - {\rm e}^{-\frac{\Theta^2}{a^2}})^N \quad (\approx N{\rm e}^{-\frac{\Theta^2}{a^2}}, \text{ for large } \Theta)\,. \tag{2.25}$$

For a simulation, we select a specific set of parameters for the pulse train, corresponding to the radar experiment of interest; generate noise-only data vectors $\mathbf{z}$; and perform a set of FMF-style integrations on them. This gives a set of max FMF values, which are binned to get an experimental $P_{\rm fa}(\Theta)$. For short runs, an hour or so on a Mac G5, one only gets good statistics for rather small values of the threshold, up to to about $\Theta = 4$. This value is still substantially smaller than the standard threshold 5 that we want to use in practice. To extrapolate, we fit Eq. (2.25) to the experimental distribution and pick $P_{\rm fa}(5)$ from the fit. Figure 7 on p. 57 summarizes the result of one such simulation. The simulated experiment was the MANDA experiment: pulse length $L = 100$ samples, interpulse period 1000 samples, sampling interval 2 μs. For each of the two integration times $T_{\rm c} = 0.1$ s (number of pulses $M = 50$) and $T_{\rm c} = 0.3$ s (150 pulses) a simulation run was made for 1000 integrations. Range gates from j=0 to 600 (200 gates), with step 3 were included into the maximization. Velocity interval was from -5 km s^{-1} to +5 km s^{-1}. With these parameters, a velocity slice has $ML =$ 50 000 and 150 000 points in the 0.1 and 0.3 s integrations, respectively, out of which $N_v = 627$ and $N_v = 1877$ were use. The dashed-dotted line in Fig. 7 on p. 57 gives the false alarm rate with range fixed, using Eq. (2.24). It gives almost two orders of magnitude too low value for $P_{\rm fa}$, when compared to the simulation data points, the dots in the figure, and the the fitted curve (solid line) through the dots. The least squares minimization fit was actually done on the cumulative probability distribution, shown in panels (a) and (c), using only those points where the corresponding probability distribution was significantly larger than zero.

For the particular simulation run shown in Fig. 7, the best-fit N and a are $N = 2.4 \times 10^4$ and $a = 1.029$ for 0.1 s integration, and $N = 5.6 \times 10^4$ and $a = 1.038$ for 0.3 s integration. Using these values, the extrapolated probability for detection with threshold 5.0 is 1.7×10^4 for 0.1 s integration, and 4.8×10^4 for 0.3 s integration. The corresponding *time of false alarm*, which we define to be the integration time $T_{\rm c}$ divided by the probability of false alarm,

$$t_{\rm fa} = \frac{T_{\rm c}}{P_{\rm fa}}\,, \tag{2.26}$$

becomes 21 hours for $T_{\rm c} = 0.1$ and 17 hours for $T_{\rm c} = 0.3$ s, in this data set. To get some feeling about the statistical significance of the difference in $t_{\rm fa}$, 21 h versus 17 h, found in the simulation, we repeated the simulation a couple of times. The result is shown in Fig. 8. As was to be expected for an extrapolation in an exponential tail, statistical variations are large. For 0.1 s integration, we find $N = (2.2 \pm 0.6) \times 10^4$, $a = 1.031 \pm 0.016$, $P_{\rm fa} = (1.5 \pm 0.7) \times 10^{-6}$ and $t_{\rm fa} = 23 \pm 10$ hours. For 0.3 s integration, we find $N = 5.4(1.4) \times 10^4$, $a = 1.044(0.017)$, $P_{\rm fa} = 4.0(0.7) \times 10^{-6}$ and $t_{\rm fa} = 16(5)$ hours. The errors refer for the standard deviation. We cannot make any firm conclusion about the constancy of the false alarm time based on these data.

For the purpose of determining the detection threshold, simulations such as shown in Fig. 8 seem to indicate that one can roughly approximate the probability of false alarm with the fixed-range formula, Eq. (2.23) (the dashed line in Fig. 8), with N_v replaced by $N_v \cdot N_g$, where N_g number of range gates. In this approximation, the false alarm time becomes asymptotically independent of the integration time in coherent integration.

Using the asymptotic form $P_{\rm fa} = N_v \mathrm{e}^{-\Theta^2}$, both $P_{\rm fa}$ and $T_{\rm c}$ are seen to be directly proportional to the number of pulses integrated. We have

$$t_{\rm fa} = \frac{1}{N_g}\frac{1}{\mathcal{D}}\frac{\lambda}{4v_{\max}}\mathrm{e}^{\Theta^2}\,, \tag{2.27}$$

where $\mathcal{D}$ is the experiment duty cycle and $v_{\max}$ is the maximum velocity to be monitored. In Eq. (2.27), given the false alarm time, the threshold depends only weakly (logarithmically) on the number of range gates, so the precise number of the range gates, independent or not, is not very important. Figure 9 shows the relation (2.27) for some EISCAT experiments. The figure suggests that with the typical number of about 1000 range gates, instead of the 200 gates that we used in the simulation, the standard threshold 5.0 may be a little too low. We would like to have a false alarm time of about one day, to be sure that the false alarms do not corrupt the event statistics (we get typically at least 10 manifestly correct events per hour). On the other hand, in practice we anyway often need to adjust the detection threshold because of variable clutter, noise injection, and other disturbances, at least for some ranges. So one perhaps should not attempt to insert too many decimals into the threshold value—the round "5" is not a bad starting point.

2.3. Probability of detection in coherent integration

Having fixed the detection threshold (to 5.0, in terms of $\max \mathrm{MF}/\sigma$), we now inspect how the probability of detection, $P_{\rm D}$, depends on the signal strength in the coherent integration scheme. So we assume a signal of the form Eq. (2.2), and ask what happens to

$$P_{\rm D} \equiv \mathbb{P}(\max \mathrm{MF}/\sigma > \Theta) = \mathbb{P}(\max \mathrm{MF}^2/\sigma^2 > \Theta^2) \tag{2.28}$$

when the signal amplitude (magnitude of the complex-valued parameter b_0 in Eq. (2.2)) is varied.

We have selected the detection threshold to be rather high. Then, if the target is detected at all, the detection will in most cases happen very near to the actual target location, (R_0,v_0), in the (R,v)-space. To a good approximation, we have

$$\max \mathrm{MF}/\sigma \approx \mathrm{MF}(R_0, v_0)/\sigma = \frac{|\langle b_0\chi_0 + \gamma, \chi_0\rangle|}{\|\chi_0\|\sigma}\,, \tag{2.29}$$

where $\chi_0(t)$ is Doppler-shifted, time-shifted transmission, $\chi_0(t) = x(t-2R_0/c)\mathrm{e}^{-i2\pi v_0 t/(\lambda/2)}$. We will assume for simplicity that the transmission has unit magnitude, and consists of a train of M pulses of length L samples with an interpulse period of P samples; phase coding of the pulses does not change the result. Then the complex-valued random variable

$$Z = \frac{1}{\sigma}\frac{\langle b_0\chi_0 + \gamma, \chi_0\rangle}{\|\chi_0\|}$$

can be written as

$$Z = \Gamma + \frac{\sqrt{ML}}{\sigma}\, b_0\,, \tag{2.30}$$

where Γ is a complex gaussian random variable with zero mean and unit variance. According to Eq. (2.28) and Eq. (2.29), we need to compute probabilities of the real random

variable $X = |Z|^2$. There does not appear to be an abundance of results readily available in literature for the PDFs of complex random variables. What we need here can be found by recasting the 1-D complex variable in Eq. (2.30) to a 2-D real vector, for which standard results are available (keyword: non-central chi-square distribution with two degrees of freedom). The result is the following. If Z is a complex gaussian random variable with zero mean and unit variance, and a is a complex constant, the PDF of the real random variable

$$X = |Z + a|^2$$

is

$$f_X(x, a) = \begin{cases} \mathrm{e}^{-x-|a|^2} \sum_{n=0}^{\infty} \frac{x^n}{n!} \frac{|a|^{2n}}{n!} = \mathrm{e}^{-x-|a|^2} \, I_0\left(2|a|\sqrt{x}\right) \,, \text{ when } x > 0 \\ 0 \,, \text{ elsewhere.} \end{cases} \tag{2.31}$$

The I_0 is the modified Bessel function of the first kind of order 0, and can be evaluated, for example, by the Matlab function BESSELI. The probability of detection, with threshold Θ and signal energy-to-noise ratio

$$\mathrm{ENR} = \frac{ML|b_0|^2}{\sigma^2} \,, \tag{2.32}$$

becomes

$$P_{\mathrm{D}} \;\; = \;\; 1 - \int_0^{\Theta^2} dx \, f_X(x, \sqrt{\mathrm{ENR}}). \tag{2.33}$$

The integral is evaluated numerically. Equation (2.33) shows that given the threshold, the probability of detection depends on the signal properties, the length of the coherent integration, and the noise variance, only via the combination ENR.

With our standard threshold $\max \mathrm{MF}/\sigma = 5.0$, which according to Eq. (2.14) corresponds to $\mathrm{ENR} = 24$, the probability rises quite sharply, from 5% at $\sqrt{\mathrm{ENR}} = 3.78$ to 95% $\sqrt{\mathrm{ENR}} = 6.12$. At at the detection threshold itself ($\sqrt{\mathrm{ENR}} = 4.90$), the probability of detection is 47%.

Once the detection threshold, in terms of ENR or $\max \mathrm{MF}/\sigma$, has been fixed, the detection sensitivity can be illustrated in more directly target-related quantities by selecting specific values for the transmission scheme and the radar system parameters. In Fig. 5, we assume target range 1000 km and show, for the radar's typical transmission, the RCS that is needed to achieve detection. For instance, at the Tromsø UHF radar, with 0.3 s coherent integration, RCS = 5 mm^2 is required to achieve $\mathrm{ENR} = 4.9^2$ (which gives 50% probability of detection). In Fig. 6, we use the effective target diameter in place of the strongly wavelength-dependent RCS (see also Fig. 12).

2.4. Non-coherent integration in the match function method

We will always process a single pulse coherently, by computing the power spectrum. We will use the expression "non-coherent pulse-to-pulse integration of M pulses" (or, more concisely, but misleadingly, just "non-coherent integration of M pulses"), when we process the data by computing r.m.s of the single-pulse match functions over M consecutive pulses. Using non-coherent integration (in the above sense) places less demands for the coherence time of the signal. On the other hand, if the signal is coherent, phase information is unnecessarily lost in the squaring.

We add a time parameter to the notation of the MF to indicate the start time of the integration, for example, $\mathrm{MF}(t; R, v)$. We also indicate how many pulses we are integrating, for example, $\mathrm{MF}^{(M)}(t; R, v)$. We denote the length of the interpulse period by P. The non-coherent integration means the computation, and maximization over the range and velocity parameters, of the non-coherent match function $\mathrm{MF_{nc}}$

$$\mathrm{MF_{nc}}^{(M)}(t; R, v) = \sqrt{\frac{1}{M}\sum_{m=0}^{M-1}\left[\mathrm{MF}^{(1)}(t + mP; R, v)\right]^2}. \tag{2.34}$$

This is a smoothed version of (any of) the single-pulse $\mathrm{MF}^{(1)}(t; R, v)$. Therefore, the maximum value of $\mathrm{MF_{nc}}(R, v)^2/\sigma^2$ is roughly equal to the sum of the background level (unity) and the mean of the energy-to-noise-ratios $\mathrm{ENR}^{(1)}$ computed separately for each IPP,

$$\frac{\max_{v,R}(\mathrm{MF}_{\mathrm{nc}}^{(M)})^2}{\sigma^2} \approx 1 + \frac{\sum_m \mathrm{ENR}^{(1)}(t + mP)}{M} = 1 + \frac{\mathrm{ENR}}{M}. \tag{2.35}$$

We denote the mean energy-to-noise ratio per-pulse by $\mathrm{ENR_{nc}}$,

$$\mathrm{ENR_{nc}} \equiv \frac{\mathrm{ENR}}{M} = \frac{1}{M}\frac{E_s}{kT_{\mathrm{sys}}}, \tag{2.36}$$

where, as before, E_s is the total signal energy during the M-pulse integration. We refer to $\mathrm{ENR_{nc}}$ as the "energy-to-noise ratio in non-coherent integration". Then we can write, precisely analogously to Eq. (2.13),

$$\widehat{\mathrm{ENR}}_{\mathrm{nc}} = \frac{\max \mathrm{MF_{nc}}^2}{\sigma^2} - 1. \tag{2.37}$$

For a given signal, the relation between the expected maximum value of the non-coherent match function and the maximum value of the coherent-match function is

$$\frac{\max \mathrm{MF_{nc}}}{\sigma} \approx \left[1 + \frac{1}{M}\left(\frac{\max \mathrm{MF}^2}{\sigma^2} - 1\right)\right]^{1/2}. \tag{2.38}$$

For example, with an $M = 150$ (0.3 s) integration in the MANDA experiment, a signal that is just at the standard detection threshold 5.0 in coherent integration, would give $\max \mathrm{MF_{nc}}/\sigma \approx 1.08$ in 0.3 s non-coherent integration. Non-coherent integration is less sensitive than coherent integration, and such a signal would not be detectable in the non-coherent integration; a higher threshold than implied by Eq. (2.38) must be used to avoid an excessive number of false alarms. In the the next two sections we address the question of setting the detection threshold in non-coherent integration and determine the resulting detection sensitivity.

2.5. Probability of false alarm in non-coherent integration

We want to set the detection threshold in non-coherent integration to correspond to the same false-alarm time, about 20 hours, that we use in coherent integration. We need the probability of false alarm as function of the threshold Θ,

$$P_{\mathrm{fa}}(\Theta) \equiv \mathbb{P}(\max_{k,j} \frac{\mathrm{MF}_{nc}^2(j,k)}{\sigma^2} > \Theta^2 \,|s = 0). \tag{2.39}$$

Again, we can only handle properly the case of fixed range gate Rj. A velocity slice of $\mathrm{MF_{nc}}$ is now the r.m.s of the M spectra of noise-only individual pulses, of length L samples each, normalized by the noise variance, and is of the form

$$\frac{\mathrm{MF_{nc}}(j,k)^2}{\sigma^2} = \frac{1}{M}\sum_{m=0}^{M-1} |\Gamma(m;j,k)|^2 \,, \tag{2.40}$$

where $k \mapsto \Gamma(m;j,k)$ is the spectrum at range Rj, computed using the discrete Fourier transform from the data of the mth IPP. The random variables $\Gamma(m;j,k)$ are complex gaussians, with zero mean and unit variance. For fixed j, they are independent variables with respect to both m and k. As before, we assume that only $N_v \leq L$ spectral points are included in the search for the MF maximum, depending on the desired velocity interval. We use the following result: If Z_m are M independent complex gaussian random variables, with zero mean and unit variance, the real random variable

$$X = \sum_{m=0}^{M-1} |Z_m|^2 \tag{2.41}$$

has the cumulative probability density

$$F_X(x,M) \equiv \mathbb{P}(X < x) = \frac{\gamma(x,M)}{(M-1)!} \equiv \gamma_{\mathrm{inc}}(x,M)\,,\; x \geq 0\,. \tag{2.42}$$

The incomplete gamma function $\gamma(x,a)$ is the integral from 0 to x of $t^{a-1}\mathrm{e}^{-t}$. In Matlab, $F_X(x,M)$ is evaluated by GAMMAINC(x,M). Note that the factorial in the nominator is included in GAMMAINC and in our γ_{inc}. The false alarm rate, with the range gate known a priori, becomes

$$P_{\mathrm{fa}}(\Theta) = 1 - \left[\gamma_{\mathrm{inc}}(M\Theta^2, M)\right]^{N_v}\,. \tag{2.43}$$

We will hope that even when we need to search through multiple ranges, we can still use the functional form (2.43) to extrapolate a simulated data set from small values of Θ to the value we actually need. For the extrapolation purpose, we adopt a two-parameter model based on Eq. (2.43), with N and a as the free parameters but M fixed,

$$P_{\mathrm{fa}} = 1 - \left[\gamma_{\mathrm{inc}}(M\frac{\Theta^2}{a^2}, M)\right]^N \approx N\,\gamma^u_{\mathrm{inc}}(M\frac{\Theta^2}{a^2}, M)\,. \tag{2.44}$$

Here $\gamma^u_{\mathrm{inc}}(x,a) \equiv 1 - \gamma_{\mathrm{inc}}(x,a)$ is the "upper branch" of the incomplete gamma-function, which in Matlab can be computed by GAMMAINC(x,a,'upper').

Figure 10 illustrates the determination of the detection threshold by a simulation of the MANDA experiment, for integration times $T_{\mathrm{c}} = 0.1$ s and 0.3 s (50 and 150 pulses). We generated a set of noise-only data, performed non-coherent integrations using 200 range gates, formed an experimental $P_{\mathrm{fa}}(\Theta)$ by binning the $\max \mathrm{MF_{nc}}$ values, and fitted Eq. (2.44) to it. We solved the threshold value that corresponds to 20 h false alarm time from the fitted model. For $T_{\mathrm{c}} = 0.1$, we found $\Theta = 1.25$, and for $T_{\mathrm{c}} = 0.3$ s, we got $\Theta = 1.46$. In a similar way, the threshold $\Theta = 1.31$ was determined for $T_{\mathrm{c}} = 0.2$ s.

Contrary to the case of coherent integration, in non-coherent integration the threshold corresponding to a given false alarm time must be computed separately for each integration time. It is inconvenient to always resort to simulation. As in the case of coherent integration, from a few simulations, such as shown in Fig. 10, it appears that, for the

interval of t_{fa} values that we are interested in, we can use Eq. (2.44) with $a = 1$ and $N = N_v \cdot N_g$, where N_g is the number of range gates. This corresponds to assuming that the variables $\Gamma(m; j, k)$ are also independent with respect to the range-index j, and so cannot be a valid strategy in general. For better or worse we nevertheless determine the detection threshold Θ from

$$t_{\mathrm{fa}} = \frac{\lambda}{N_g \, \mathcal{D} \, 4 v_{\max} \, \gamma^u_{\mathrm{inc}}(M\Theta^2, M)} \,, \tag{2.45}$$

where $\mathcal{D}$ is the transmission duty cycle and λ is the radar wavelength. When $M = 1$, Eq. (2.45) reduces to Eq. (2.27) of coherent integration. Eq. (2.45) can therefore be used also for coherent integration, by setting M=1 and interpreting the threshold to refer to MF/σ instead of $\mathrm{MF}_{\mathrm{nc}}/\sigma$. Fixing the false alarm time, perhaps to $t_{\mathrm{fa}} = 20$ h, we can solve the detection threshold numerically from Eq. (2.45) for any specific measurement scheme. Figure 11 on p. 61 shows some examples.

It must be noted, though, that in the few cases where we have tested non-coherent integration with real data, the threshold computed from Eq. (2.45) has been too low, and has to be adjusted slightly upwards. This may have more to do with range-dependent clutter in the data—the clutter seems to be relatively more pronounced in the non-coherent integration than in the coherent integration—than with any inherent inaccuracy of Eq. (2.45).

2.6. Probability of detection in non-coherent integration

Having found the threshold for typical integration times, we can inspect the probability of detection in non-coherent integration as function of signal strength. We need an expression for the probability of detection. Analogously to the development leading to Eq. (2.30), we are now concerned with the cumulative distribution of the random variable X, defined in

$$\frac{\max \mathrm{MF}_{\mathrm{nc}}{}^2}{\sigma^2} \approx \frac{\mathrm{MF}_{\mathrm{nc}}{}^2(R_0, v_0)}{\sigma^2} = \frac{1}{M} \cdot \sum_{m=0}^{M-1} |\, \Gamma(m; j_0, k_0) + \frac{\sqrt{L}}{\sigma} b_m|^2 \equiv \frac{1}{M} \cdot X \,, \tag{2.46}$$

where the random variables Γ are independent complex gaussians with zero mean and unit variance. The signal part, $L|b_m|^2/\sigma^2 \equiv \mathrm{ENR}_m$, is the ratio of the signal energy in pulse m and the noise power spectral density, L is the pulse length in terms of samples, and b_m is the complex-valued pulse amplitude so that $s_m(t) = b_m \chi(t; R_0, v_0)$ is the reception of the mth transmitted pulse in terms of the delayed, Doppler-shifted transmission. In non-coherent integration, one can allow the b_m to be different from pulse to pulse, both in magnitude and phase.

Recalling that for non-coherent integration, we have chosen to express the detection threshold Θ in terms of the square root of the mean (per pulse) energy rather than the total integrated energy, the probability of detection is

$$P_D(\Theta) \equiv \mathbb{P}(\frac{\max \mathrm{MF}_{\mathrm{nc}}}{\sigma} > \Theta) \approx \mathbb{P}(X > M\Theta^2) = 1 - F_X(M\Theta^2) \,. \tag{2.47}$$

The cumulative distribution $F(x)$ of X is a non-central version of the cumulative distribution given in Eq. (2.42), and involves the non-central chi-squared distribution of

$2M$ degrees of freedom. We have not found a closed-form expression for the cumulative distribution in the literature, so the result will be given here as an integral of the probability distribution function $f(x)$. Starting from the standard expression for the non-central chi-squared distribution, $f(x)$ for $x > 0$ can be written as

$$f(x; \mathrm{ENR}, M) = \mathrm{e}^{-(x+\mathrm{ENR})} \cdot \Big(\frac{x}{\mathrm{ENR}}\Big)^{\frac{M-1}{2}} \cdot \mathrm{I}_{M-1}(\, 2\sqrt{\mathrm{ENR}\; x}\,)\,, \tag{2.48}$$

where $\mathrm{ENR} = \sum \mathrm{ENR}_m$ is ratio of the total signal energy to the noise power spectral density and I_{M-1} is the modified Bessel function of the first kind of order $M-1$. It may be noted that, for $M = 1$, Eq. (2.48) reduces to the case of coherent integration, Eq. (2.31); and by setting $\mathrm{ENR} = 0$, one recovers the noise-only distributions needed to estimate the false alarm rates. The probability of detection becomes

$$P_\mathrm{D} = 1 - \int_0^{M\Theta^2} f(x; \mathrm{ENR}, M)\, dx\,. \tag{2.49}$$

We evaluate this integral numerically in Matlab.

2.7. Comparison of coherent and non-coherent integration

The curves in Fig. 12, computed from Eq. (2.49), show the probability of detection in the MANDA experiment for three integration times, both in non-coherent integration and, for comparison, in coherent integration. In the top panel, P_D is plotted as a function of the square root of the total signal energy. We note that, contrary to what happens in the coherent integration, in non-coherent integration the probability of detection is not a function of the total energy-to-noise ratio only. Instead, P_D also depends on the number of pulses integrated when we keep the false alarm time constant—that is why we indicate M and ENR explicitly in Eq. (2.48). Panels (2) and (3) in Fig. 12 show that a longer integration allows smaller targets to be seen than a shorter integration as of course it must. Panel (a) shows that the longer the integration, the more the non-coherent integration wastes detection sensitivity. This reflects the fact that the longer the integration, the more phase information is thrown away in the non-coherent integration.

Panel (b) of Fig. 12 suggests that with a 0.3 s coherent integration we should be able to detect about 5.4 dB weaker signals than with 0.3 s non-coherent integration. But consider the following four problems. First, the much shorter data vectors to be Fourier-transformed in the non-coherent integration allow heavy zero-padding of the input vector. This in practice eliminates the "picket-fence" effect from the non-coherent integration. For the picket-fence effect, subtract up to about 4 dB from the MF maximum. Second, use of the FMF algorithm, instead of the the much-too-slow, but more sensitive, basic MF algorithm, can cause an additional loss of up to another 4 dB. Third, in long coherent integrations—and our typical 0.3 s is long in this sense—several dB can be lost if the attempt to compensate for target acceleration fails. Fourth, when the transmission has two frequency channels (a typical case in EISCAT), the two Doppler-shifted spectral lines tend to separate in a long coherent integration, and cannot therefore add in amplitude, even though they are still kept together in the non-coherent integration by virtue of the lower spectral resolution. For this effect, subtract up to 3 dB from the coherently integrated amplitude. These well-understood sinks of the integrated amplitude can add

up to a 10–12 dB loss in the worst case. It would not be unexpected to lose about half of that on average, that is, effectively all the 5–6 dB theoretical gain provided by this method. When testing target detection on real data sets with both integration schemes, our experience so far has been that both methods detect nearly the same number of targets.

On the other hand, even though coherent integration perhaps cannot be made significantly more sensitive in practice than non-coherent integration in the target detection phase, after the detection, more accurate estimates of target parameters are, in principle, available.

3. Measuring system

3.1. Hardware

3.1.1. The EISCAT UHF radar

Except for a 24 hour test measurement at the EISCAT Svalbard radar (ESR) in November 2005, in all our SD measurements we have used the EISCAT UHF radar (1; 2). The 32 m UHF antenna is a fully steerable parabolic dish, with Cassegrain optics, and features a maximum rotation rate of about 80°/min both in azimuth and elevation. The antenna pointing direction is calibrated using celestial radio sources, and is believed to be accurate better than 0.1° in most directions.[1]

A block diagram of the UHF radar at the Tromsø site is shown in Fig. 13. The Tromsø UHF receiver has a cooled preamplifier, giving a system temperature $T_{\mathrm{sys}} \approx 110$ K, much of which is contributed by the transmission/reception switch necessary to protect the receiver during the transmission phase. The radar's radio-frequency (RF) band is centered at 928 MHz, and there are 14 transmission frequencies available, 300 kHz apart. In the most common EISCAT experiment modes, two frequency channels are used. Recently those have been centered at 929.9 MHz (EISCAT frequency F13) and 930.2 MHz (F14). The RF signal is mixed in two stages to the second intermediate frequency (IF2) band, using local oscillators at 812.0 MHz and 128 MHz, so that F13 maps to 10.1 MHz and F14 to 9.8 MHz. The band is formed by the radar's antialiasing filter, which is 6.8 MHz wide and centered at 11.25 MHz.

In the standard EISCAT data processing, the second IF is digitized by a 14-bit analog-to-digital converter (A/D), which produces a continuous sample stream at the rate of 15 Msamples/s. The stream of IF2 samples is distributed to the multi-channel, VME-based, EISCAT digital receiver, each channel occupying one slot in a VME crate. Custom hardware in each channel performs quadrature detection, followed by sampling rate reduction appropriate to the typical 10–50 kHz final channel bandwidth. The baseband sample stream is buffered, and further processing to averaged sample-correlation products is done on UNIX-based computers.

The EISCAT UHF transmitter consists of a programmable radar controller that generates the pulse patterns at DC level, either uncoded on/off pulses or various classes of binary phase codes; an exciter system that converts the radar controller output to RF around 928 MHz; and a klystron power amplifier that consists of two klystron tubes, in principle capable of delivering a combined peak power of about 2.5 MW. The power during the space debris measurements has been between 1 and 2 MW. The maximum transmitter duty cycle is 12.5%, and duty cycles near this value are also used in most

[1] The UHF antenna has the half power beam width 0.6°. The official EISCAT pointing program uses geocentric cartesian coordinates $x = 2106.791$ km, $y = 734.793$ km, and $z = 5955.183$ km for the antenna, while assuming a reference spheroid with semimajor axis 6378.135 km and semiminor axis 6356.75 km. The corresponding geographic coordinates are latitude 69.586°N, longitude 19.227°E, and altitude 0.086 km.

experiments in practice. The time and frequency base at all EISCAT sites is taken from the GPS system.

3.1.2. The EISCAT Svalbard radar

Since 1996, EISCAT has operated a 500 MHz radar system in Longyerbyen, Svalbard (10). The system has two antennas: a steerable 32 m dish and a fixed 42 m dish, pointed to the magnetic-field aligned direction, as shown in Fig. 14. The location of the 32 m antenna as specified in the EISCAT antenna pointing programs is: latitude 78.153°, longitude 16.029°E, altitude 445 m. The geocentric cartesian coordinates are $X = 1262.647$ km, $Y = 362.744$ km and $Z = 6220.902$ km. The radar has a single transmission system, capable of a peak power of about 1 MW, with the high duty cycle of 25%. The transmission power can be switched to either of the two antennas on pulse-to-pulse basis, by reversing the phase of the RF drive to one half of the 8-module transmitter power amplifier. The normal mode of operation, however, is to alternate between the antennas much less frequently, typically once every few seconds. A special problem at the ESR is ground clutter, for, as hinted by Fig. 14, the radar has an unhindered field of view over a fjord to a mountainous landscape reaching to the distance of more than 70 km. Figure 15 shows a block diagram of the ESR system and the connection of the SD receiver.

3.1.3. The space debris receiver

Figure 13 shows the main blocks of the SD receiver, connected to the EISCAT UHF system at the Tromsø site. The arrangement at the ESR site is quite similar, and is illustrated by Fig. 14 and 15.

The EISCAT standard data processing handles a multi-frequency transmission by feeding the IF2 data to multiple hardware channels, each tuned to a particular center frequency. In the SD receiver, we sample the analog IF2 band fast enough to capture the relevant frequency channels into a single digital stream. We need to take B million complex samples per second (of the demodulated, complex signal), in the minimum, if the spread of frequencies is B MHz.[2]

In addition to the standard reception, our data processing requires that the transmission waveform is measured. EISCAT provides the transmission sample signal (TS) time-multiplexed into the same data path as the reception. The multiplexer switch is controlled by the receiver protector bit ("TX bit"), generated by the EISCAT radar controller microprocessor. We routinely record the receiver protector bit into our data

[2]The tradition at this point is to refer to some form of bandpass sampling theorem, as if "bandpass sampling" were a special form of sampling. This is quite unnecessary. The simple result that covers all cases of uniform sampling is the one expressed, for example, via Eq. (1.29) on p. 27 in the classic book by Oppenheim and Schafer (8). The spectrum $Z(\nu)$ of the digital signal, defined as the Fourier-transform of the sequence of the signal samples $z_n = z(n\tau)$, is the periodic extension, with period $f_\mathrm{s} = 1/\tau$, of the Fourier-transform $Z_\mathrm{a}(f)$ of the analog signal $z(t)$,

$$Z(\nu) = f_\mathrm{s} \sum_m Z_\mathrm{a}([\nu + m] f_\mathrm{s}) \,.$$

The dimensionless variable ν is the normalized linear frequency, $\nu = f/f_\mathrm{s}$. When $Z_\mathrm{a}(f)$ has support only on a frequency interval of width B, the condition $f_\mathrm{s} > B$ ensures that the spectral replicas $Z_m(\nu) = f_\mathrm{s} Z_a([\nu + m] f_s)$ do not overlap, and therefore, information is not lost in the sampling.

stream to mark out the transmission blocks. The bit is stored into the least significant bit of the imaginary part of the $16 + 16$-bit complex integer data words.

The core of the data acquisition system is a custom PCI-board which performs sampling, quadrature detection and sampling rate reduction. The board was developed originally for ionospheric tomography by the now defunct Finnish company Invers Ltd.

The sampling rate f_A of the A/D converter on the PCI board can be programmed (at least) between 40 and 46 MHz. The resulting real-valued sample stream is processed by programmable logic chips, from the Xilinks SpartanXL family, to perform quadrature detection, essentially by doing Hilbert transforms. The result of the transform is a complex-valued sample stream at the sampling frequency $f_A/4$, representing the negative frequency part of the spectral contents of the analog input. The chip then decimates the 10–11 MHz stream to the final sampling rate. A typical decimation factor M is 20. The decimation is done by adding samples in blocks of M; this ensures proper filtering. Because frequency translation from IF2 to baseband is done by undersampling, selection of f_A requires careful consideration, to get the frequency channels to map as near to the zero frequency as possible to minimize attenuation in the decimation filter, while at the same time producing a sensible sampling interval as required by our sample-count-based data addressing. In different experiments, we have used 40, 42 and 44 MHz primary sampling rates, see Fig. 1 and Fig. 2. Any future version of the SD receiver should have a complex mixer built-in. More details about the low-level signal processing done in the SD receiver are given in Appendix A of reference (6).

The PCI board is mounted in a Macintosh G4 workstation, running under the Mac OS X version of UNIX. We call the Mac G4 the measurement computer. In addition, there is a dual-CPU Mac G5 computer for data analysis. The Mac workstations are connected to each other via a gigabit Ethernet link, and are also connected to the site LAN. The measurement computer runs software from Invers Ltd to read the sample data from an onboard buffer and write them to a hard disk, either a local disk, or a disk mounted over the gigabit link from the analysis computer. The data accumulation rate to the disk is between 7 and 30 GBytes per hour (2 to 8 MBytes s^{-1}), depending on the sampling rate. The maximum sustainable transfer rate over the data link in this configuration is more than 20 MBytes s^{-1}, so even 8 MBytes s^{-1} is only a minor load, and does not affect significantly the computing performance of either of the workstations. The LAN connection is used to access the EISCAT process computer, to update the time base in the G4 and G5 once every 5 minutes, using the standard network time protocol (ntp). This ensures that the time base in the Macs stays within 20 ms of the time kept in the EISCAT system. This is more than adequate for time-stamping space debris events.

3.2. Software

An overview of the real-time SD data processing software system is shown in Fig. 16 on p. 66. The system consists of five main processing units and an overall control system. These have been described in some detail in (6), pp. 57–83. Here we give an updated summary. The processing has the following phases.

Sampling and demodulation. The SD receiver's programmable firmware delivers complex-valued baseband samples at a strictly regular rate to a buffer, which is visible in the measurement computer's memory space. The buffer is large enough

to smooth out the less predictable access times of the reading process—which is an ordinary time-sharing UNIX process—so that no samples are lost.

Recording. The recorder program GUMP reads the data from the buffer and writes them to disk files. The sample data are organized into directories which we call the stream directories, or just the streams. Typically, a stream contains 60 minutes of uninterrupted sample flow in time-stamped files, each storing one million complex points as $2 + 2$ byte integers.

Scanning. The streams are processed, one stream at a time, by the SD scanner program DSCAN (Fig. 17). Two scanners can be running in parallel in the dual-processor analysis computer. The scanner reads a segment of raw data from a stream and searches through the segment for hard targets range gate by range gate, performing threshold detection using the FMF algorithm. When a pre-determined threshold is exceeded, we say that we have a hit. The scanner saves the hit's description to a file and proceeds to the next data segment. Scanning is the most time-consuming step in the data processing. DSCAN is implemented as a C program that makes use of the onboard AltiVec vector processor in the G5, by calling routines in Apple's DSP library (vdsp). The scanner performance depends strongly on the length of the input data vector. For the most common configuration (2 μs sampling interval and 0.3 s coherent integration), we get about 2 GFlops mean speed per processor. The output of the scanner is a stream-specific directory in a standard place in the filesystem hierarchy, for example, `/Scans/050921/tau2_2000_cp2pos1/UHF20050921030614/`. The directory contains a list of the streams's hits in the file `out.hlist`, and for each hit, two Matlab-format files that contain information about the $\mathrm{MF}(R, v)$ associated with the hit. The file with a name like `rat_20050921_030659_124.mat` contains the MF "range-profile", the function $R \mapsto \max_v \mathrm{MF}(R, v)/\sigma$. The file with a name like `vel_20050921_030659_124.mat` contains the MF velocity slice through the MF maximum position, $v \mapsto \mathrm{MF}(\widehat{R}, v)/\sigma$. These two files are used by the hit-list cleaning program CLEANSCANS to plot an overview of the match function such as shown in Fig. 4.

Hitlist cleaning. A problem point in our data processing has long been the interface between detection and analysis, the step that involves grouping the detector hits into events. An event is, by definition, those hits that are caused by a single target when it moves across the radar beam. The grouping is handled by the event-archiver program DARC, using *only* a hit list as its input. If DARC manages to produce a "good" event, the analysis programs can in most cases make reasonable sense of it automatically. A hit's description in the hit list contains only the most basic parameters, namely, the time, value and location of the MF maximum. We have found that we can vastly improve the event selection by also taking into account the MF's overall behavior around the maximum point, the information that is available in the `rat_*.mat` and `vel_*.mat` files.

We use the Matlab program CLEANSCANS (see Fig. 18) to remove bad hits from the `out.hlist` hit-list file produced by DSCAN. Early versions of CLEANSCANS just plotted the range profile and velocity slice of each hit; the operator had then to decide weather or not to accept the hit, and for a bad hit, manually remove the corresponding line from the hit-list file. This was acceptable for handling

a few hours of test data, but with hundreds of hours of data manual cleaning was becoming a major bottleneck. Even after we had enhanced CLEANSCANS for point-and-click hit-removal, cleaning one day's worth of data still took an hour or so of high-concentration work. Next we tried using the variance of the range profiles and the velocity slices to automate the hit removal. That produced a lot of spaghetti-code but did not really improve the success rate.

The most common causes of bad hits are range aliased targets and targets which attain their maximum signal strength when the receiver is muted due to ongoing transmission. The problem is that in both case DSCAN triggers on a point which actually is not the true, global, MF maximum, and this results in a misleading estimate of the target range and velocity that we use in event forming. But then M Markkanen of Eigenor suggested that we might be able to discern which of the threshold-exceeding apparent maxima was the true maximum, by making better use of a special property of the MF in EISCAT. With the phase codes that EISCAT customarily uses nowadays, the maximum of the MF range profile is a very narrow (corresponding to the width of a single bit of the phase code) and high spike (compared to the local background), such as shown in Fig. 4. That is, a valid maximum not only exceeds the detection threshold, but, crucially, exceeds it much more than its immediate surroundings. By making use of the width of the observed spike, both in the range and the velocity direction on one hand, and by inspecting the level and variance of the local background, CLEANSCANS can now quite reliably decide when a hit represents a true MF maximum. Hits which do not represent a true maximum are disregarded.

Event archiving. The next module in the processing chain, the event archiver DARC, inspects the stream's cleaned list of hits, and combines to an event the hits that correspond to a single target passing through the radar beam. Having determined the time boundaries of the event, the archiver copies the event's data to a separate event directory. The event archiver is a C program, but it is not performance critical. Most of its time goes to data copying, so its speed is mainly limited by disk speed. We have archived the raw data for all events from all our measurement campaigns so far, less than 500 GB.

Parameter estimation. As the last step, the analyser program DANALYSER, outlined in Fig. 20, picks events from the event directories and deduces and saves the event parameters. The analyzer calls DSCAN to re-scan the data using FMF, but with maximum time and range resolution, over a narrow range interval, and to make linear or quadratic fits to the range and Doppler-velocity time series. The range and velocity parameters that we normally quote are taken from these fits, for the time instant of maximum signal strength. The analyser is a Matlab program. The analysis results are written to separate event-specific analysis result directories, see Fig. 20 and Table 3. Also the fit plots for each event are saved to the analysis result directory. An example of such an "event summary plot" is shown in Fig. 21. For kind of "quicklook" access, the results are also collected to summary files, (mostly) on a daily basis. We call these summary files "event parameter lists". They contain the same fields as shown in Table 3, one event per line. An example of such a file on the CD is the file `050811_manda/050812/manda_2000_fmf/events.txt` which contain the event parameters from the August 2005 MANDA campaign, for the day August 12th.

The five main processing blocks run as independent, stand-alone UNIX timesharing processes, which do their specific job once and then die. The processes themselves do not know anything about each other. The processing chain is created and organized by software that we call DROS. The name DROS is a modified version of "eros", and is meant to indicate that the system is a slightly tailored copy of the standard EISCAT real-time radar operating system. Based on an experiment-specific configuration file and a given start time, the DROS system generates the required input files and command line parameters for the processing modules, starts and restarts the processes in the two computers as required, and maintains and logs state information. The DROS system can query the running EROS at the host radar to find the antenna pointing direction and transmission power information. It is also possible to run each processing component separately via a script.

4. Measurements

In this chapter, we give an overview of the four space debris measurement campaigns conducted in 2005 at the EISCAT radars. In accordance to our ESA contract, the 700 hours of measurement, producing about 8000 debris events, were conducted in parallel with standard EISCAT common mode (CP) ionospheric measurement campaigns, using the space debris receiver for data collection.

Manda campaign 11–13 August at EISCAT UHF radar in Tromsø. The 51 hour continuous run produced 806 debris events. The UHF antenna was parked to the magnetic field aligned direction during the run.

Cp2 campaign 7–29 September at EISCAT UHF radar. From the 545 h measurement, we report here 5151 events, from four antenna parking directions.

Tau0 campaign 11 November at EISCAT Svalbard radar. This 24 hour test measurement produced 650 "normal" events and 456 "bonus" events (these terms will be explained below).

Manda campaign 17–20 November at EISCAT UHF radar in Tromsø. The 79 h measurement produced 1349 events. The UHF antenna was parked to the magnetic field aligned direction during the run.

The raw data of all the events, 330 GB, have been saved to disk. The event parameters in the format described at the end of section 3.2 are available on the CD associated with this report. In the next several subsections we describe the measurement modes and summarize the measurement results via campaign-wide overview plots of the basic measured parameters.

4.1. Manda campaigns in August 2005 and November 2005

The structure of the MANDA raw data is shown in Fig. 1. Conceptually, the experiment is one of the simplest in current use in EISCAT. There is only a single frequency channel. The transmission pulsing is is strictly periodic with interpulse period of 1875 μs. The scheme is intended for the low ionosphere, down to about 70 km altitude, and provides high spatial resolution. The transmission cycles through a set of 128 different phase codes, each $64 \times 3\,\mu$s long. The codes are sufficiently different to alleviate the problem of range-aliasing so that one gets unambiguous range to very long ranges. To get coverage throughout LEO, we searched for the return echo in the first seven IPPs after a given transmission. The antenna was parked along the Tromsø magnetic field-aligned direction, azimuth 184.1° and elevation 77.4°. In EISCAT, this pointing geometry is referred to as the CP1 mode. For the MANDA transmission, the CP1 geometry results in blind zones in LEO at the ranges 0-68 km, 251 - 349 km, 532-631 km, 813-912 km, 1095-1193 km, 1376-1474 km, 1657-1755 km, and 1938-2000 km, see e.g. panels (c-d) in Fig. 23. In the MF detection scheme the edges of the blind zones are, in effect, somewhat "fuzzy",

because one can accept that some part of the returned echo is blocked by a transmission period and some part is visible. The blind zones quoted above correspond to ranges where at least some part of the echo is blocked. In the analysis phase, when we are analyzing an event near a blind zone edge, we allow a slight (a few samples) incursion into the blind zone, and drop the event only if the signal strength does not peak very soon after entering the zone. The edges can cause problems in data interpretation. In this report, when we have binned data in range or altitude bins, we have not corrected for some of the bins partially overlapping the blind zones. In histograms such as shown in panels (e-f) of Fig. 24, cross-hatching overlapping a histogram bar is a warning that the particular bar may be affected by reduced statistics.

In both MANDA campaigns, the SD receiver was taking primary complex samples, at a rate of 10.5 MHz, of the MANDA IF2 analog signal centered at 10.4 MHz; after down-sampling, the data were recorded using 2 μs sampling interval. Target detection was done using FMF with coherent integration of 160 pulses ($T_c = 300$ ms). In DSCAN processing, after each integration, the next 80 pulses were skipped to speed the scanning. For the same reason, only every third range gate, total of 1427, was computed. The velocity interval ± 5 km s^{-1} was monitored.

After detection, cleaning, and archiving, the events were analyzed in several ways. The plots shown in Fig. 23 and Fig. 24 are from analysis done using FMF-based 0.2 s coherent integration. On the CD, this data are in daily event parameter list files, with the names such as `050812_manda/050812/manda_2000_fmf/events.txt`. All the MANDA events were also re-analyzed (but not re-detected) using 0.2 s non-coherent integration. The event parameter lists for these analysis runs are in the files such as `050812_manda/050812/manda_2000_nci/events.txt`. The events on August 11th were also analyzed with the MF, event parameter list is `050811_manda/050811/manda_2000_mf/events.txt`, as well as with half a dozen different choices of integration times and the extent of zero-padding in the Fourier-transform. Event parameter lists of these variations are in subdirectories of `050811_manda/050811/`.

Both of the MANDA campaigns were scheduled for the time of a meteor shower. Even though the coherence time of meteor echoes is short, and the typical radial velocity much higher than the ± 5 km s^{-1}, it turned out that several tens of such echoes were picked up, all below 150 km altitude, in the standard detection scans. In order not to distort SD event count by meteor events, it was necessary to restrict plotting and event counting to altitudes larger than 150 km. The meteor events have not been removed from the event parameter lists, though. We re-scanned the recorded data with DSCAN better optimized for high-velocity targets with short coherence time. We used the FMF algorithm but integrated coherently only over four pulses. We also used the maximum velocity window allowed by the 2 us sampling rate. We analyzed the events using non-coherent integration of two pulses. We refer to these events as MANDA-METEOR events; they have been archived separately from the standard space debris events. In the August MANDA-METEOR data we found 2201 events, or 43 events per hour; and in the November data, 3653 events, corresponding to 46 events per hour. On the CD the meteor event parameters are in the daily files `05MMDD_manda/05MMDD/manda_2000_meteor_nco/events.txt`.

Our analysis of the meteor events is good for quick-look purpose at most. For instance, velocity wrapping should be done more carefully. The extend of velocity values in the data is larger than the about ± 40 km s^{-1} that can be fitted in a single Nyquist zone when using 500 kHz sampling on a 930 MHz radar. In the analysis, we have mapped

events with an apparent v_r larger than $+10\ \mathrm{km\,s^{-1}}$ to $v_r - 80\ \mathrm{km\,s^{-1}}$. The RCS estimates given in the listings assume, in addition, that the target is at the beam center and that the signal is coherent over the pulse duration. A few examples of the meteor data from the November 2005 campaign are in Fig. 25 on p. 73.

4.2. CP2 campaign in September 2005

The EISCAT common mode experiment CP2 has a six-minute, four-position antenna scan, illustrated in Fig. 26. The transmission scheme in the September measurement was the TAU2 pattern, which uses two frequency channels, see Fig. 2 and Fig. 22. The EISCAT measurement was started on September 2nd, but due to problems with the transmitter, stabilized to more or less continuous operation only on September 7th, at which time we joined the run with the SD receiver. It must be said that when EISCAT signed the contract for 2005, we had not anticipated to be required to collect debris data with an experiment where antenna pointing direction would not be fixed. In most years up to 2005, EISCAT has run enough hours with a CP1-type, fixed-position mode, and that is what the debris software has been tailored for. But 2005 was exceptional, and to be able to collect the agreed amount of data, we decided, late in summer 2005, to cover the CP2. It was clear that some hacking in the software was called for. To be able to use as much as possible of the existing software on the one hand, and to save storage space in a long run on the other, we decided to split the data into position-wise streams. Each pointing direction would be recorded into its own, short data stream when the antenna was stationary. The recording would be stopped while the antenna was changing pointing direction, as is indicated in panel (b) of Fig. 26. This would result in four data sets, each corresponding to a complete, standard-format, stand-alone beam-park experiment, readily manageable with the existing SD software.

With hindsight, stopping the recording every so often to save 30% of temporary storage was a wrong decision. It would have been better to keep the recording running all the time, as we normally do, and just pick the desired data in the analysis phase. Now, due to a programming error in the poorly tested software which was taking care of the stopping and starting of the recording, the recording slipped out of synchronization with the antenna motion loop, as is shown in panel (c) of Fig. 26. JM's log notes from the night on September 20th when he finally noticed that the recording was going badly, and the actual offending piece of code, are reproduced in Figs. 27 and 28.[1] The net effect of the error was that from the beginning of the campaign until 02 UT on September 20th, we recorded only 48 s in position 1 in each passage of the pointing loop, while we could have been recording 76 seconds. During the campaign, we got 1460 events in position 1, so taking into account the two different recording duty cycles, 13.3% with the bug (13.1 days), and 21.1% without (9.9 days), we estimate that we lost about 400 events, or 8% of the total of 5150 events in the 23 day long campaign.

The data were both detected and analyzed with the FMF algorithm, using 0.3 s coherent integration in the detection and 0.2 s integration in the analysis. The event parameters are in daily files on the CD, with file names `0509DD_cp2/0509DD/tau2_2000_cp2posN/events.txt`. We run the analysis indiscriminately on all recorded events, thereby including in positions 2–4 some events that had been inadvertently recorded

[1] JM has kept manual notes during all the SD campaigns. For the 2005 runs, these are available on the CD, in the campaign-wise `info` directories.

when the antenna was slewing. We have not counted the offending events into the reported total number of events, and have not plotted them in any of the figures shown in this report; those events were removed by the plotting program DPLOT_CP2_EVENTS.M, based on the events' time stamps. This was readily done with reference to Fig. 26, for the CP2 experiment is synchronized to a full-hour boundary. For convenience, the directory `050906_cp2/info/` on the CD contains Matlab files `pos1.mat` ...`pos4.mat`, which contain only the valid events of the campaign. When plotting event rates in terms of the number of events per hour per bin, as e.g. in Fig. 30, we have scaled the directly measured event rates by the position-wise recording duty-cycles. We have labeled the y-axis with "N_{eff}/hour/bin" in this case.

In the CP2 campaign, the SD receiver used a primary sampling rate of 10 MHz in terms of complex samples, so that the two IF2 frequency channels at 10.1 MHz and 9.8 MHz were mapped to 100 kHz and (-)200 kHz in the undersampling by 20 to the final 500 kHz sampling rate, as shown in Fig. 2. Detection used 56 pulse (312 ms) coherent integration. After every detection scan, 32 IPPs were skipped. The blind zones in LEO are in the ranges 0–345 km, 735–960 km and 1575–1899 km. We extended the scanning slightly beyond LEO, to 2409 km range, but that did not gain many extra events, see Fig. 33 and Fig. 30.

Figure 30 shows that in spite of the blind zones, due to the different elevations in the four parking positions, the experiment manages to sample the debris distribution peaks at around 1000 km and 1500 km altitudes. It is somewhat puzzling, though, why the duty-cycle corrected event rate at altitude 1000 km in Fig. 30 is significantly smaller in positions 3 and 4 than in 1 and 2.

It may be noted that there is considerable amount of structure in the velocity scatter plots of Fig. 35. The routine analysis computes target velocity directly from the Doppler-shift, as in Fig. 35, but also, as in Fig. 36, from the time derivate of the range data. Unsurprisingly, the Doppler-data has significantly less noise.

Figure 34 shows the radar cross section, computed from Eq. (2.15). The cross section is converted to effective diameter in Fig. 33, using a simplified formula for the cross section of a conducting sphere. Figure 31 shows the range-integrated size distribution. There is some kind of discontinuity at 6 cm size. This feature is visible in all our EISCAT UHF data, independently of the experiment, and shows up clearly as a "layer" in the scatter plots such as Fig. 33. In our earlier reports we have interpreted the discontinuity as an artifact of the simplified cross section model, where we ignore the resonance region by artificially joining the Rayleigh and optical regions at about this target size. This still seems the most probable interpretation, but the matter would seem to merit a more thorough inspection, for one can imagine that some kind of range-independent discontinuity is present already in the cross section data in Fig. 34, at about the corresponding position.

4.3. Test measurement at ESR in November 2005

So far during our SD work, all the measurements we have been reporting have been done at the 930 MHz UHF radar in Tromsø. This radar has long been the main instrument also for EISCAT's normal work, but the situation seems likely to change in the near future as the emphasis of EISCAT operations is expected to shift over to the 500 MHz Svalbard radar. Due to the longer wavelength, one would expect the ESR system to be less sensitive for small targets than the UHF system, as suggested by panel (a) of

Fig. 5. According to Tables 2 and 1 on p. 49, with 0.3 s coherent integration in typical experiments, our standard detection threshold 5 corresponds to 2.7 cm effective diameter at 1000 km range at the 42 m ESR system, and 1.9 cm at the Tromsø UHF. The ESR 42 m antenna has half-power beam width about 0.9° (corresponding to 45 dBi gain), which is somewhat more than the 0.6° (gain 48 dBi) beam width of the UHF antenna, and should help to increase the number of detections. The high latitude of the ESR site could also be expected to boost the number of detections, due to the crowding of polar orbits up there. It was clearly worthwhile to check the debris detection sensitivity of the ESR radar with a test measurement.

EISCAT has in principle two identical copies of the SD receiver. One unit has been installed in Tromsø, and the other has been kept as a spare in Sodankylä. The spare unit was now transported to Svalbard. On November 7th it was connected to the ESR receiver, into the receiver chain coming down from the 42 m antenna as shown in Fig. 15. The SD receiver was configured in the same way as is done in Tromsø: The second analog IF and the radar controller bit that controls the receiver protector were routed to the measurement computer; the analysis computer and the measurement computer were synchronized to the time kept by the site's main computer; and the measurement computer's frequency reference was phase-locked to the radar's 10 MHz frequency reference signal.

EISCAT started a scheduled common mode experiment on November 8th, measuring in CP3 mode, using the TAU0 transmission. As is now perhaps the most typical mode of using the two ESR antennas, in CP3 the 32 m antenna pointing direction is cycled through a 14-position meridian scan. In order not to waste the time intervals when the 32 m antenna is re-pointed—EISCAT does not routinely use data from a slewing antenna—those intervals are used to measure with the non-steerable 42 m antenna. In the CP3 mode, the transmission is switched between the antennas every 64 seconds, and only the recording system associated with the active receiver chain is used at any given time. Because the SD receiver was hooked to the 42 m antenna, we expected to get useful data only for 64 seconds at a time, interleaved with 64 seconds of noise. After the bad experience in the CP2 campaign about the consequences of unnecessarily stopping the recording, we nevertheless decided to keep the debris recording running continuously.

After initial hassle due to the sign of the receiver protector bit being opposite to what it has been on Tromsø, we started collecting SD data on November 9th, using the normal, DROS-controlled recording. To make use of the high (up to 25%) allowed duty cycle of the ESR transmitter, the TAU0 transmission uses two 960 μs phase-coded pulses in a 9 990 μs IPP, on two frequencies, see Fig. 22. The pulses are sent closely after each other, with a 60 μs gap in between; the 60 μs is also the length of a single bit in the 16-bit code. The two frequencies appear at 11.125 MHz and 11.375 MHz in the analog IF2 band. In order for them to map reasonably near to the zero frequency after decimation, the SD used 44 MHz real sampling rate, corresponding to 11 MHz complex sampling rate after demodulation, which was then decimated by 11, to produce a 1 MHz final sample stream for recording. On the ±500 kHz baseband, the carrier frequencies thus appear at 125 kHz and 375 kHz. Especially the latter frequency is considerably attenuated in the filtering associated with the decimation. It would be better if one could map the frequencies symmetrically around zero, but with the present version of the SD receiver which does not have a mixer, this is not practical. The attenuation could in principle be taken into account in RCS estimation as we mentioned in section 2.1 (Eq. (2.11)), but this was not done.

A problem became evident soon after we had started the recording. We had set DROS to produce one hour long data streams; this works nicely in Tromsø. But it now turned out that when DROS tried to re-lauch the recording program in the measurement computer for a new stream, the recorder refused to start, and it was necessary to reboot the measurement computer to get the recording started. We wasted considerable number of measuring hours before finally believing that we had a systematic problem, and that we could do nothing to remedy it. To save the campaign, we gave up having the data in hourly directories and recorded the data in much larger chunks. (There is nothing inherently wrong in long streams, apart from the practical aspect that all our data processing modules use the stream as the smallest data unit, and long streams make interactive inspection of the data awkward.) We have not had the opportunity to inspect what actually went wrong with the SD system at ESR. Even so, the recording problem serves as a reminder that for future work, the SD hardware necessarily must be updated and brought under EISCAT control.

Due to these difficulties, we managed to make only a cursory check of the data during the stay on Svalbard, and had to analyze the data off-line in Sodankylä. We ran the standard DSCAN-CLEANSCANS-DARC-ANALYSIS chain on all the raw data, irrespective of whether the relevant transmission was supposed to be active (transmission on the 42 m antenna) or inactive (transmission on the 32 m antenna). The result was a twofold surprise.

High event rate when the transmission was on the 42 m antenna. When the transmission was on the 42 m antenna, we got more events per hour than we normally observe at the Tromsø UHF radar. Figure 38, panel (a), shows the actual event count per hour, that is, there is no correction for the recording duty cycle. Only those events have been counted that occurred at the times when the transmission was known to be on the 42 m antenna. Obviously, the effective, duty cycle corrected event rate would have been twice as high, about 40 events per hour. That is about 50% higher than we have ever measured at the Tromsø UHF.

High event rate even when the transmission was on the 32 m antenna. Panel (b) of Fig. 38 shows the uncorrected event count for the time intervals when the transmission was known to be on the "wrong" antenna, the 32 m antenna which should have had no connection to the SD receiver. The event count is smaller than on the "correct" antenna, but by no means insignificant. The other panels of Fig. 38 and Fig. 39 show no drastic difference in the parameters of the events between the two data sets, either. We refer to these unexpected events as the bonus events.

We do not know what really caused the bonus events. It is unfortunate that we did not realize this oddity when we were still on Svalbard and could have started finding out. Some events could be due to side-lobe detections, either the 42 m antenna detecting in its side-lobe an echo from a target illuminated by the main beam of the 32 m antenna, or the 42 m antenna detecting in its main beam a target illuminated by a side-lobe of the 32 m antenna. These events are possible, and probably we have some, but we would not expect a great many of them. And we would expect that the different beam directions would show up in the velocity distributions for instance; but this does not appear to be the case. Perhaps a better explanation is the one suggested by A. van Eyken, namely, that the switching of the transmission from the 42 m antenna to the 32 m antenna might not have been perfect. The switching is implemented by changing, in the microsecond

time scale, the relative phasing of the two RF inputs of a four-port switchless combiner that collects the power from the two halves of the transmitter, and should forward it only to one of the antennas, see Fig. 15. The switch might, in effect, be leaking, causing some residual amount of the transmission power to go to the 42 m antenna. In Fig. 40 we deduce a rough estimate of about 10% of the power leaking to the unintended route. This sounds rather high, but perhaps not impossible.

The event parameter list for the ESR test measurement is in the file `051110_tau0/051110/tau0_1000_ch12/events.txt`. The list contains both the proper events and the bonus events. Perhaps the simplest way to separate the two sets is to use the field "TS", the transmission sample power divided by the noise power. For the proper events, that field has value larger than 30. Incidentally, we dare not to use that field to infer the size of the transmission leakage, because unknown system parameters, such as the coupling attenuation at the point where the transmission samples are picked from the antenna waveguide, will affect the TS value.

In conclusion, it is clear that the ESR system is suitable for space debris measurements. As was clear at the outset, the detection sensitivity is slightly lower than we get at the Tromsø UHF, but the good event statistics, the often available long measurements, and the excellent system stability, more than compensate for the handicap caused by the longer wavelength. Encouraged, we are looking forward for opportunities to resume EISCAT space debris measurements, full-scale, and now using the most modern of the EISCAT systems.

Bibliography

[1] M. Baron, The EISCAT facility, *J. atmos. terr. Phys.* **46** (1984) 469.

[2] M. Baron, EISCAT progress 1983–1985, *J. atmos. terr. Phys.* **48** (1986) 767.

[3] ESA Directorate of Technical and Operational Support ESOC Ground Segment Engineering Department Mission Analysis Section, *Study specification, measurements of small-size debris with backscatter of radio waves* (Darmstadt, Germany, 1999).

[4] ESA Directorate of Technical and Operational Support ESOC Ground Segment Engineering Department Mission Analysis Section, *Study specification, real-time space debris detection with EISCAT radar facilities* (Darmstadt, Germany, 2002).

[5] J. Markkanen, M. Lehtinen, A. Huuskonen and A. Väänänen, Measurements of Small-Size Debris with Backscatter of Radio Waves, (Final Report, ESOC Contract No. 13945/99/D/CD, 2002).

[6] J. Markkanen and M. Postila, Real-time Small-Size Debris Detection with EISCAT Radar Facilities, (Final Report, ESOC Contract No. 16646/02/D/HK(CS), 2005).

[7] J. Markkanen, M. Lehtinen and M. Landgraf, Real-time space debris monitoring with EISCAT, Advances in Space Research**35**(2002) 1197-1209.

[8] A. V. Oppenheim and R. W. Schafer, *Digital signal processing* (Prentice-Hall, London, 1975).

[9] M. I. Skolnik, *Introduction to radar systems* (second edition, McGraw-Hill, Singapore, 1981).

[10] G. Wannberg, I. Wolf, L.-G. Vanhainen, K. Koskenniemi, J. Röttger, M. Postila, J. Markkanen, R. Jacobsen, A. Stenberg, R. Larssen, S. Eliassen, S. Heck and A. Huuskonen, The EISCAT Svalbard radar: A case study in modern incoherent scatter radar system design, *Radio sci.* **32** (1997) 2283.

A. Tables and Figures

T_c/s	RCS_1/ mm^2 d_1/ cm	RCS_5/ mm^2 d_5/ cm	RCS_{10}/ mm^2 d_{10}/ cm
0.1	0.41	9.8	40
	1.37	2.32	2.9
0.2	0.21	4.9	20
	1.22	2.07	2.6
0.3	0.14	3.3	14
	1.14	1.93	2.4

(a) Coherent integration.

T_c/s	RCS_{eq}/ mm^2 d_{eq}/ cm	RCS_{th}/ mm^2 d_{th}/ cm
0.1	20.7	23.4
	2.62	2.68
0.2	20.7	14.8
	2.62	2.48
0.3	20.7	11.6
	2.62	2.38

(b) Non-coherent integration.

Table 1.: Some figures of sensitivity for the EISCAT UHF radar at 1000 km range, in a typical experiment such as TAU2, for integration times 0.1, 0.2 and 0.3 s. Table (a) is for coherent integration, table (b) is for non-coherent integration. For coherent integration, the table shows the noise equivalent (integrated ENR = 1) radar cross section RCS_1 and the corresponding target diameter; the cross section RCS_5 corresponding to our standard detection threshold ENR $= 5^2 - 1$; and the cross section RCS_{10} corresponding to an "easy" signal for which ENR $= 10^2 - 1$. For non-coherent integration, the table gives the noise equivalent (ENR = 1 over one pulse, so that also the mean of ENR is unity) radar cross section RCS_{eq}, and the cross section RCS_{th} corresponding to the detection threshold that gives the same false alarm time, about 20 hours, as we use in the coherent integration.

T_c/s	RCS_1/ mm^2 d_1/ cm	RCS_5/ mm^2 d_5/ cm	RCS_{10}/ mm^2 d_{10}/ cm
0.1	0.242	5.80	23.9
	1.89	3.21	4.06
0.2	0.121	2.90	12.0
	1.68	2.89	3.62
0.3	0.0806	1.93	7.98
	1.57	2.67	3.38

(a) Experiment TAU0.

T_c/s	RCS_1/ mm^2 d_1/ cm	RCS_5/ mm^2 d_5/ cm	RCS_{10}/ mm^2 d_{10}/ cm
0.1	0.906	21.8	89.7
	2.36	4.00	5.07
0.2	0.453	10.9	44.9
	2.10	3.56	4.51
0.3	0.302	7.25	29.9
	1.96	3.33	4.22

(b) Experiment STEFFES.

Table 2.: Sensitivity of the EISCAT Svalbard radar when using the 42 m antenna, with coherent integration times 0.1, 0.2 and 0.3 s. Panel (a) refers to the 19% duty-cycle TAU0 experiment, panel (b) refers to the 5.1% duty cycle STEFFES experiment. We refer by STEFFES to the standard experiment STEFFE, shown in Fig. 22 on p. 70, when only the shorter, 480 μs pulse is utilized for debris detection. Even though we do not show any STEFFE data in this report, we anticipate STEFFES becoming the major debris measuring mode at ESR. The panels give the noise equivalent (ENR = 1) radar cross section RCS_1 and effective diameter d_1; the cross section RCS_5 and diameter d_5 corresponding to the standard detection threshold ENR $= 5^2 - 1$; and the cross section RCS_{10} and diameter d_{10} corresponding to a signal for which ENR $= 10^2 - 1$. We have assumed 1000 km range, 1.0 MW transmission peak power, 45.3 dBi antenna gain, and 70 K system temperature.

Table 3.: Event parameter file U20050812_001348_821.epar.

```
%       VS  File format version ID.                                          1
%       NM  Event name UT.                                                   2
%       XI  Experiment ID string.                                            3
%       TM  UT of max Ratio.                                                 4
%       ST  System temperature K.                                            5
%       AG  Antenna gain dB.                                                 6
%       WL  Radar wavelength m.                                              7
%       TX  Transmission power MW.                                           8
%       AZ  Azimuth degr, N=0, E = 90.                                       9
%       EL  Elevation degr.                                                  10
%       RT  Max Ratio ( = estimate of sqrt(SNR_N)).                          11
%       RG  Range km.                                                        12
%       RR  Range rate (km/s).                                               13
%       VD  Doppler velocity (km/s), positive away from radar.               14
%       AD  Acceleration from VD, km/s^2.                                    15
%       DI  Effective diameter cm.  Estimated from ST, PW, RT. RN,           16
%           AG, WL.                                                          17
%       CS  log10 of a lower bound of radar cross sectio cm^2.               18
%           Estimated as DI.                                                 19
%       TS  (Transmission sample power)/(Noise power), dB,                   20
%           arbitrary reference point.                                       21
%       EN  Event number.                                                    22
%       ED  Event duration, seconds.                                         23
%       TP  Transmission sample power, dB, arbitrary reference point.        24
%                                                                            25
%       NaN = Bad.                                                           26
%                                                                            27
%       16-Dec-2005 21:03:52                                                 28
%                                                                            29
VS = 1.1                                                                     30
NM = U20050812_001348_821                                                    31
XI = manda_2000                                                              32
TM = 2005  8 12  00 13 52.669                                                33
ST = 120                                                                     34
AG = 48.1                                                                    35
WL = 0.323                                                                   36
TX = 0.90                                                                    37
AZ = 184.9                                                                   38
EL = 77.4                                                                    39
RT = 13.2                                                                    40
RG = 1936.422                                                                41
RR = -0.956                                                                  42
VD = -0.974                                                                  43
AD = 0.1699                                                                  44
DI = 5.00                                                                    45
CS = 0.999                                                                   46
TS = 11.512                                                                  47
EN = 3                                                                       48
ED = 3.0375                                                                  49
TP = 60.300                                                                  50
```

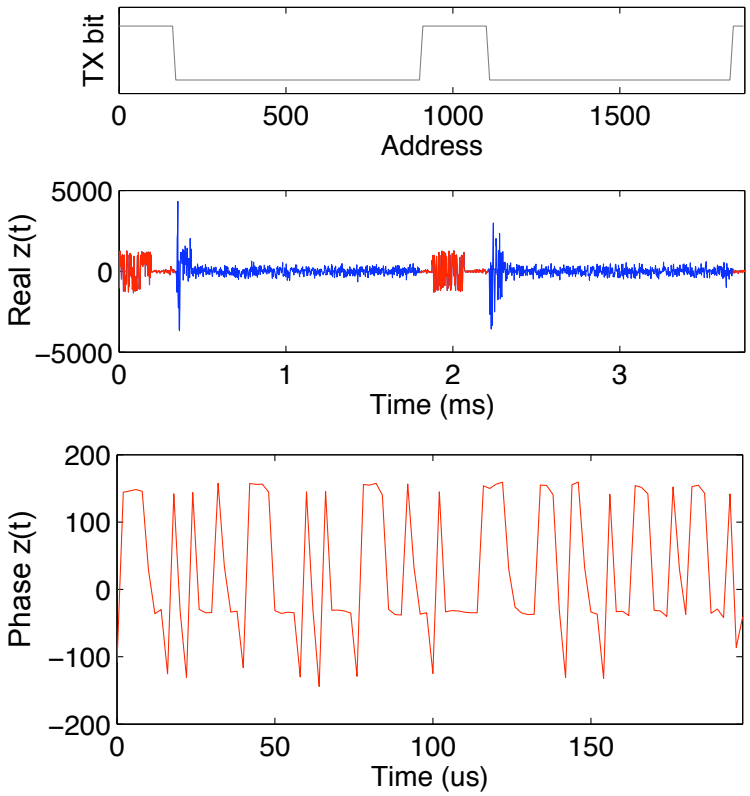

Figure 1.: Structure of space debris raw data in the MANDA experiment. The top panel shows the receiver protector bit, stored in the least-significant bit of the imaginary part of the recorded data. The middle panel shows two 1875 μs long IPPs of the real part of the recorded data, starting from the transmission samples taken from the 192 μs pulse with 2 μs sampling interval. The pulse is phase-coded with baud length of 3 μs, the phase is plotted in the bottom panel after mixing the complex signal from 100 kHz to the zero frequency. The RF frequency in the MANDA experiment is F12=929.6 MHz, which is translated to 10.4 MHz at the second IF. The SD receiver primary real sampling rate is 42 MHz in this experiment, corresponding to 10.5 MHz complex sampling rate after demodulation. This rate is further decimated by 21 in the SD receiver, to produce 2 μs final sampling interval. With this sampling interval, spectral features become periodic by 500 kHz so that 10.5 MHz at IF2 maps to zero frequency and the channel frequency 10.4 MHz maps to 100 kHz at the baseband.

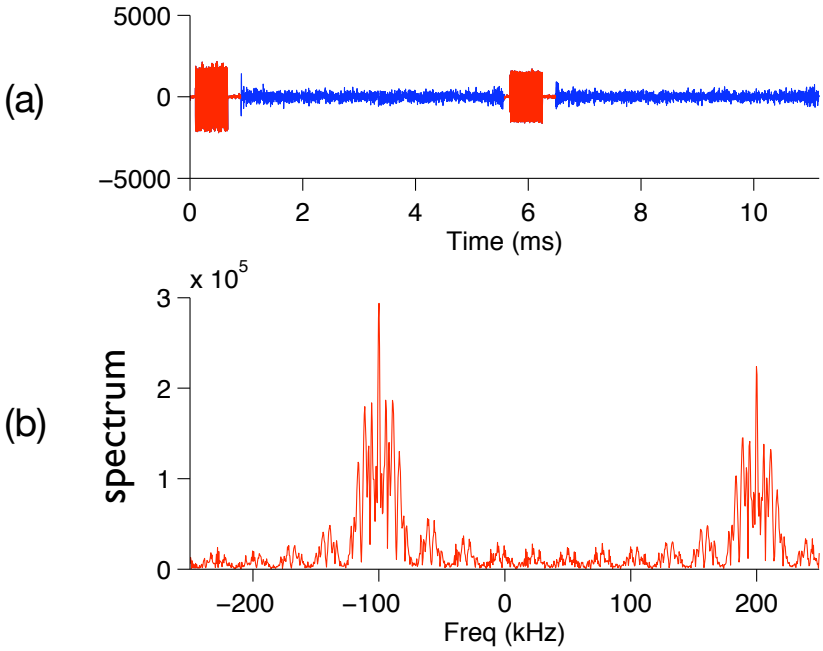

Figure 2.: Space debris receiver raw data in the TAU2 experiment. Panel (a) shows the real part of the stored complex-valued data vector from two 5580 μs IPPs. Both the transmission samples and the actual reception are recorded. Panel (b) is the magnitude of the Fourier-transform of the transmission samples. Both transmitted pulses are 16×32 μs long, the first corresponds to RF frequency F13=929.0 MHz and IF2 frequency -10.1 MHz, the latter to the RF frequency F14=930.2 MHz and IF2 frequency -9.8 MHz. In the space debris receiver, the IF2 band is undersampled to the final sampling rate of 500 kHz, so that F13 maps to -100 kHz at the baseband, and F14 to 200 kHz. The higher frequency is more attenuated due to the filter used in the downsampling. The primary real sampling rate of the analog IF2 band in the space debris receiver is 40 MHz in this experiment. This rate is reduced to a 10.0 MHz complex rate in the Hilbert-transform-based demodulation phase. In this scheme a 10.0 MHz signal at IF2 maps to the zero frequency.

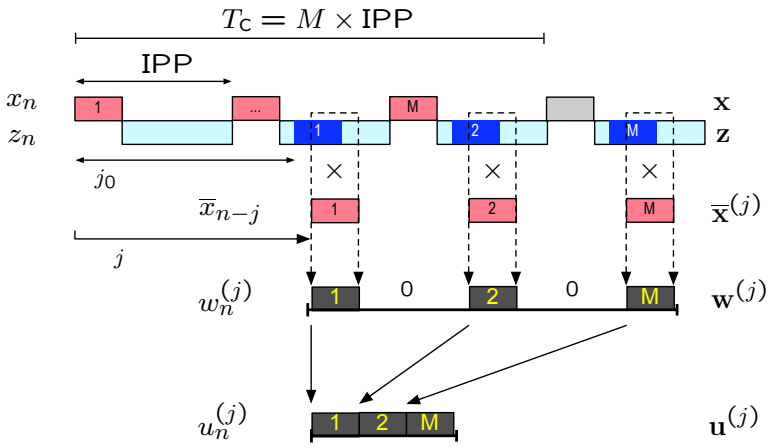

Figure 3.: Coherent integration of M pulses in the MF- and FMF-algorithms. The raw data are the essentially noiseless complex transmission samples x_n and the noisy reception samples $z_n = s_n + \gamma_n$. The diagram also shows the echo of a point-target at range R_{j_0}. To evaluate the match function $\mathrm{MF}(R_j, v_k)$ at range R_j and velocity v_k, the first step is to point-wise multiply the reception sample vector $\mathbf{z}$ with the time-shifted, complex-conjugated transmission sample vector $\overline{\mathbf{x}}^{(j)}$, to produce the vector $\mathbf{w}^{(j)}$. The magnitude of the discrete Fourier-transform of $\mathbf{w}^{(j)}$, normalized by $\|\mathbf{x}\|$, gives a velocity slice of the match function: $\mathrm{MF}(j,k) = |\mathrm{DFT}\{\mathbf{w}^{(j)}\}(k)|/\|\mathbf{x}\|$. Computation of the fast match function FMF has an extra step before the Fourier-transform: the M non-zero blocks of $\mathbf{w}^{(j)}$ are concatenated, to the much shorter vector $\mathbf{u}^{(j)}$. The normalized magnitude of the DFT of $\mathbf{u}^{(j)}$ is a velocity slice of the FMF. The match function maximum position $(\widehat{R}_j, \widehat{v}_k) \approx (R_{j_0}, v_{k_0})$ has the property that all the signal simples s_n add with equal phase, or coherently. The value of the maximum, after background subtraction, is proportional to $\|\mathbf{s}\|$, the square root of the total signal energy.

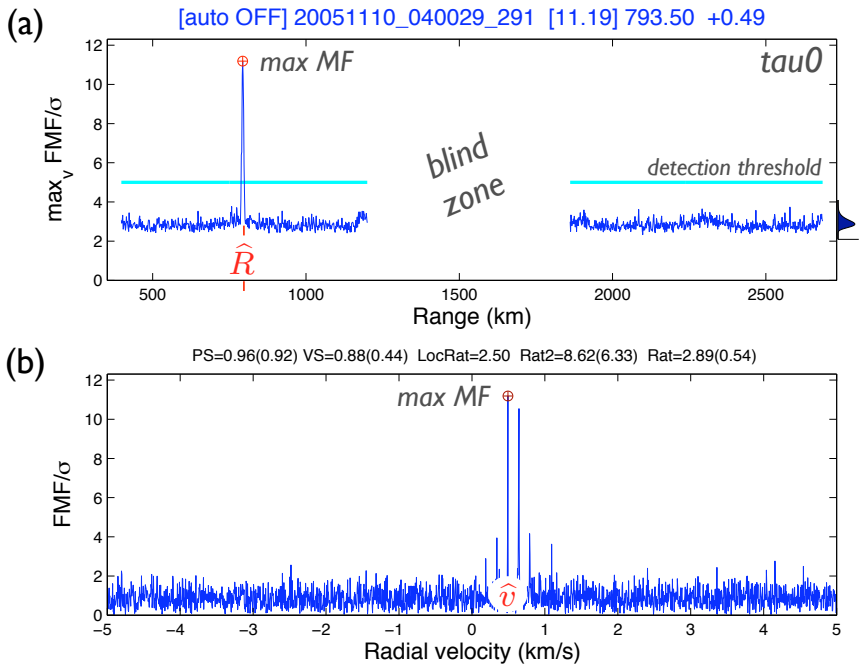

Figure 4.: An example of the fast match function $\mathrm{FMF}(R, v)$ in the TAU0 ESR experiment, showing a detector hit. Coherent integration is 30 pulses or 300 ms. The figure is an annotated version of a standard CLEANSCANS output plot, based on two Matlab files produced by the DSCAN scanner for the detector hit and saved permanently in the `/Scans` directory tree. Panel (a) shows the match function "range profile" $R \mapsto \max_v \mathrm{FMF}(R, v)/\sigma$. Panel (b) shows the velocity slice $v \mapsto \mathrm{FMF}(\widehat{R}, v)/\sigma$ through the match function maximum position. From the considerations in section 2.2, the probability distribution of the variable $\theta \equiv \mathrm{FMF}/\sigma$ in the background part of the velocity slice, the segment outside the signal peaks around 0.49 $\mathrm{km\,s^{-1}}$, should be $f(\theta) = 2\theta \mathrm{e}^{-\theta^2}$. This implies expectation value $\mathbb{E}\theta = \sqrt{\pi}/2 = 0.89$ and standard deviation $\sqrt{1 - \pi/4} = 0.46$. An undisturbed background obeys the prediction well: as shown on the header line of panel (b), the mean value of the velocity slice data is 0.88 and the standard deviation is 0.44, these are estimated by excluding a ± 1 $\mathrm{km\,s^{-1}}$ zone around the maximum position. The probability distribution $g(\Theta_j)$ of the range-profile values, the variables $\Theta_j \equiv \max_k \mathrm{FMF}(R_j, v_k)/\sigma$, is found by differentiation of Eq. (2.24) to be $g(\Theta) = N_v(1 - \mathrm{e}^{-\Theta^2})^{Nv-1} \cdot 2\Theta \mathrm{e}^{-\Theta^2}$, where N_v is the number of points in a velocity slice, which we take to be 1920 in this case. The distribution g is plotted along the right-hand-side y-axis in panel (a), and has maximum at 2.76. The expectation value $\mathbb{E}\Theta_j$, computed using g, is 2.84. The mean value of the data in panel (a), given by the item "Rat" in the header of panel (b), is slightly larger, 2.89, but this number includes also the points containing signal. When those points, and also the points containing calibration noise, just to the left of the blind zone, are removed, the mean becomes 2.79, which is lower than expected. The discrepancy may partially be due to the fact that our actual computation of the FMF is somewhat more complicated than the derivation of Eq. (2.24) assumes.

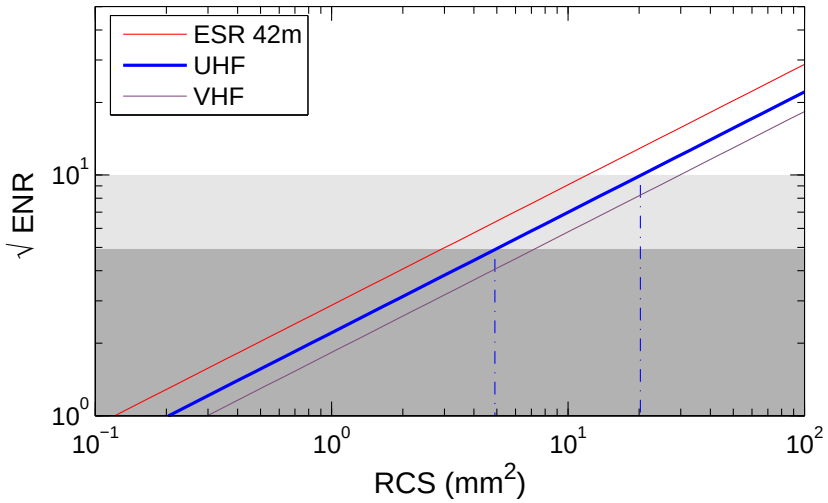

(a) ENR v RCS in typical experiments on three EISCAT radars. Coherent integration T_c=0.2 s and range 1000 km are assumed. ENR = 1 corresponds to noise equivalent signal level (after the coherent integration). Our standard detection threshold is $\sqrt{\text{ENR}} = 4.9$. When $\sqrt{\text{ENR}} > 10$, the signal is already "strong", and is always analyzable.

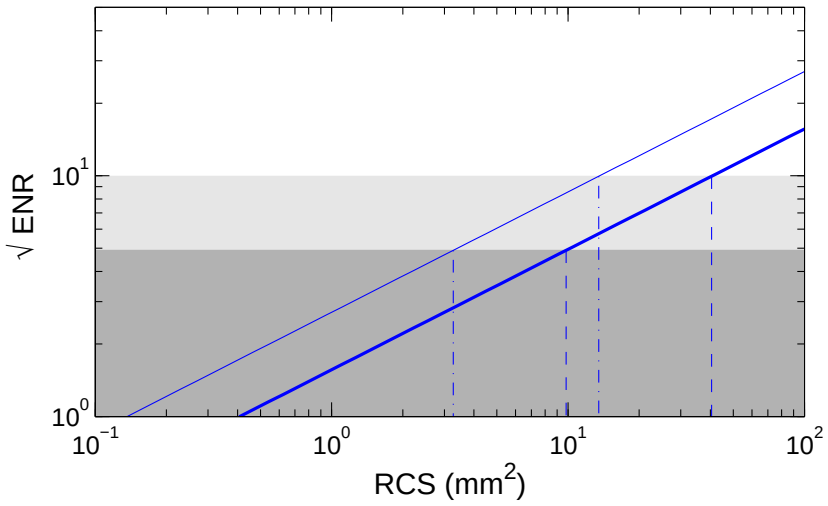

(b) ENR v RCS on the EISCAT UHF radar, for two integration times. The thicker line corresponds to $T_c = 0.1$ s, the thinner line to $T_c = 0.3$ s. Range is 1000 km. An experiment such as tau2 or manda, with about 10.3% RF duty cycle, is assumed.

Figure 5.: Detection sensitivity of EISCAT radars. Panel (a) gives the noise-equivalent RCS; the RCS at the detection threshold; and the RCS for a "strong" signal, for the 0.2 s coherent integration we typically use in analysis. Panel (b) illustrates the effect of varying the coherent integration time.

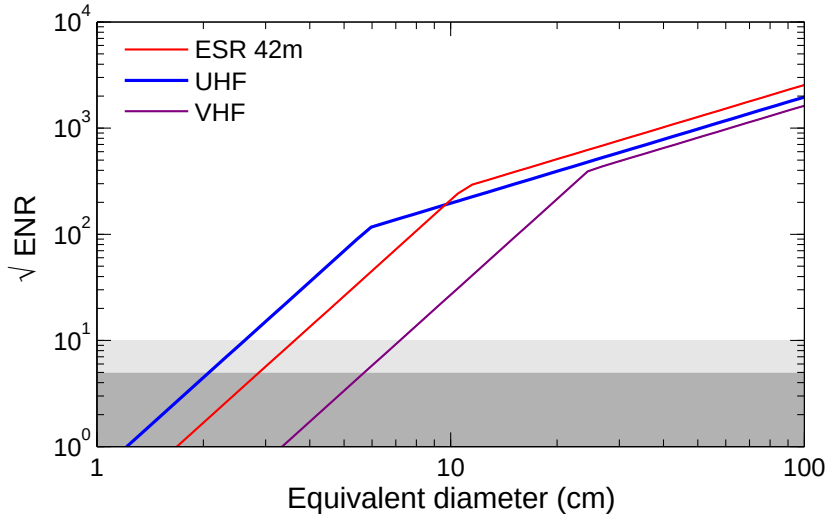

(a) ENR v target's equivalent diameter in typical experiments on three EISCAT radars. Coherent integration T_c=0.2 s and range 1000 km are assumed. ENR = 1 corresponds to noise equivalent signal level. Standard detection threshold is $\sqrt{\text{ENR}} = 4.9$. When $\sqrt{\text{ENR}} > 10$, the signal is "strong", that is, normally easily analyzable.

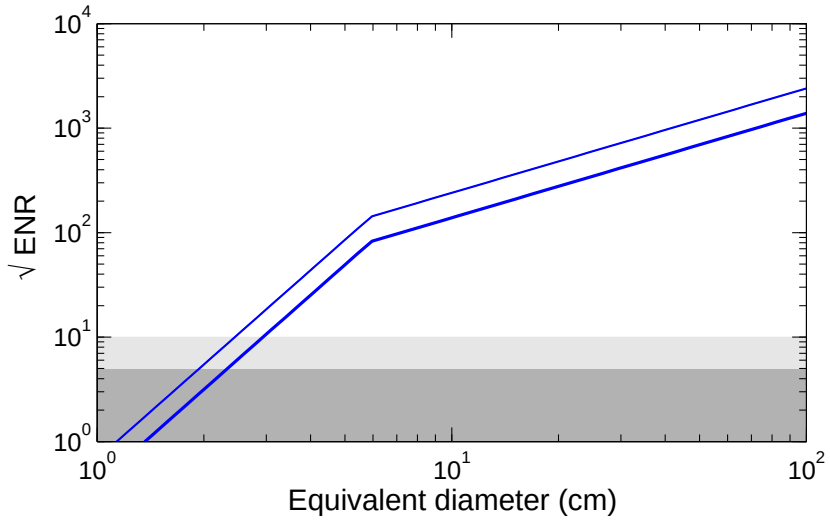

(b) ENR v equivalent diameter on the EISCAT UHF radar, for two integration times. The thicker line corresponds to $T_c = 0.1$ s, the thinner line to $T_c = 0.3$ s. Range is 1000 km. An experiment such as tau2 or manda, with about 10.3% RF duty cycle, is assumed.

Figure 6.: Detection sensitivity of EISCAT radars in terms of equivalent diameter. Panel (a) indicates the noise-equivalent target diameter, the diameter at the detection threshold, and the diameter for a "strong" signal, for 0.2 s coherent integration and 1000 km range. Panel (b) illustrates the effect of varying the coherent integration time at the UHF radar.

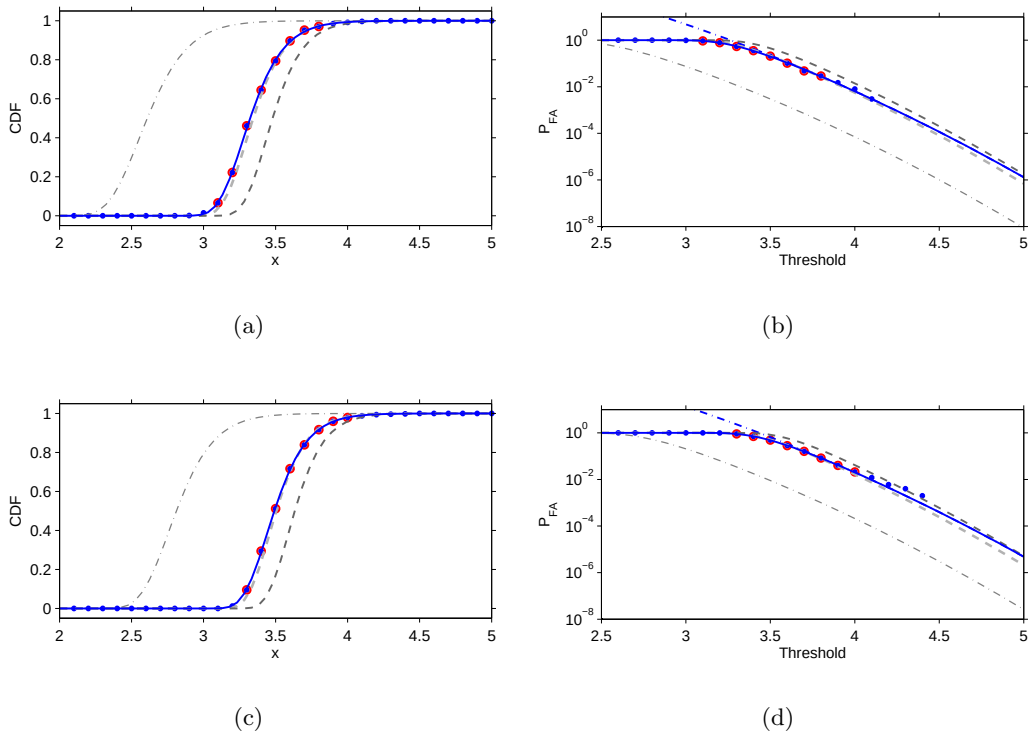

Figure 7.: Probability of false alarm in coherent integration, for two integration times. Panels (a) and (c) give the cumulative probability distribution CPD of the MF maximum value for noise-only data, for integration times 0.1 and 0.3 s respectively. Panels (b) and (d) give the corresponding probability of false alarm, $P_{\rm fa} = 1 - \mathrm{CPD}$. The dots are from a Monte Carlo simulation of a synthetic UHF manda experiment, with 200 range gates (1:3:600) and velocity interval ∓ 5 km s^{-1}. The solid blue line is a two-parameter fit to the circled points. Using the fit to extrapolate to the standard detection threshold 5.0, we find $P_{\rm fa} = 4.8 \times 10^{-6}$ and the false alarm time $t_{\rm fa} = 17.3$ hours for 0.3 s integration, and $P_{\rm fa} = 1.3 \times 10^{-6}$, $t_{\rm fa} = 21.4$ hours for 0.1 s integration. The simulation had 1000 integrations with both integration times. The gray lines are various attempts to approximate the distribution. The leftmost (light gray, dash-dotted) line assumes a single, fixed range in the detection search. The rightmost gray, dashed line (slightly above the fit in panels (b) and (d)), assumes that all the involved MF points would be statistically independent; at the standard threshold, this curve implies $P_{\rm fa} = 5.2 \times 10^{-6}$ and $t_{\rm fa} = 16.0$ hours for 0.3 s integration, and $P_{\rm fa} = 1.7 \times 10^{-6}$, $t_{\rm fa} = 16.0$ hours for 0.1 s integration.

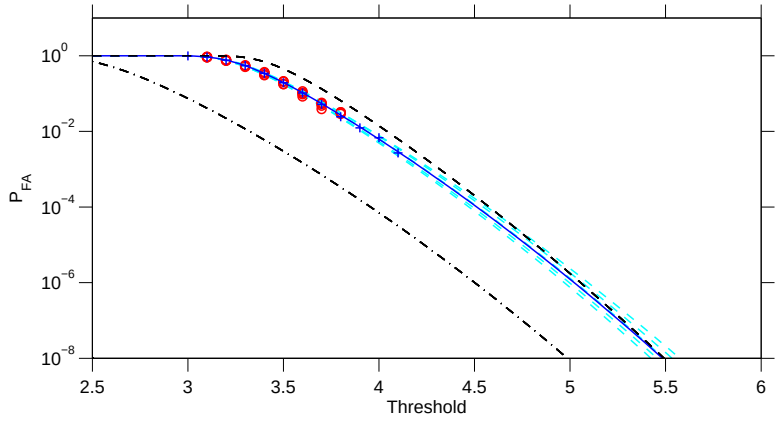

(a) Probability of false alarm in 0.1 s coherent integration.

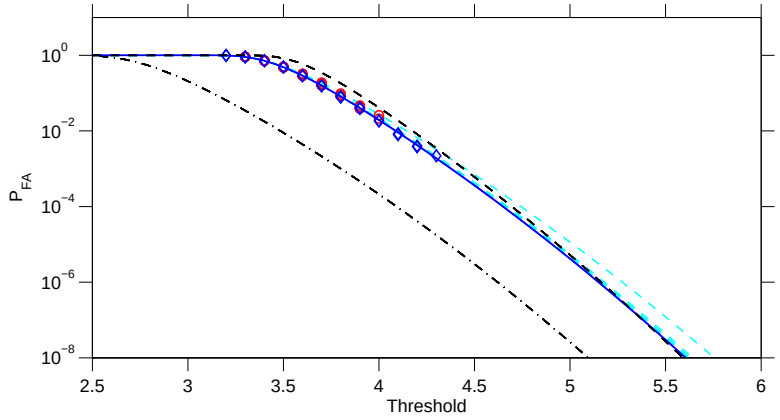

(b) Probability of false alarm in 0.3 s coherent integration.

Figure 8.: Inspecting the accuracy of P_{fa} extrapolation in coherent integration. The simulated experiment is MANDA, and the simulation gives directly P_{fa} up to threshold about 4. We attempt to determine P_{fa} for threshold 5. The light-colored dashed lines show fits of the form Eq. (2.25) to the data (circles) from five 1000-integration simulation. The dashed-dotted line is the theoretical P_{fa} when a target range is known a priori and no search over ranges is needed. The dashed line above the markers is the theoretical P_{fa} of the form Eq. (2.23), if all the used match function points would be independent random variables. The solid line and the diamond-shaped markers are from a longer, 10 000-integration simulation run, which for the bottom panel took 6.9 hours on a 2 GHz Mac G5. From the 1000-integration simulations, we extrapolate $P_{\mathrm{fa}}(5.0) = (1.5 \pm 0.7) \times 10^{-6}$ for 0.1 second integration, and $P_{\mathrm{fa}}(5.0) = (4.0 \pm 1.7) \times 10^{-6}$ for 0.3 second integration. From the longer simulations, we extrapolate $P_{\mathrm{fa}}(5.0) = 1.23 \times 10^{-6}$, false alarm time $t_{\mathrm{fa}} = 22.7$ hours for 0.1 second integration; and $P_{\mathrm{fa}}(5.0) = 4.15 \times 10^{-6}$, $t_{\mathrm{fa}} = 19.0$ hours for 0.3 second integration. The x-axis in the plots is in terms of $\max \mathrm{MF}/\sigma$.

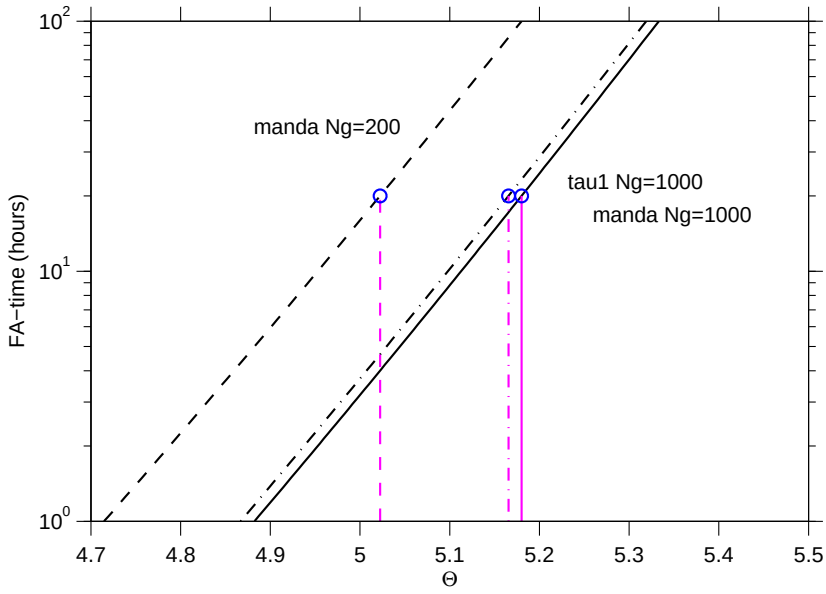

Figure 9.: False alarm time v detection threshold in coherent integration, computed from Eq. (2.27) with ± 5 km s^{-1} velocity interval. The solid line and the dashed line are for a 10% duty-cycle Tromsø UHF or a 20% duty-cycle ESR experiments (such as MANDA and TAU2 on UHF, TAU0 at ESR). The dash-dotted line is for an 8.6% duty-cycle experiment (TAU1) at UHF. N_g is the number of range gates searched.

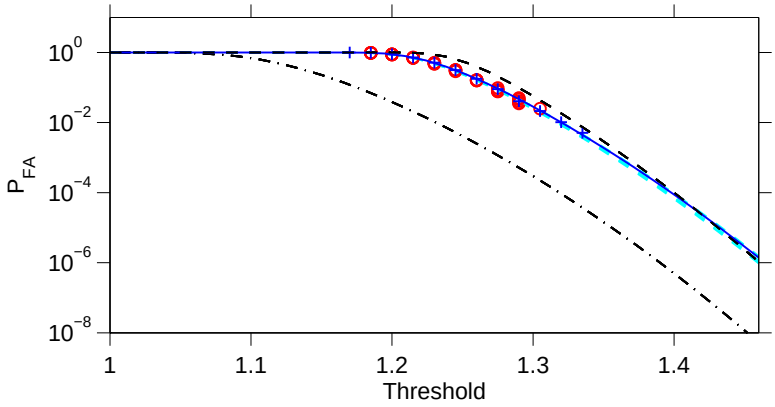

(a) Probability of false alarm in 0.1 s non-coherent integration.

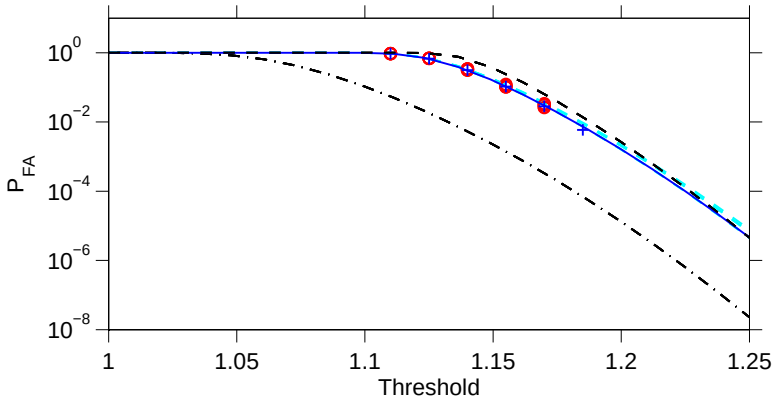

(b) Probability of false alarm in 0.3 s non-coherent integration.

Figure 10.: Extrapolating P_{fa} in non-coherent integration. The dashed lines (cyan) show fits of the form of Eq. (2.44) on the data (red circles) from five 1000-integration runs. The dashed-dotted line is the theoretical P_{fa} when a target need not be searched over multiple ranges. The dashed line above the markers is the theoretical curve computed as if the MF_{nc} points would be independent also in the range direction. The solid blue line and the blue markers are from a 10 000-integration run. From the 1000-integration simulations, we extrapolate $P_{\text{fa}}(1.46) = (1.2 \pm 0.3) \times 10^{-6}$ for 0.1 second integration, and $P_{\text{fa}}(1.25) = (6.0 \pm 1.5) \times 10^{-6}$ for 0.3 second integration. From the longer simulations, we extrapolate $P_{\text{fa}}(1.46) = 1.23 \times 10^{-6}$, false alarm time $t_{\text{fa}} = 22.7$ hours for 0.1 second integration; and $P_{\text{fa}}(1.25) = 4.6 \times 10^{-6}$, $t_{\text{fa}} = 18$ hours for 0.3 second integration. The x-axis in the plots is in terms of $\max \text{MF}_{\text{nc}}/\sigma$.

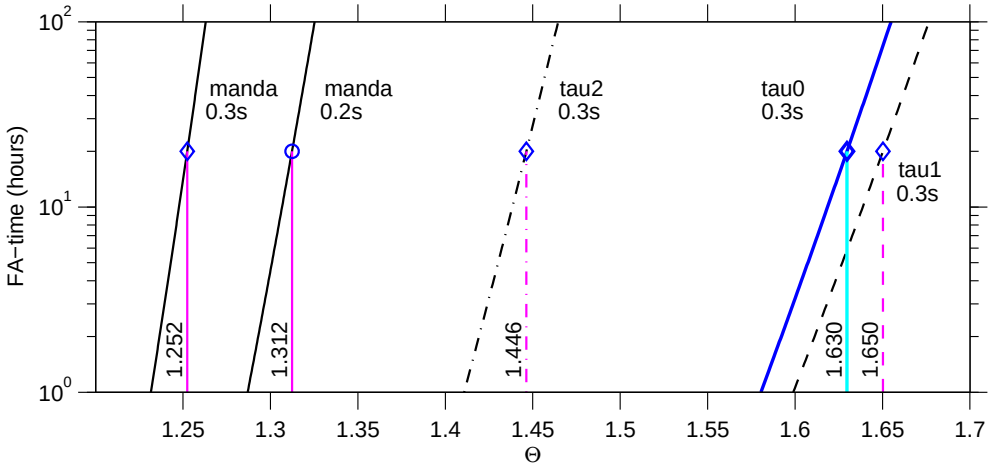

Figure 11.: False alarm time v detection threshold in non-coherent integration, computed from Eq. (2.45). The x-axis is the threshold in terms of $\max \mathrm{MF}_{\mathrm{nc}}/\sigma$.

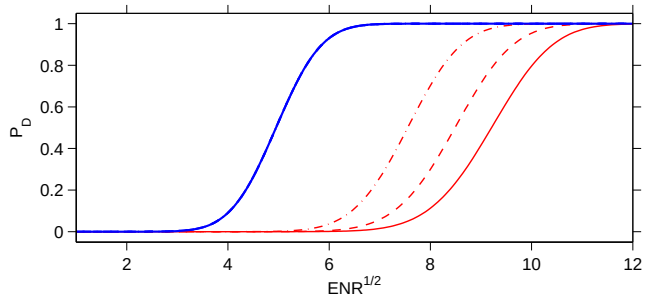

(a)

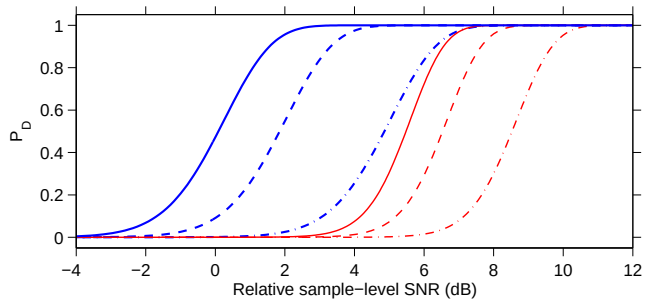

(b)

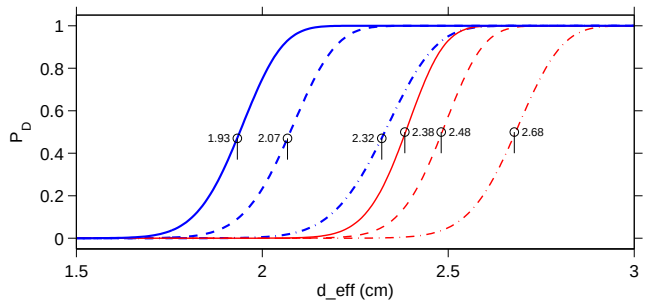

(c)

Figure 12.: Probability of detection in the MANDA experiment. The three panels show the same P_{D} data, computed from Eq. (2.49), but with different choices of the x-axis. In panel (a), the leftmost curve is for coherent integration of any length, followed by curves for 0.1, 0.2 and 0.3 s non-coherent integration. The curves in panels (b) and (c) are, from left to right, for 0.3, 0.2 and 0.1 s coherent integration, and for 0.3, 0.2 and 0.1 s non-coherent integration. In (b), the signal-to-noise ratio SNR means the quantity $|s/\gamma|^2$ computed from unprocessed data $z_n = s_n + \gamma_n$. The reference level 0 dB is the level that gives 50% probability of detection with 0.3 s coherent integration. It can be seen that with 0.3 s integration, coherent integration is about 5 dB more sensitive than non-coherent integration on this measure. In panel (c), target range 1000 km is assumed; the markers give detection-threshold equivalent target diameter. In panel (a), ENR is the total signal energy divided by noise power spectral density.

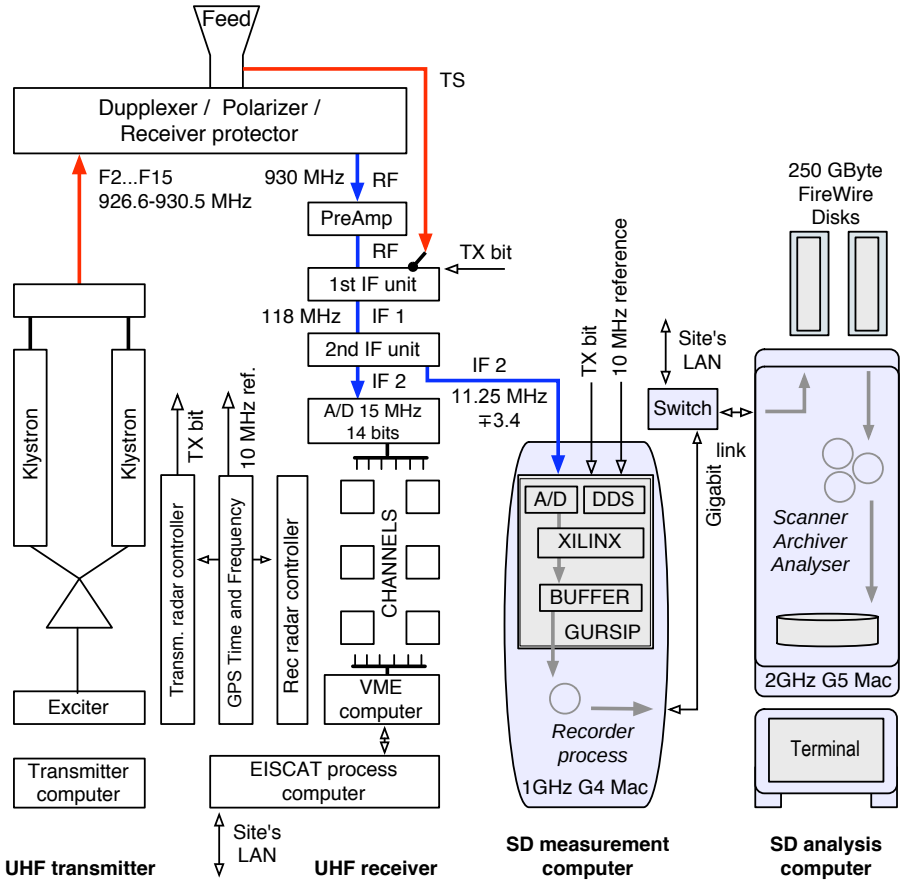

Figure 13.: The space debris receiver connected to the EISCAT UHF radar. The SD receiver consists of a measurement computer and an analysis computer. The measurement computer hosts a custom signal processing board (GURSIP). The primary analog input to the SD receiver is the EISCAT second intermediate frequency (IF 2) band. The input contains, time-multiplexed, both the standard received signal and the transmission sample signal (TS). On the processing board, there is an analog-to-digital converter (A/D) taking 40 megasamples per second; a direct-digital-synthesizer chip (DDS), which provides clock signals on the board, phase-locked to the host radar's 10 MHz frequency reference signal; two Xilinks signal processing chips (XILINX) to perform signal demodulation and sampling rate reduction; and a memory buffer for temporary storage of the samples. The recorder program running on the measurement computer moves the samples over a gigibit network link to an external FireWire disk, mounted on the analysis computer. Target detection is done by the scanner program running on the analysis computer, using the MF-method. After detection, two other software modules, the archiver and the analyser, store away the event's raw data, and estimate and save the target parameters.

Figure 14.: The space debris receiver at the EISCAT Svalbard radar. Panel (a) shows the 32 m fully steerable antenna (left), the site building, and the 42 m magnetic field aligned antenna (right), at the altitude of 420 m on a north-facing slope of the Breinosa mountain, at latitude 78.153°N. Panel (b) shows the Macintosh G5 analysis computer, the console screen and firewire disks in the site's control room. Panel (c) shows the Macintosh G4 measurement computer, with the external connections: gigabit ethernet to the analysis computer (1), IF2 signal from the radar's analog receiver (2), phase-locked 10 MHz frequency reference signal from the radar's frequency distribution system (3), and the receiver protector bit from the transmitter radar controller (4).

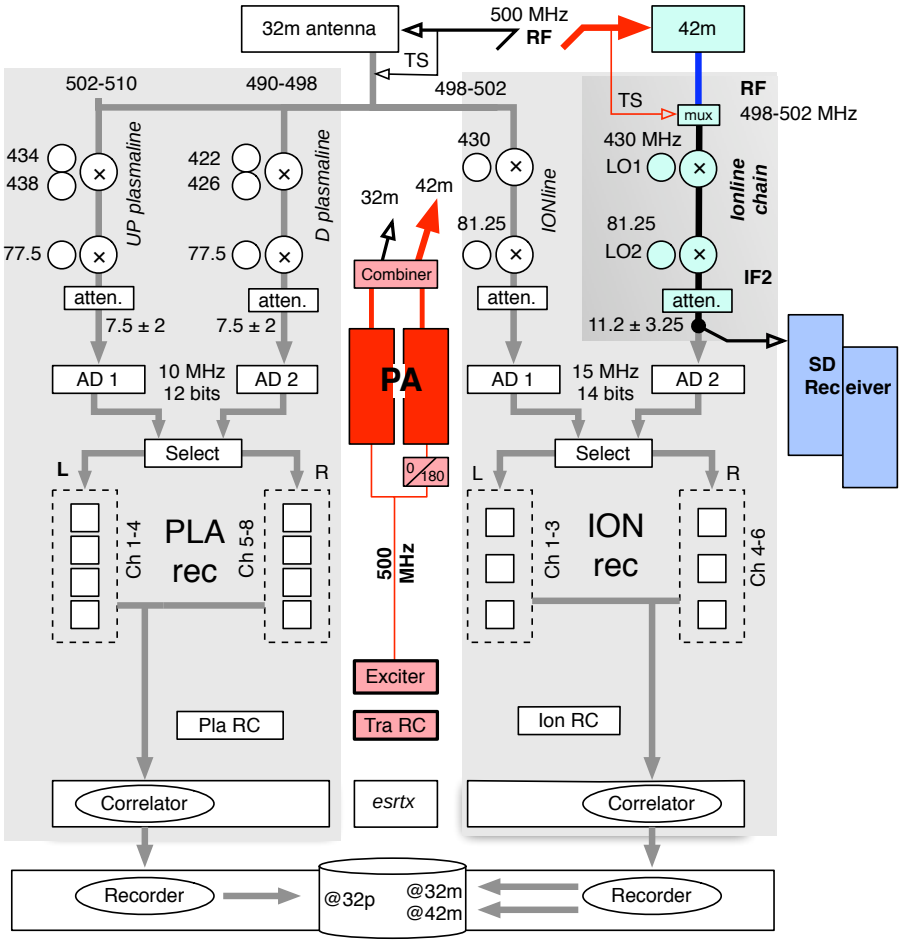

Figure 15.: EISCAT Svalbard radar block diagram, showing the principal data flow during the TAU0 CP3 measurement, from the space debris receiver point of view. The radar has a single transmitter, two antennas, and four complete receiver chains. In the TAU0 CP3 scheme, the transmitter output is switched between the antennas every 64 second. While the transmitter is serving the non-steerable 42 m antenna, EISCAT records data only with the ION receiver, and the 32 m antenna is being pointed to another direction. The space debris receiver, hooked to the second analog IF (IF2) of the receiver chain coming down from the 42 m antenna, records continuously, receiving either the standard echo, or the transmission sample signal (TS). After the 64 second period dedicated to the 42 m system has elapsed, transmission is switched in a few microseconds to the 32 m antenna, by flipping the phase of the exciter output to one half of the transmitter power amplifier, and EISCAT starts recording and transmitting with the 32m antenna. Even though EISCAT is not explicitly making any use of the 42 m system during that time, the ION receiver front-end is kept active, that is, switching between TS-mode and the normal receiving mode. In addition to the analog IF2, the SD-receiver records the control bit (not shown) that switches the system between transmit and receive states. The SD-receiver is phase-locked to the host radar's GPS-derived frequency reference signal.

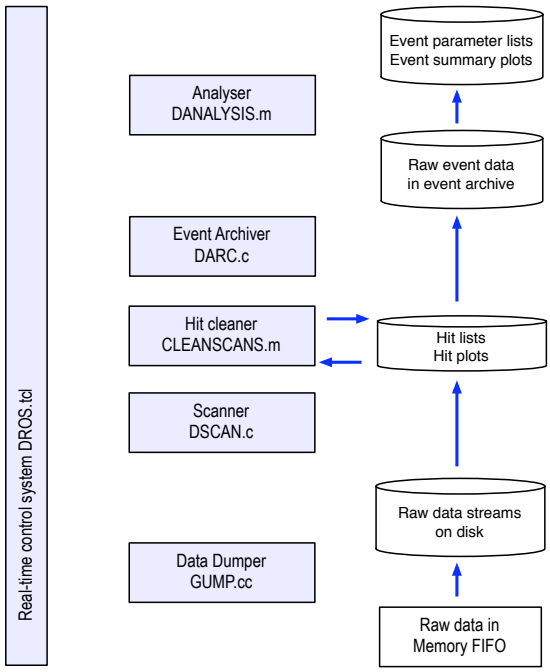

Figure 16.: Main modules of the real-time SD data processing software.

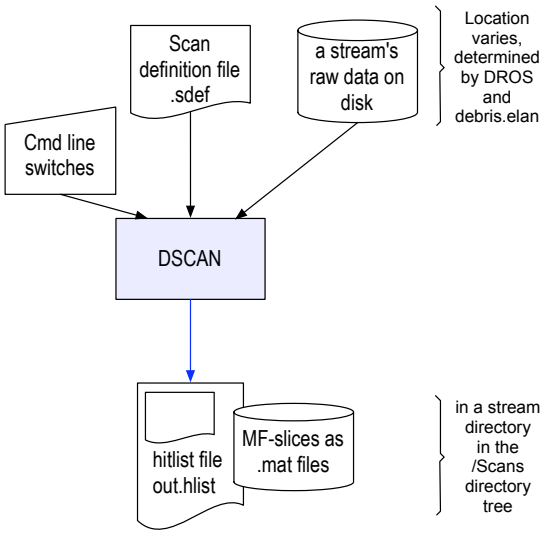

Figure 17.: Space debris scanner DSCAN.

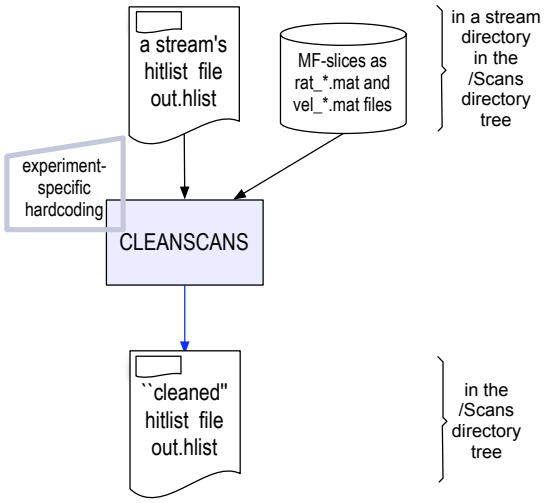

Figure 18.: Bad hit removing program CLEANSCANS.

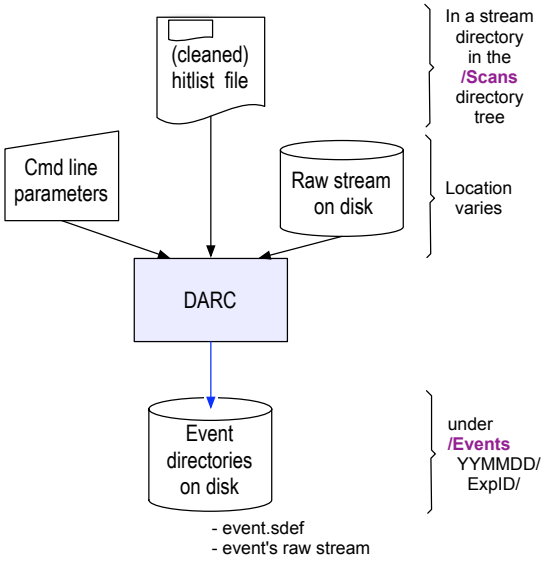

Figure 19.: Hit grouping, event archiving program DARC.

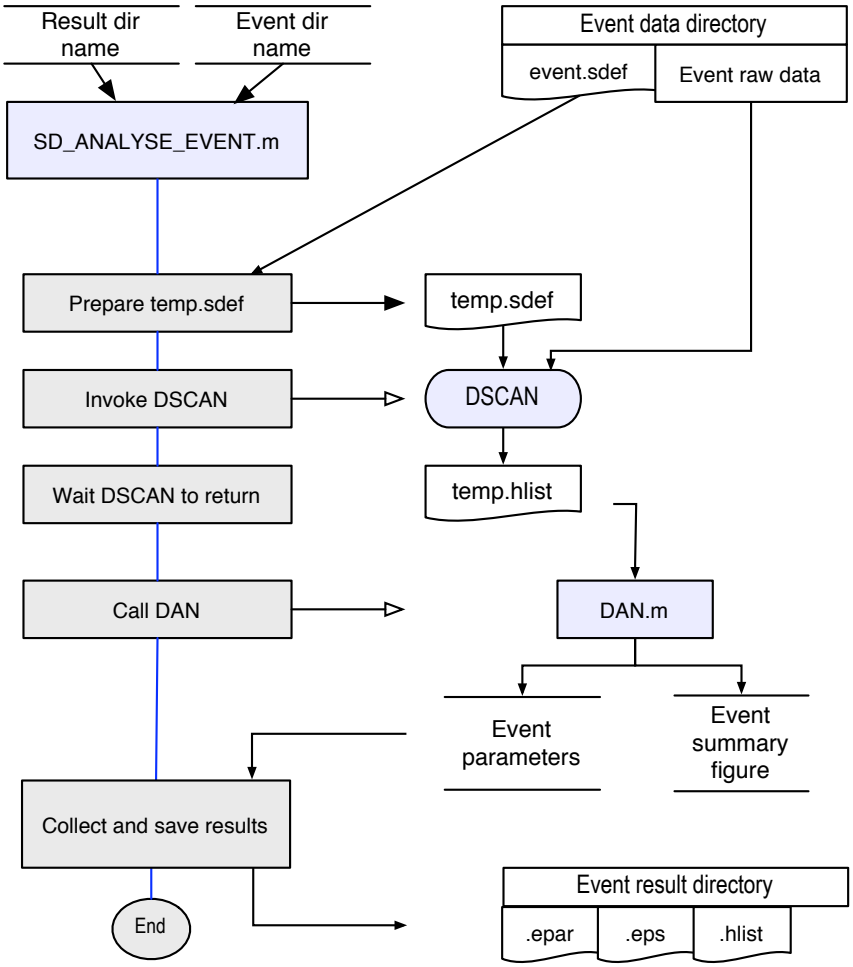

Figure 20.: Parameter estimation by SD_ANALYSE_EVENT.M. Matlab can invoke external UNIX programs like DSCAN in a standard way, so SD_ANALYSE_EVENT prepares a suitable scan definition file for DSCAN—based on the event's hitlist file event.sdef—launches the scanner, and reads the scan results from a file. Then it calls the fitting and plotting m-file DAN.m, to deduce and plot the event parameters. The file were the event parameters are written has the standard name eventlist.txt. The plots are accumulated to a single multipage postscript file, events.ps (often we prepare also a PDF version of the file). The results for each event are also saved into an event-specific result directory. The current version of the analysis software saves the event summary plot as an encapsulated postscript file, and saves the plotted time-series data also in numerical form, simply by copying the DSCAN output file temp.hlist to the event's result directory, so that refitting is possible if desired. The event parameters are saved to a separate event parameter file, for which we use the extension '.epar'.

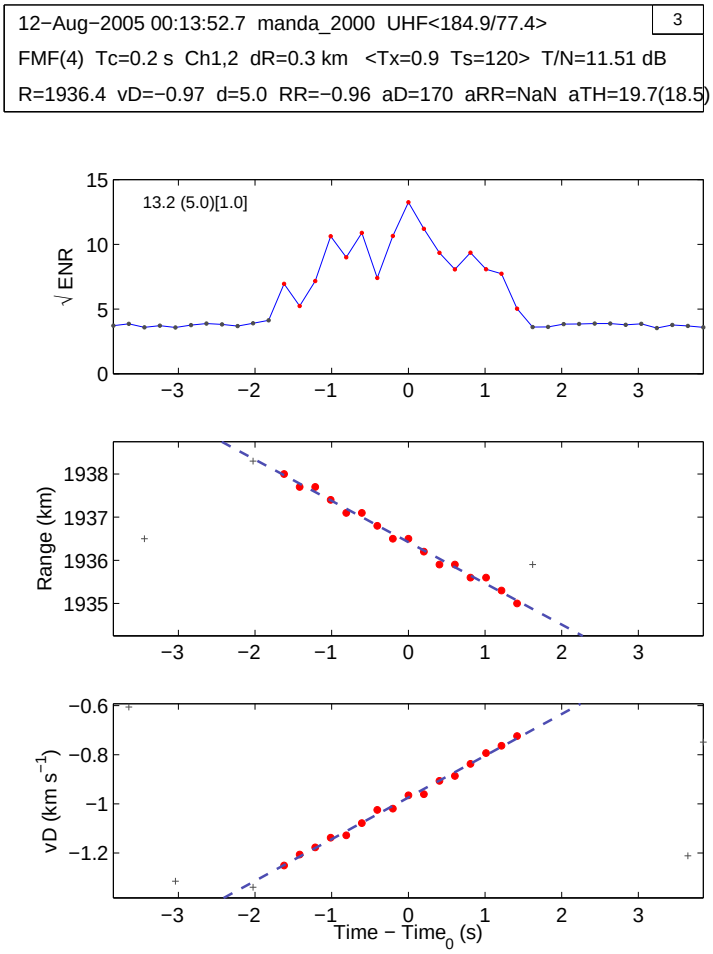

Figure 21.: Standard-format event summary plot for an event in the August 2005 MANDA campaign. The event parameter file for this event is given in Table 3 on p. 50. The top panel shows the square root of the estimated energy-to-noise ratio as function of time. In the red points, the signal exceeds the detection threshold (5.0 in this case). Background (=1) is not subtracted in this plot, so a more precise labeling of the y-axis would be $\sqrt{1+\widehat{\mathrm{ENR}}}$. The middle panel gives the target range in subsequent integrations, and the bottom panel gives the target Doppler-velocity. There is a good agreement between the range rate ("RR" in the header panel) derived from the slope of $R(t)$ in the middle panel, and the Doppler-velocity v_D taken from the fit in the bottom panel for the time of maximum signal strength. The slope of the v_D data in the bottom panel, which corresponds to a "Doppler-drift" a_D, is unrealistically large, 170 $\mathrm{m\,s^{-2}}$. This feature is an artifact due to the FMF-algorithm, which shortens the time axis by the transmission duty cycle $\mathcal{D}$, and stretches the frequency axis correspondingly. The true radial acceleration is about $\mathcal{D}\cdot 170\ \mathrm{m\,s^{-2}} = 17\ \mathrm{m\,s^{-2}}$ in this case. In the event parameter files, as well as in the plot headers, we nevertheless take a_D simply from the slope of $v_\mathrm{D}(t)$. The estimate does not normally go wrong quite this badly.

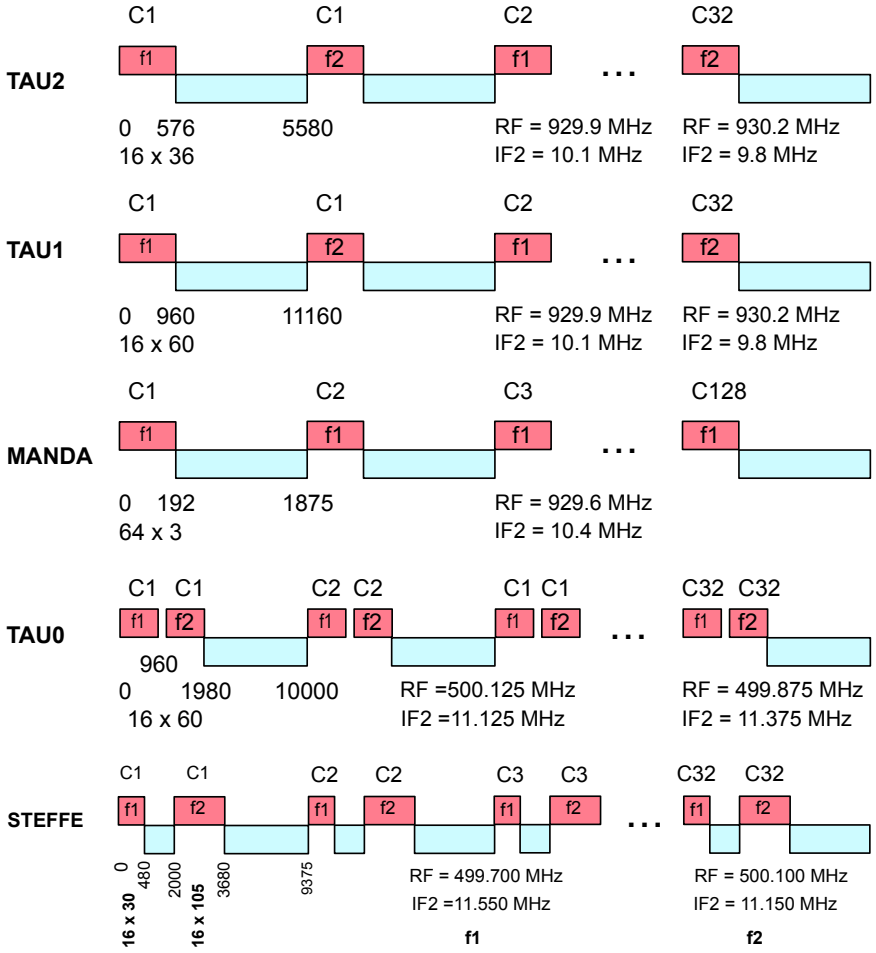

Figure 22.: Timing diagrams of five common EISCAT standard transmission/reception schemes. The schemes TAU1, TAU2 and MANDA are for the Tromsø UHF radar, while TAU0 and STEFFE are for the EISCAT Svalbard radar. The diagrams are not drawn to scale, but the labels indicate the length of the transmission (e.g., 576 μs in TAU2), the length of the interpulse period (5580 μs), and the transmission frequencies, both the RF frequency and the second IF frequency which is sampled by the SD receiver. All the transmissions are binary phase-coded. The number of code "bits" and their duration is also shown (16 bits $\times$ 36 μs). The bit patterns are from a set of N codes, where $N = 2\times$ number of bits. The code order in a given frequency channel is $C_1 \ldots C_N$ in TAU2–MANDA and STEFFE, but (for clutter cancellation purpose) $C_1, C_2, C_1, C_2, C_3, C_4, C_3 \ldots C_{32}$ in TAU0. Therefore, in TAU0, ranges from 3000 km up are ambiguous, while in the other experiments the first ambiguous range is much further away. Though not indicated in the diagram, the transmission blocks are surrounded by a receiver protection window, typically starting about 50 μs in front, and extending at least 100 μs after, the transmission. During the protection window, the receiver is closed to the sky but takes in a sample of the transmission waveform.

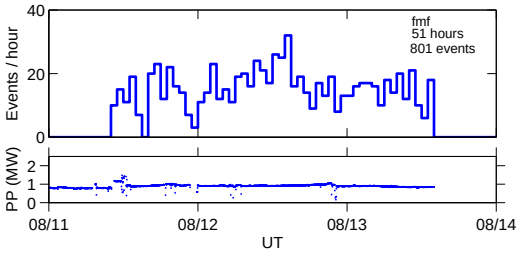

(a) Aug 11-13: Hourly event count, transmission peak power.

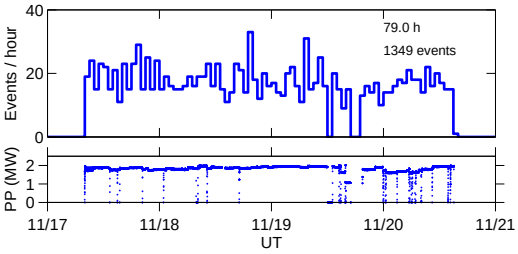

(b) Nov 17-20: Hourly event count, transmission peak power.

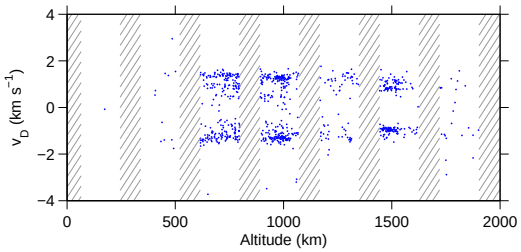

(c) Aug 11-13: Doppler-velocity v altitude.

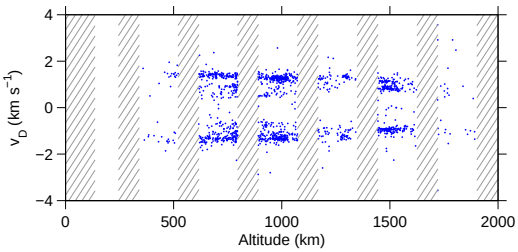

(d) Nov 17-20: Doppler-velocity v altitude.

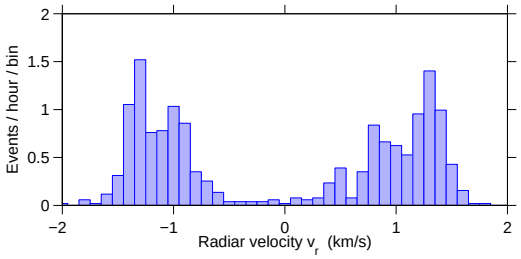

(e) Aug 11-13: Mean event rate v. Doppler-velocity.

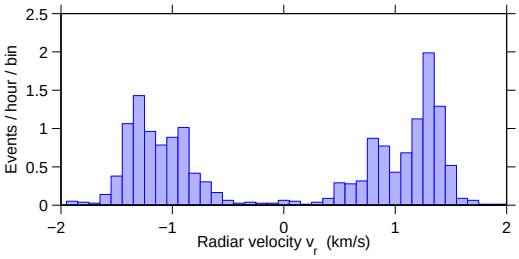

(f) Nov 17-20: Mean event rate v. Doppler-velocity.

Figure 23.: Summary plots of the MANDA campaings, 11–13 August and 17-20 November 2005 at Tromsø UHF. The UHF antenna was parked to magnetic field-aligned direction, azimuth 184.9° and elevation 77.4°. The observations shown here exclude altitudes below 150 km, where a large number of meteor events took place. Detection was done with the FMF-algorithm, using 0.3 s coherent integration. Parameter estimation was also done with FMF, but using shorter, 0.2 s integration time. More summary plots are shown in Fig. 24.

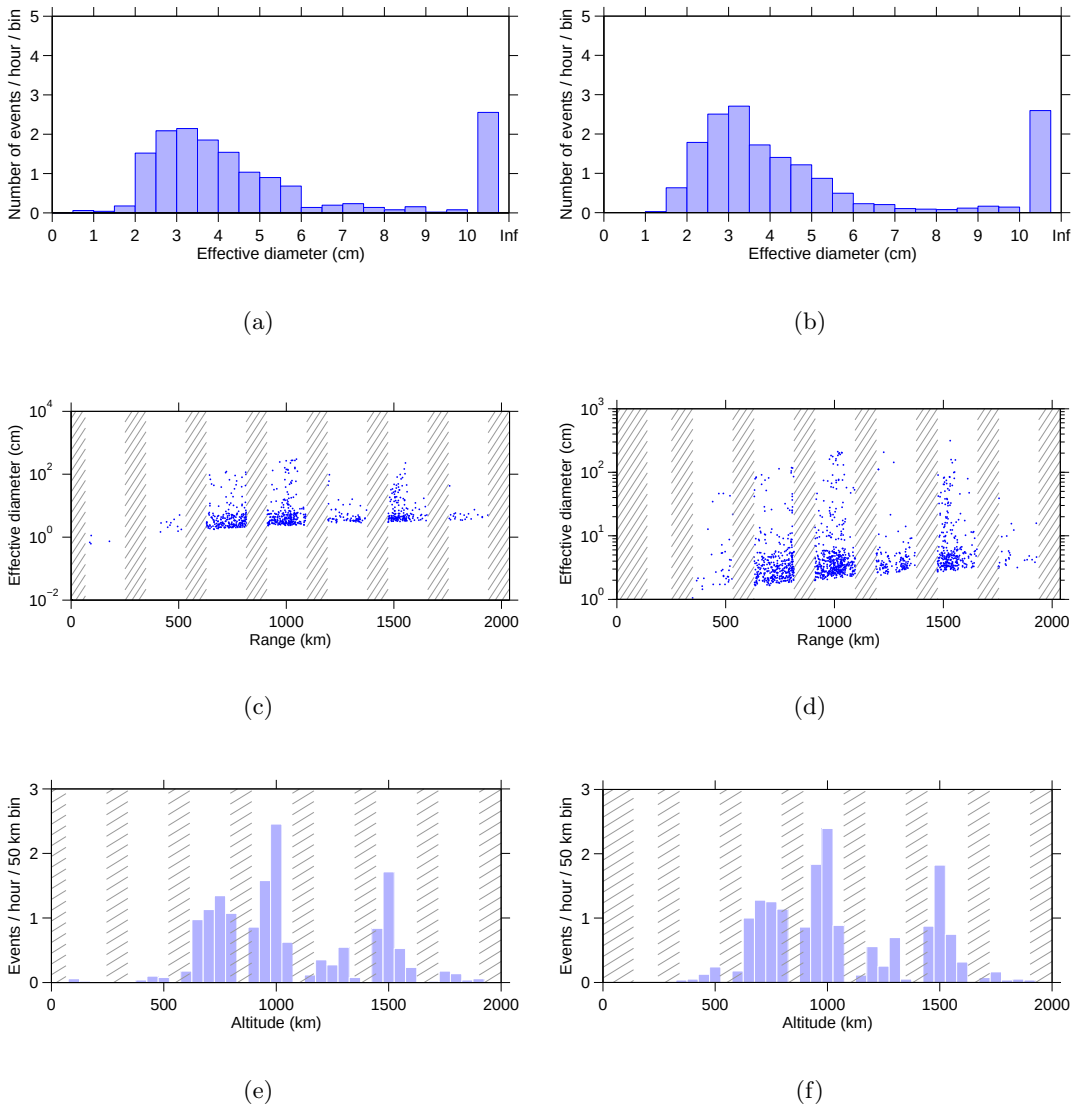

Figure 24.: Summary plots of the MANDA campaigns, 11–13 August (panels a,c,e) and 17-20 November 2005 (panels b,d,f). See also Fig. 23. The top row shows the effective size distribution of all events, the middle row plots effective diameter against range for all events, and the bottom row shows the altitude distribution of the events.

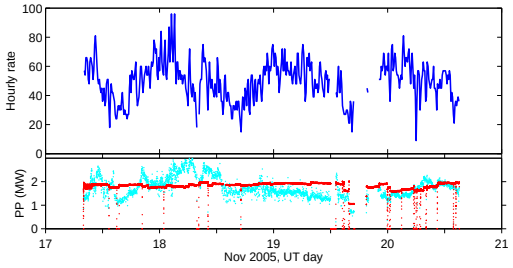

(a) Hourly event rate (one hour moving average), and transmission peak power.

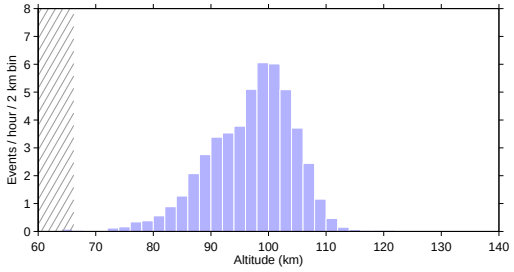

(b) Event rate as function of altitude.

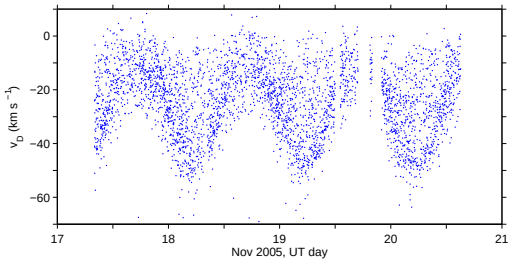

(c) Radial velocity v time.

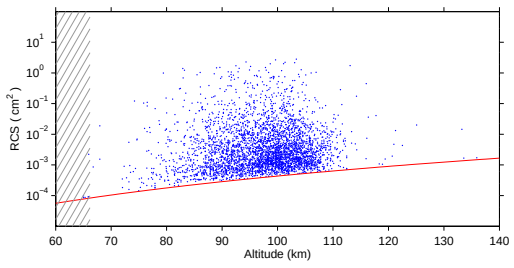

(d) Radar cross section v altitude.

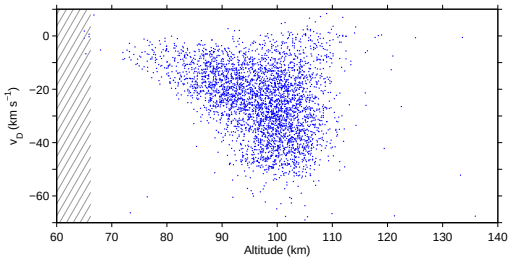

(e) Radial velocity v altitude.

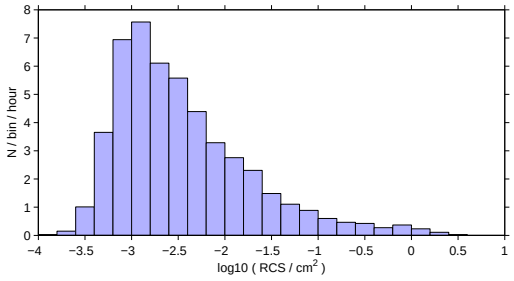

(f) Event rate v cross section.

Figure 25.: Analysis summary plots of 3653 MANDA METEOR events 17-20 November 2005, analyzed with non-coherent integration of two pulses. Panel (a) shows a clear diurnal variation in the number of observed events. In the bottom sub-panel of panel (a), the red points give the peak transmission power as reported by the standard EISCAT ionospheric data analysis, while the cyan points give the power as deduced from the transmission samples recorded by the SD receiver (in the data analysis for effective cross section, panel (d), a constant peak power 1.8 MW was used). Panel (b) gives the altitude distribution of the events. There is a curious-looking bump at around 90 km altitude. Panel (c) shows the Doppler-velocity; there is strong diurnal variation, with the largest magnitudes at about 06 local time, when the radar rams head-on into the sun-orbiting meteoroid cloud. Panel (d) gives an "effective" radar cross section, computed with the same formula, Eq. (2.15), that we use for the debris events.

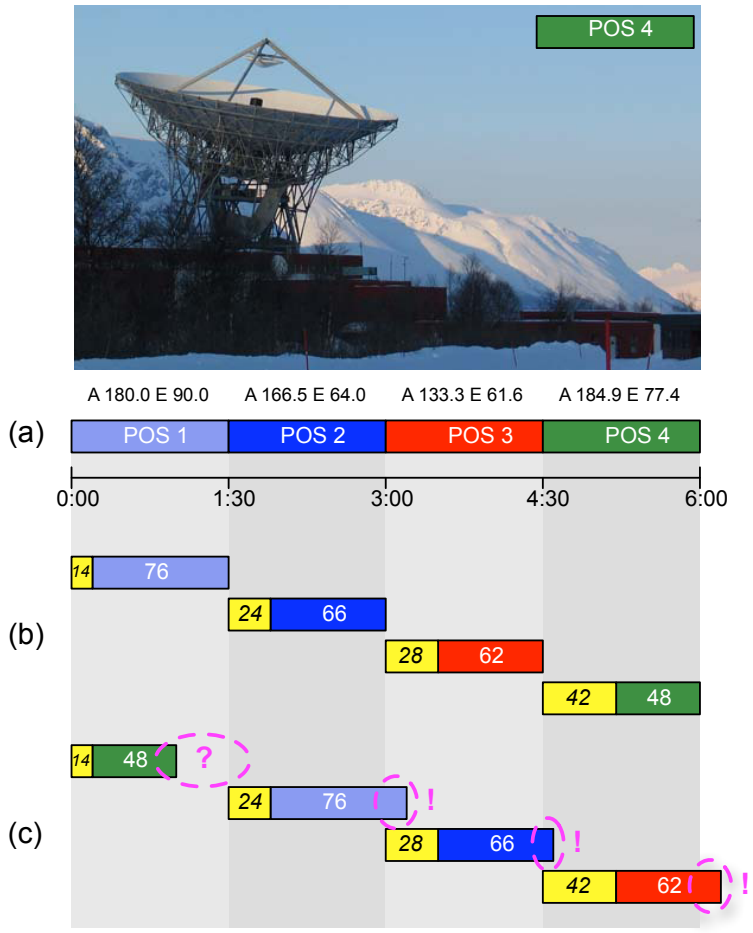

Figure 26.: Antenna pointing loop in the CP2 experiment at the Tromsø UHF radar. The 6 minute pointing cycle has four parking positions, with azimuths and elevations as shown in panel (a). The cycle starts with the antenna using 14 seconds to slew from position 4 to position 1. Then the antenna is parked for 76 seconds for data recording before moving in 24 seconds to position 2. And so on, as shown in panel (b). Due to a programming error in the SD receiver real-time control software, in the September 2005 campaign, from Septempber 7th until September 20th, the space debris receiver recording was out of synchronization with respect to the antenna motion, as shown in panel (c). The problem was fixed so that the SD recording was as intended, in accordance to panel (b), from 02 UT, September 20th. As indicated in panel (c), the incorrect alignment caused some data being recorded with moving antenna, these are the circled intervals marked by an explanation point. After analysis, the events (592 out of 5743) whose maximum signal strength occurred during these intervals, were ignored from the plots that we show in this report, and were not included into the event statistics we quote. Of course, nothing could be done to recover the data that were not recorded during the 28 s intervals indicated with a question mark in panel (c).

```
Sep 19 MONDAY
=============

[[---lines omitted---]]

23:36

[[---lines omitted---]]

        Should soon release disk D (after having 8-10 analyses), disk
        space is getting low, I'm now on disk G, and have 57 GB left.

        Disk D 286E9 bytes 2005 09 08 01:36:14 - 2005 09 11 01:47:12

            POS1: 62.7E9 bytes     08 01:36:14 -         11 01:48:14_00022
            POS2: 85.0E9 bytes     08 01:37:54 -         11 01:49:54_00036
            POS3: 78.2E9 bytes     08 01:39:28 -         11 01:45:28_00031
            POS4: 60.3E9 bytes     08 01:41:12 -         11 01:47:12_00029

       THESE TIMES AND NUMBER OF FILES ARE BAD! WHAT IS WRONG ???
       Start times are OK, but the number of files are wrong. So gump
       is not STOPPED as it should.  The DROS log file looks OK:

        POS 1  (move = 14)
        -----
        [20-Sep-2005 00:30:00.0] {Gumper: waiting for cp2 pos1}
        [20-Sep-2005 00:30:14.3] {Gump started 20-Sep 00:30:14.0} /SD-GURSIP/etc/next_erosgump.conf
        [20-Sep-2005 00:30:14.4] {Gumper: recording in cp2 pos1 (180.00 89.98 1519) started}

        [20-Sep-2005 00:31:28.1] {Gumper: recording in cp2 pos1 stopped}


        POS 2  (move = 24)
        -----
        [20-Sep-2005 00:31:30.0] {Gumper: waiting for cp2 pos2}
        [20-Sep-2005 00:31:54.4] {Gump started 20-Sep 00:31:54.0} /SD-GURSIP/etc/next_erosgump.conf

[[---lines omitted---]

        But recording logs show disaster
        --------------------------------------------------------
        THIS IS ABOUT OK
        ----------------
        Sep 08  1:36:14 matti TxGump[9043]: NOTICE: Recording: UHF20050908013614
        Sep 08  1:36:14 matti TxGump[9043]: NOTICE:  - data root: /Volumes/D/Deb0/tau2_2000_cp2pos1
        Sep 08  1:36:14 matti TxGump[9043]: NOTICE:  - file extension:
        Sep 08  1:36:14 matti TxGump[9043]: NOTICE:  - length in seconds: 74
        Sep 08  1:36:14 matti TxGump[9043]: NOTICE: UHF20050908013614 sampling started at
2005-09-08 01:36:14.458814
        Sep 08  1:36:14 matti TxGump[9043]: NOTICE: Raw data directory: /Volumes/D/Deb0/
tau2_2000_cp2pos1/UHF20050908013614

        BUT THIS IS NOT
        ---------------
        Sep 08  1:48:14 matti TxGump[9236]: NOTICE: Recording: UHF20050908014814
        Sep 08  1:48:14 matti TxGump[9236]: NOTICE:  - data root: /Volumes/D/Deb0/tau2_2000_cp2pos1
        Sep 08  1:48:14 matti TxGump[9236]: NOTICE:  - file extension:
        Sep 08  1:48:14 matti TxGump[9236]: NOTICE:  - length in seconds: 46
        Sep 08  1:48:14 matti TxGump[9236]: NOTICE: UHF20050908014814 sampling started at
2005-09-08 01:48:14.402301
        Sep 08  1:48:14 matti TxGump[9236]: NOTICE: Raw data directory: /Volumes/D/Deb0/
tau2_2000_cp2pos1/UHF20050908014814
        Sep 08  1:49:01 matti TxGump[9236]: NOTICE: UHF20050908014814 sampling stopped, 47.0248
seconds

[[---lines omitted---]

        This means that all times in config files are computed wrong. HOW CAME?


20, TUESDAY
===========

01:14 UT

        The dwell times occording the log are
            {46 74 64 60},
        while they should be, and are correctly computed in gumploopc, to be
            {74 64 60 46},
        so there is rotation by one. Looks like a programming error ... in timing pipeline, no
doubt.
        And only two weeks waisted so far ... [sig].


1:52    OK from 01:41. Forced the correct dwell times by keying them to the
```

Figure 27.: An authentic piece of manually maintained campaign log during the September 2005 CP2 campaign at the EISCAT Tromsø site, from around the time in the night between September 19th and September 20th when a serious SD recording synchronization problem was finally detected and fixed.

```
 1: # Time reserved for antenna motion into positions 1, 2, 3 and 4, seconds.
 2: # These should be carefully turned to real antenna motion.
 3: # The times should also try to accommodate the gump start delay.
 4: # (See the file cp2_scan.txt for the CP2 timing results 23-Aug-2005).
 5:
 6: set skiplist  [ list  pos1 14  pos2 24  pos3 28  pos4 42]
 7: set timelist  [ list  pos1 90  pos2 90  pos3 90  pos4 90]
 8:
 9: for { set p 0 } { $p < $NPos } { incr p } {
10:     set Pname($p) [lindex $skiplist [expr 2*$p] ]
11:     set Pskip($p) [lindex $skiplist [expr 2*$p + 1] ]
12:     set Ptime($p) [lindex $timelist [expr 2*$p + 1] ]
13: }
14:
15: set pos 0
16:
17:     [[---code omitted---]]
18:
19: set streamlen [expr $Ptime($pos) - $Pskip($pos) - 2 ]
20:
21:     [[---code omitted---]
22:
23: GumpConfig $streamlen $Sampling_ns $Expname $Activeside $Logfile $PosID
24:
25:     [[---code omitted---]]
26:
27: # Gumper loop
28:
29: while { 1 } {
30:
31:     for {set pos 0 } { $pos < $NPos } { incr pos } {
32:
33:         set Position $Pname($pos)
34:         EngineMsg [list "Gumper: waiting for $Scan $Position"] [Utime]
35:
36:         # Wait antenna to move into position
37:
38:         [[---code omitted---]]
39:
40:         # Start gump
41:
42:         [[---code omitted---]]
43:
44:         # Now wait so long that there are 20 seconds left of current
45:         # position
46:
47:         set MainDwell [expr $Ptime($pos) - 20 - $Pskip($pos)]
48:         set streamlen [expr $Ptime($pos) - $Pskip($pos) - 2 ]
49:
50:         if [Gsync $MainDwell] {
51:             set breaked 1
52:             break
53:         }
54:
55:         # We now have 20 seconds left of the current position
56:
57:         # Prepare for a "buffer flip"
58:
59:         if { $gmp(bufflip) == 1 } {
60:             set Activeside [expr 1 - $Activeside]
61:         }
62:
63:         # Prepare for next position
64:
65:         set nextpos [expr ($pos + 1) % $NPos]
66:         set PosID "${Scan}$Pname($nextpos)"
67:         GumpConfig $streamlen $Sampling_ns $Expname $Activeside $Logfile $PosID
68:
69:         # Then wait 20 - 2 seconds
70:
71:         [[---code omitted---]]
72:
73:     }
74:
75: }
```

Figure 28.: Original, buggy segment of the file `dros4/lib/spade.tcl` in the DROS software, containing the piece of code in the tcl programming language that controls the SD recording in the CP2 experiment. The segment generates a stream of recorder configuration files and (re-)starts the external recorder process with a new such file for each pointing position. The bug caused the actual recording cycle to be shifted by one pointing position with respect to the antenna motion cycle, resulting in about 15% loss of data during the September 2005 campaign. The loop initialization in lines 1–26 is correct as shown, and, to add to the confusion, in the first pass of the loop even the first position records correctly. But after this very first position 1, things go wrong for all subsequent recordings, as described in Fig. 26, because in line 48 the position number variable ($pos) contains a wrong value.

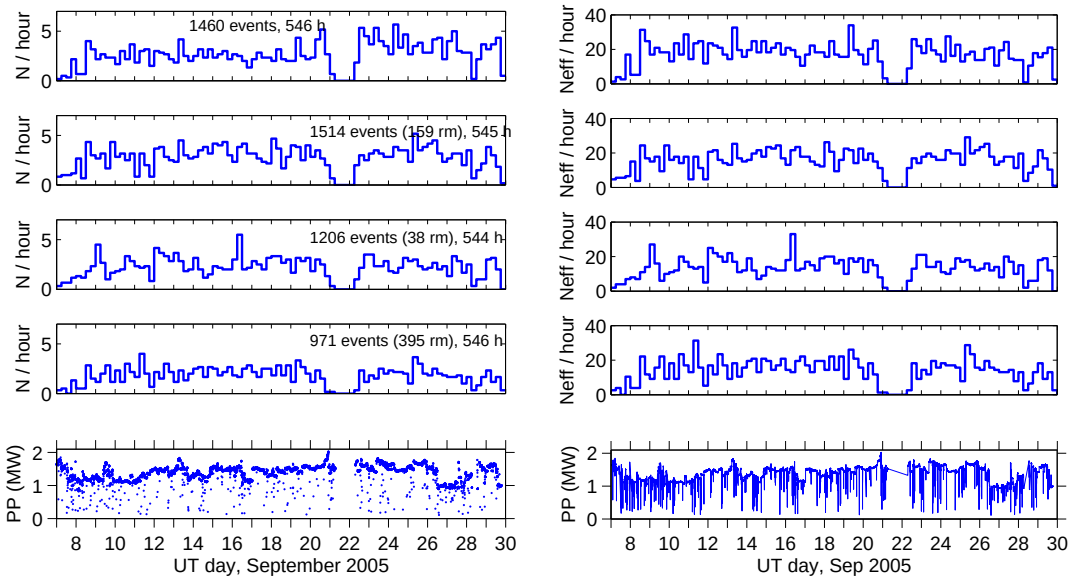

(a) Uncorrected event rate.

(b) Effective event rate.

Figure 29.: CP2, 7–29 September 2005 at Tromsø UHF. Panel (a) shows the actual, uncorrected hourly event count as function of time in the parking positions 1–4, in the top four sub-panels, and the peak transmitter power in the bottom sub-panel. In panel (b), the hourly rate has been divided by the recording duty cycle, separately for each position. The recording duty cycle is constant in positions 2–4, but in position 1, increases from 13% to 21% at 02 UT, Sep 20, when an error in the SD recording software was corrected. The transmitter peak power shown in this figure has been taken from the official EISCAT ionospheric data analysis results. Even though the power varied considerably during the run, in the SD data analysis, the constant value 1.3 MW was used throughout. (Similarly, a constant value 115 K was used for the system temperature.)

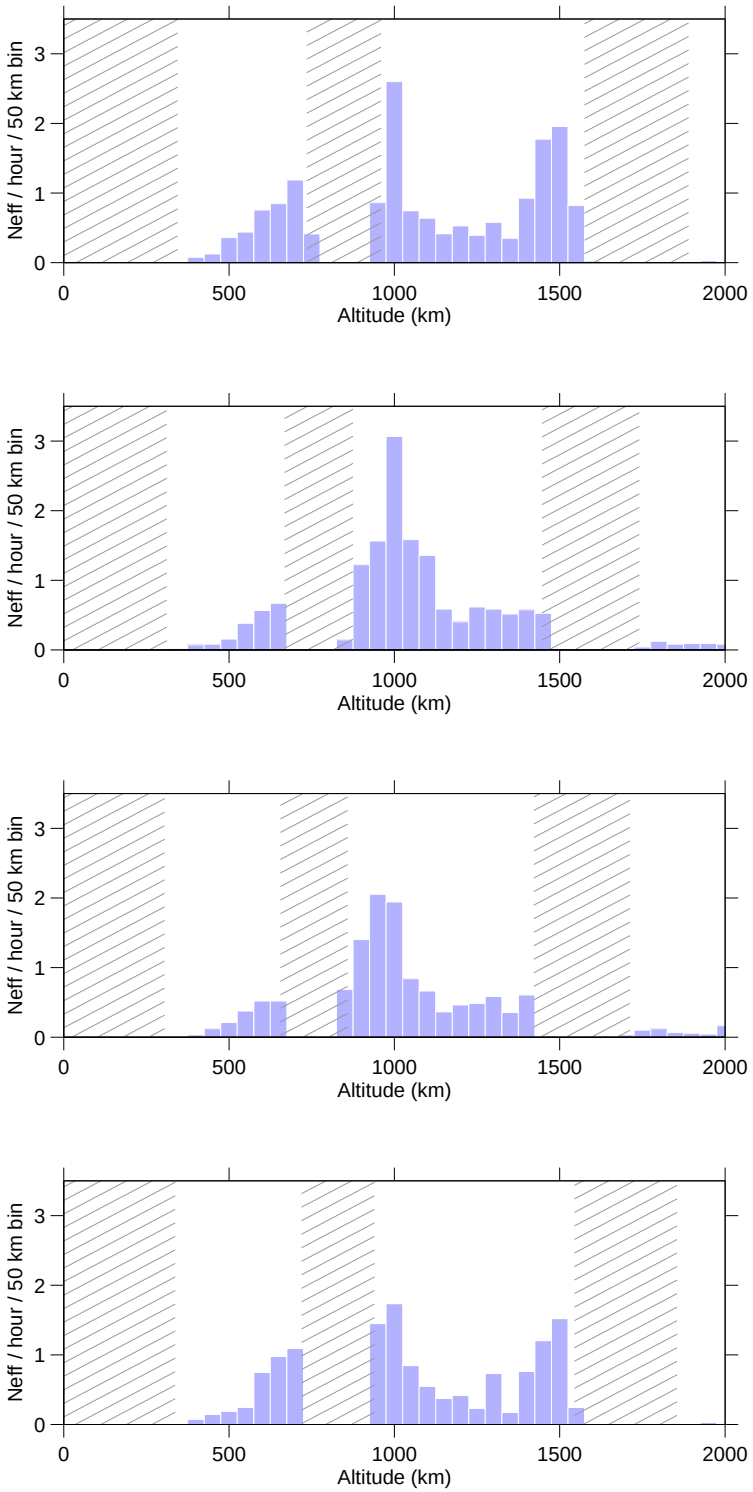

Figure 30.: CP2, 7–29 September 2005 at Tromsø UHF. Effective event rate as function of altitude in four antenna pointing directions.

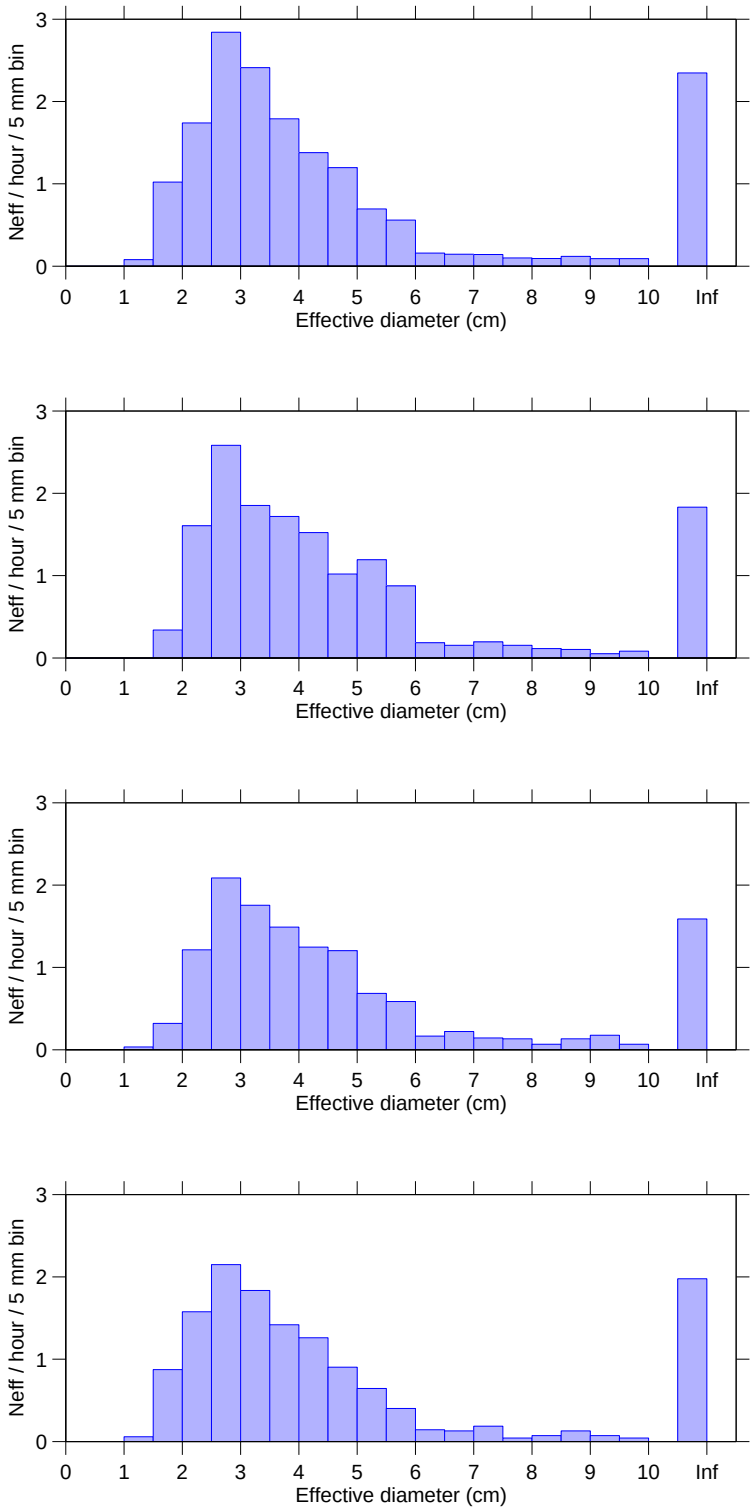

Figure 31.: CP2, 7–29 September 2005 at Tromsø UHF. Mean effective event rate as function of effective target diameter in four antenna positions.

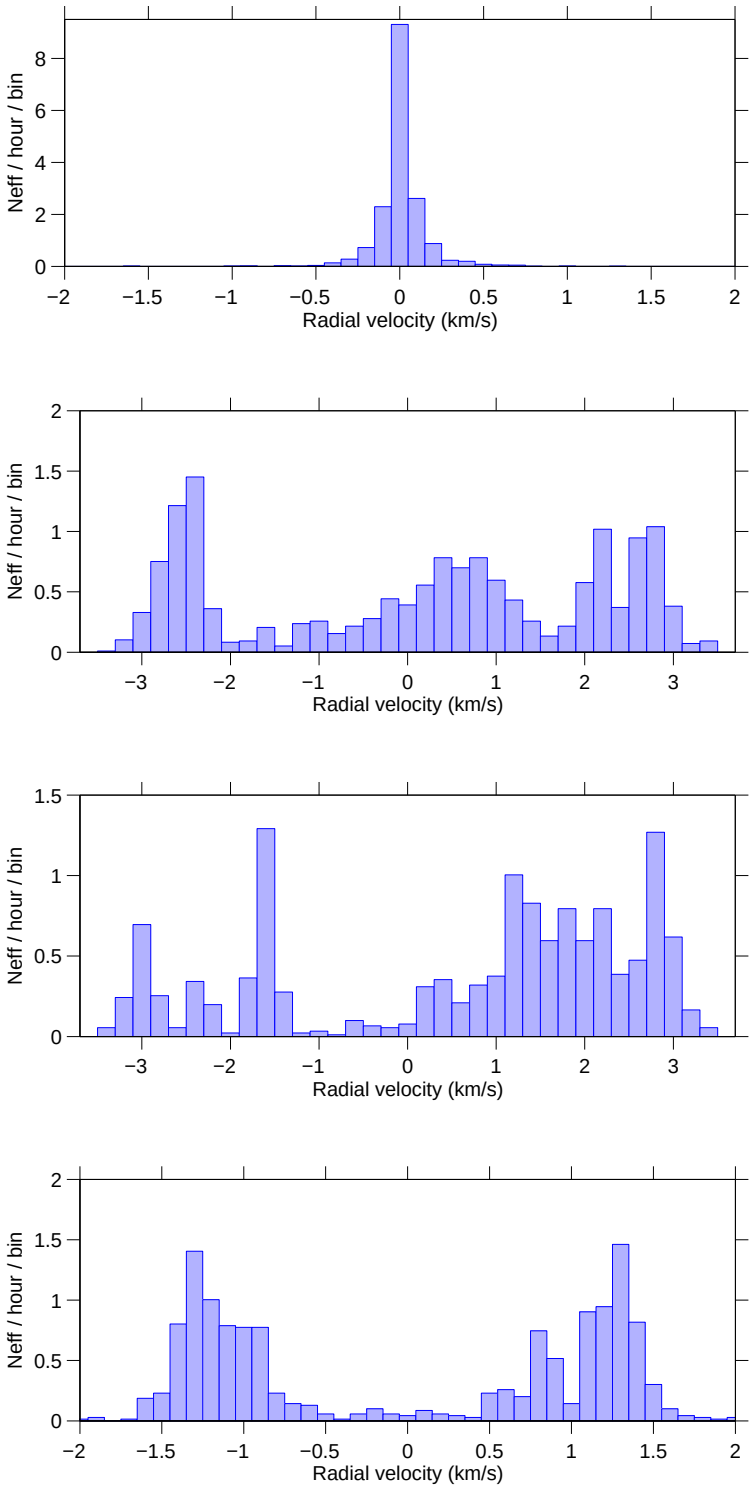

Figure 32.: CP2, 7–29 September 2005 at Tromsø UHF. Mean effective event rate as function of radial velocity in four antenna positions.

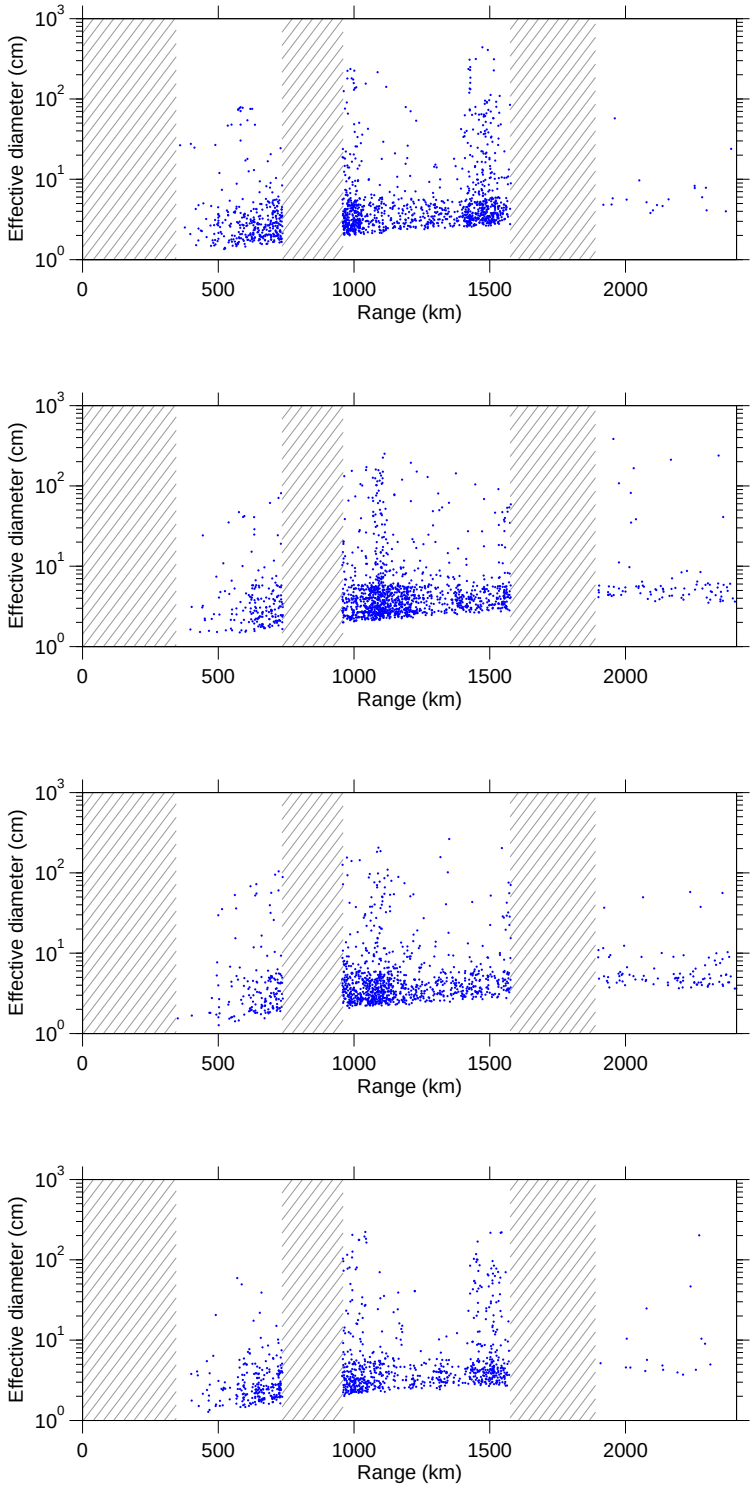

Figure 33.: CP2, 7–29 September 2005 at Tromsø UHF. Effective diameter v range in four antenna positions. Position 1: 1460 events, position 2: 1514 events, position 3: 1206 events, position 4: 971 events.

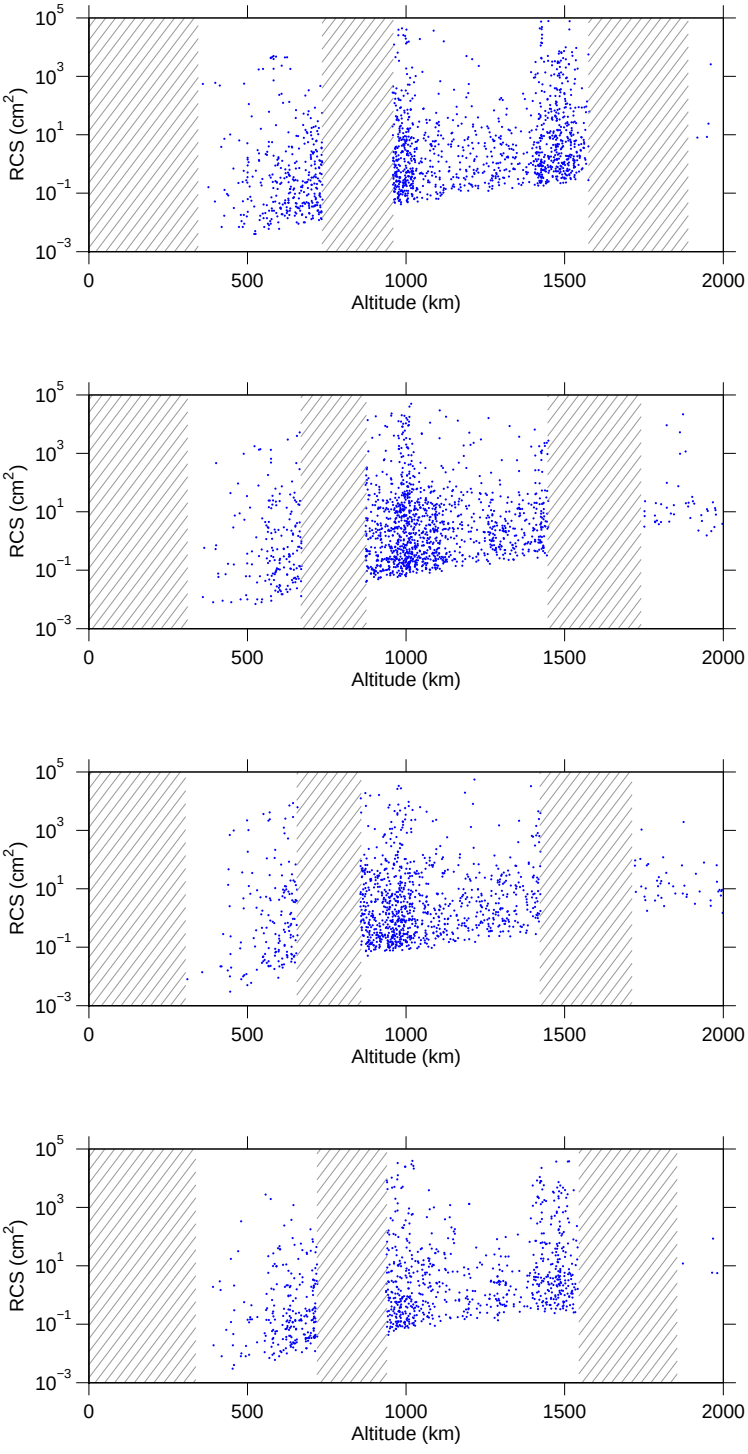

Figure 34.: CP2, 7–29 September 2005 at Tromsø UHF. Radar cross section v altidude in four antenna positions.

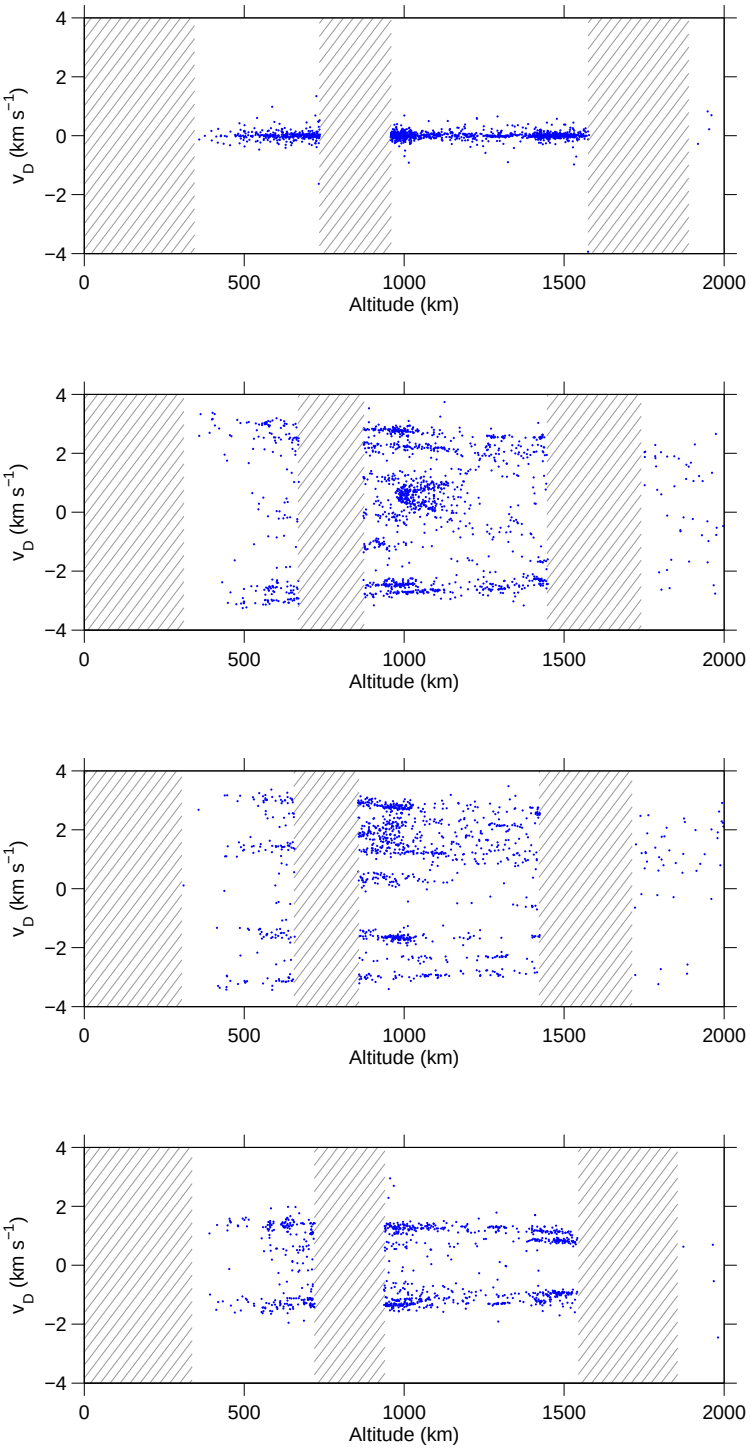

Figure 35.: CP2, 7–29 September 2005 at Tromsø UHF. Radial velocity v_D versus altitude in four antenna positions.

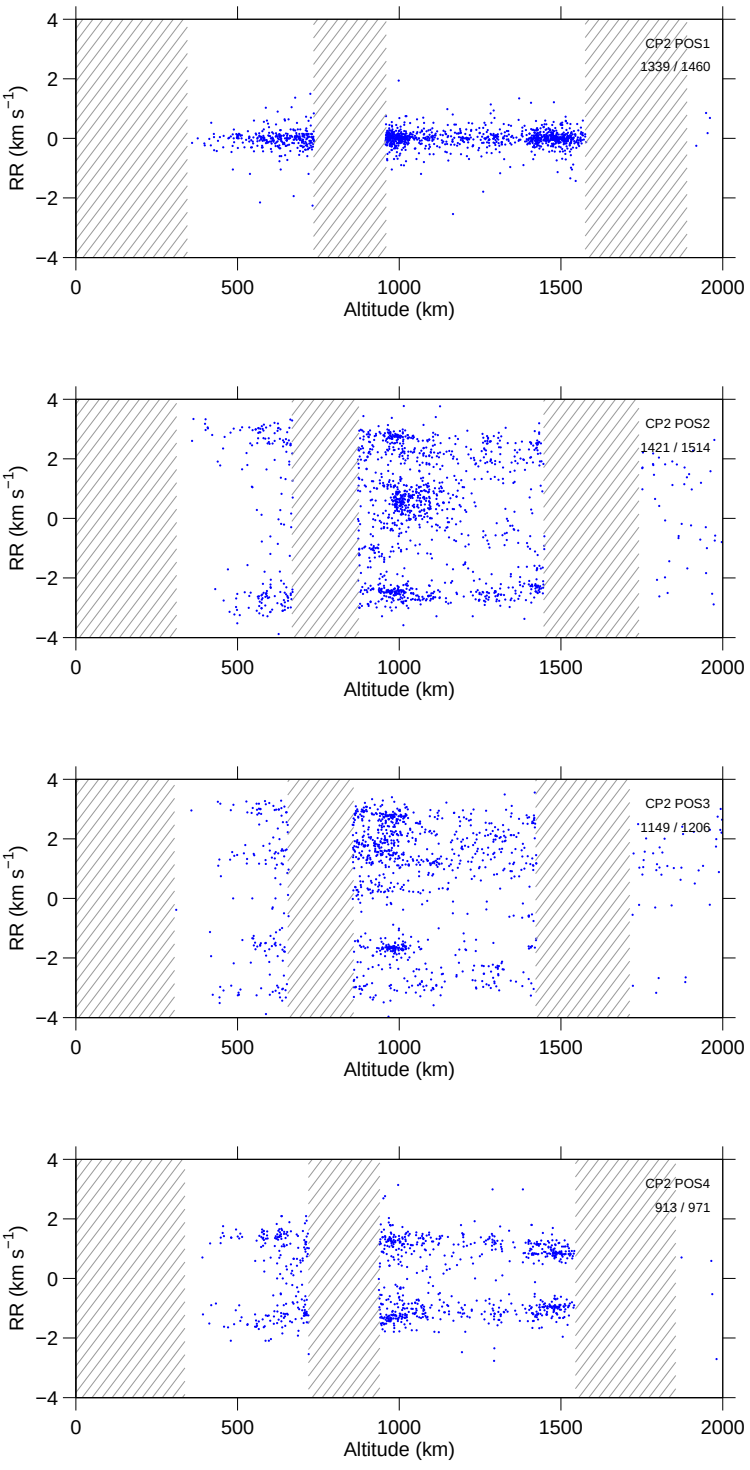

Figure 36.: CP2, 7–29 September 2005 at Tromsø UHF. Radial velocity dR/dt versus altitude in four antenna positions.

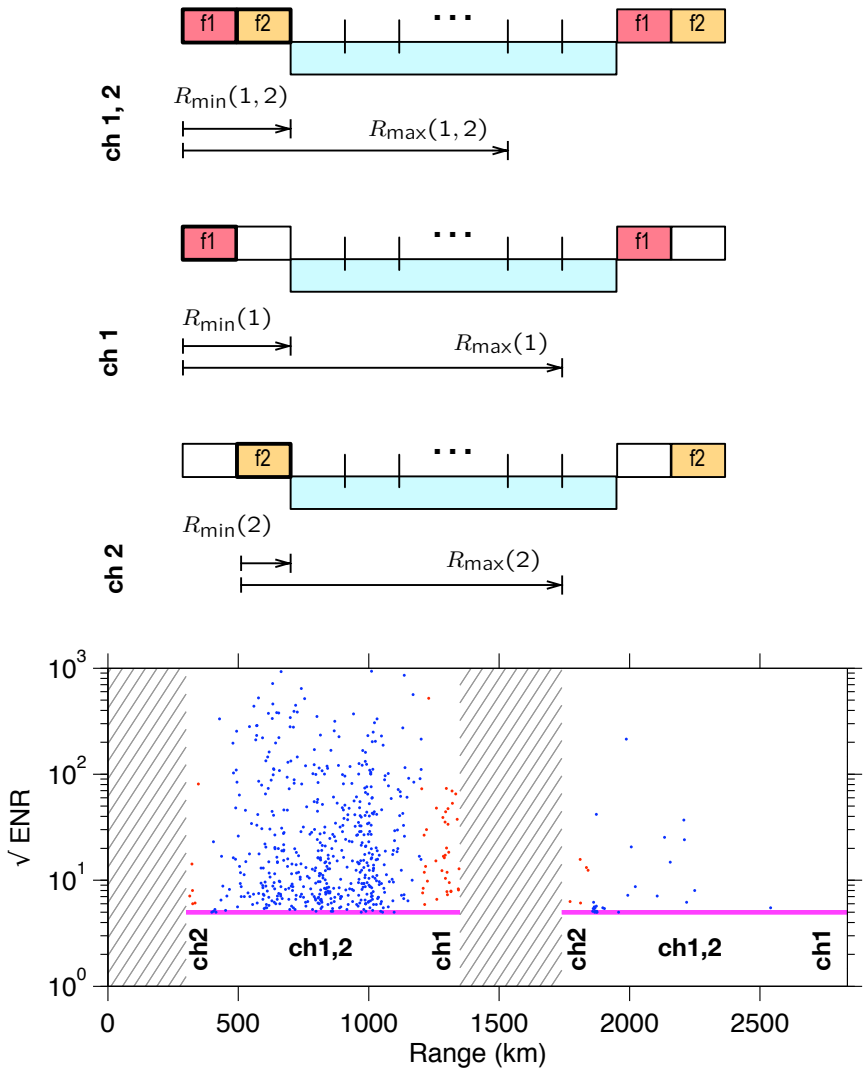

Figure 37.: TAU0, 10 November 2005 at EISCAT Svalbard radar. TAU0 transmission consists of two consecutive 960 μs pulses, on two frequencies. To increase the range coverage in the MF-method, it is worthwhile to use only one or the other of the pulses in the pattern-matching, in addition to using both pulses simultaneously. (In our present implementation, we actually scan the recorded raw data three times, with different .sdef files. This is a simple but rather inefficient approach.) The three diagrams in the top part of the figure indicate the minimum and maximum range available when using both frequency channels simultaneously, and when using only either the first or the second pulse. Of course, using shorter transmission results in loss of sensitivity. The scatter plot at the bottom part of the figure shows all 650 ("normal") tau0 events. The 600 events marked by the blue dots were detected and analysed using both channels simultaneously, while the rest where detected and analysed using either the first or the second pulse only. A range-independent threshold 5.0 was used in all cases.

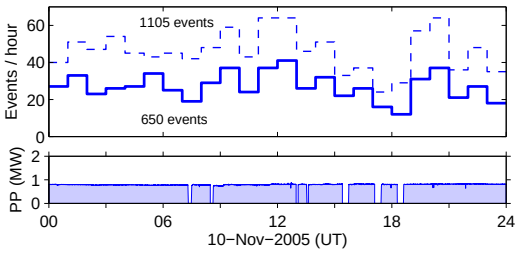

(a) Hourly event count and transmission peak power for events recorded when the transmission was through the 42 m antenna.

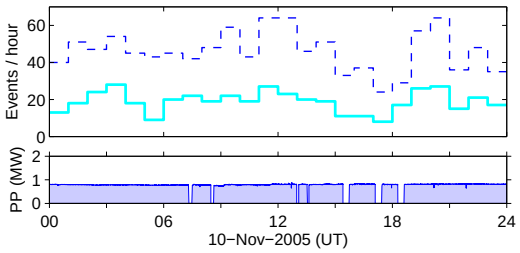

(b) Hourly event count in the data recorded by the SD receiver (hooked to the 42 m antenna) when transmission was through the other, 32 m, antenna.

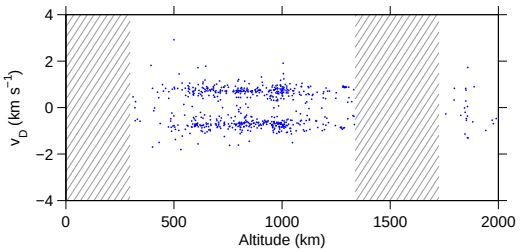

(c) Radial velocity and altitude in the standard events.

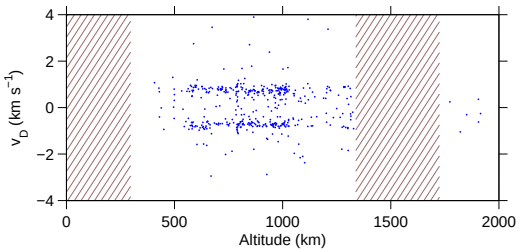

(d) Radial velocity and altitude in the bonus events.

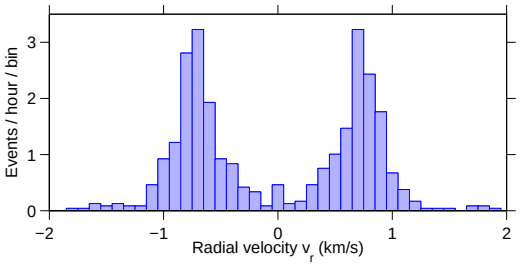

(e) Mean event rate as function of radial velocity in the standard events.

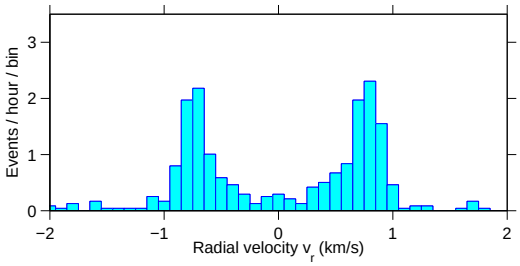

(f) Mean event rate as function of radial velocity in the bonus events.

Figure 38.: TAU0, 10 November 2005 at EISCAT Svalbard radar.

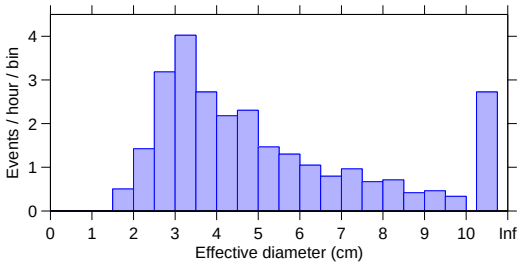

(a) Mean event rate as function of target diameter for the standard events.

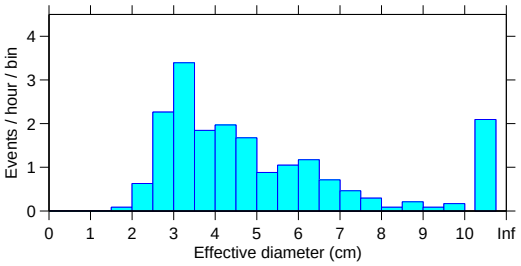

(b) Mean event rate as function of target diameter for the bonus events.

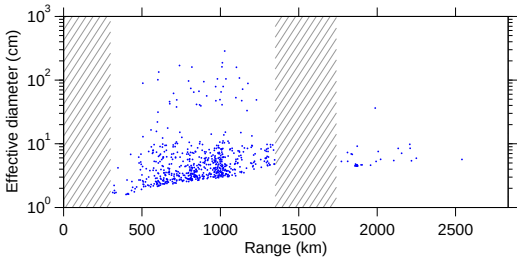

(c) Effective diameter and range of the standard events.

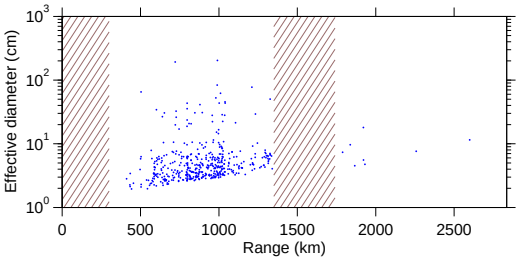

(d) Effective diameter and range of the bonus events.

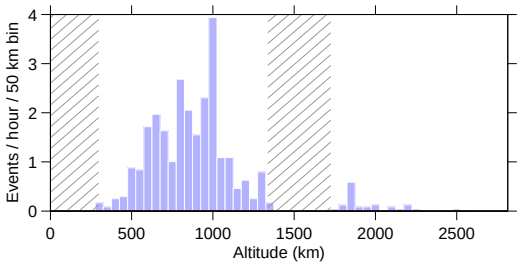

(e) Event rate as a function of altitude for the standard events.

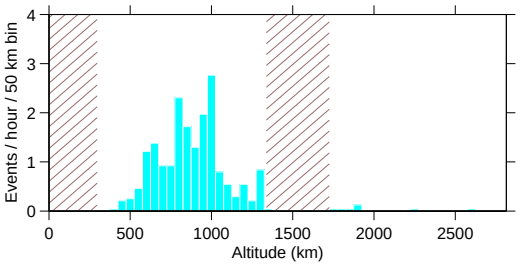

(f) Event rate as a function of altitude for the bonus events.

Figure 39.: TAU0, 10 November 2005 at EISCAT Svalbard radar.

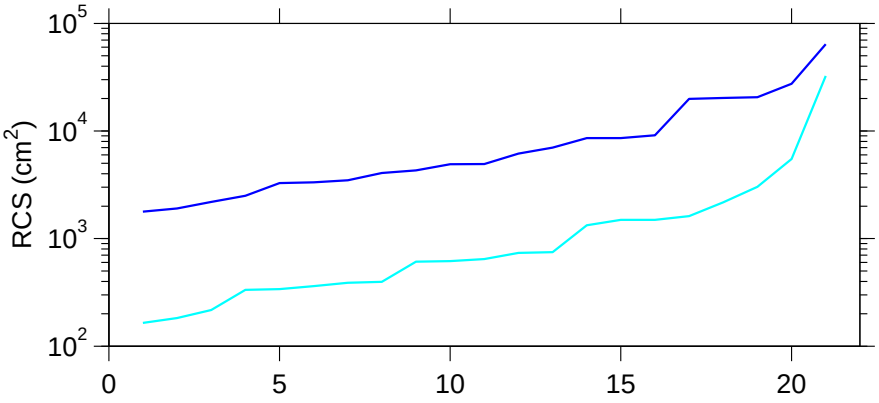

Figure 40.: TAU0, 10 November 2005 at EISCAT Svalbard radar. The 21 largest radar cross sections between ranges 800 and 1200 km, both in the set of normal events (upper curve), and the bonus events (lower curve), both computed assuming full transmission power. There is roughly a decade's difference between the curves. One expects that in both transmission situations, the SD receiver would easily detect *all* the large events that come to the radar's field of view. Then it is not unreasonable to assume that in a 24 hour measurement, roughly the same large-size end of the size distribution is measured in both case. The curves therefore suggest that the true transmission power for the bonus events has been lower than was assumed in the RSC computation, by about the factor of 10.